Title

AN ELECTROCHEMICAL AND MORPHOLOGICAL STUDY OF THE EFFECT OF TEMPERATURE ON THE RESTRUCTURING AND LOSS OF CAPACITY OF ALKALINE BATTERY ELECTRODES

Authors

Macdonald, D.D.
Pound, B.G.
Lenhart, S.J.

Publication Date

1984-11-01

LBL-18716
UC-94c

Lawrence Berkeley Laboratory
UNIVERSITY OF CALIFORNIA

APPLIED SCIENCE DIVISION

AN ELECTROCHEMICAL AND MORPHOLOGICAL STUDY OF THE EFFECT OF TEMPERATURE ON THE RESTRUCTURING AND LOSS OF CAPACITY OF ALKALINE BATTERY ELECTRODES
Final Report

D.D. Macdonald, B.G. Pound, and S.J. Lenhart

November 1984

APPLIED SCIENCE DIVISION

Prepared for the U.S. Department of Energy under Contract DE-AC03-76SF00098

DISCLAIMER

LBL-18716

AN ELECTROCHEMICAL AND MORPHOLOGICAL STUDY OF THE EFFECT OF TEMPERATURE ON THE RESTRUCTURING AND LOSS OF CAPACITY OF ALKALINE BATTERY ELECTRODES

Final Report

November 1984

by

Digby D. Macdonald, Principal Investigator
Bruce G. Pound, Senior Research Associate
Stephen J. Lenhart, Graduate Research Associate

Fontana Corrosion Center
Department of Metallurgical Engineering
The Ohio State University
116 West 19th Avenue
Columbus, Ohio 43210

for

Technology Base Research Project
Lawrence Berkeley Laboratory
University of California
Berkeley, California 94720

This work was supported by the Assistant Secretary for Conservation and Renewable Energy, Office of Energy Systems Research, Energy Storage Division of the U.S. Department of Energy under Contract No. DE-AC03-76SF00098, subcontract no. 4506610 with the Lawrence Berkeley Laboratory.

ABSTRACT

The degradation processes occurring within porous nickel battery electrodes have been investigated during charge/discharge cycling at temperatures in the range 0 to 100°C. The ac impedance of two types of porous nickel electrodes (sintered electrodes and rolled and bonded electrodes) in 8 m KOH solution was measured, and the data were analyzed in terms of a transmission line model (TLM). In addition, cyclic voltammetry was used to study the characteristics of the oxygen evolution reaction on nickel electrodes during charging.

Impedance data of planar, non-porous electrodes were obtained over a range of potentials and temperatures in order to provide an equivalent circuit to model the pore-wall and backing-plate interfacial impedance components in the TLM.

Parameters in the TLM were curve-fitted to experimental impedance data obtained for porous electrodes at different stages of cycling. Changes in these parameters with cycling time for rolled and bonded electrodes were consistent with experimental observations, and could be attributed to various degradation processes. The principal changes found to occur with increasing cycle number were that the average pore effective length decreases and the average solid-phase resistivity increases.

The impedance data for sintered electrodes do not change during galvanostatic cycling and failures occur abruptly after a relatively large number of cycles. Consequently, the TLM provides little insight into cycle-dependent degradation phenomena on sintered electrodes.

TABLE OF CONTENTS

ILLUSTRATIONS

INTRODUCTION

Secondary alkaline batteries are considered promising near-term energy storage systems for electric vehicle propulsion and for some load-leveling applications. Porous nickel electrodes are used in a number of candidate battery systems including nickel-iron, nickel-zinc, and nickel-hydrogen cells. Each of these batteries must meet several performance criteria: high specific power, high specific energy, low cost, and long cycle life. At present, the viability of these batteries is often limited by the degradation of the electrode materials, In some cases, the nickel plate has been found to limit the life of the battery.

Porous alkaline battery electrodes can undergo a loss in charge capacity due to restructuring of the active material as the system is cycled between high and low states of charge. This phenomenon leads to a gradual decrease in the coulombic efficiency of a battery due to mechanical damage and/or a reduction in the active surface area and porosity of the cathode or anode, or both. The reduction in porosity restricts the access of the electrolyte to the inner regions of the active material and the concomitant growth in particle size reduces the area to volume ratio. Furthermore, the oxidation products such as $Fe(OH)_2$ and NiOOH generally have Pilling-Bedworth ratios in excess of one; that is, the oxidation product occupies a greater volume than the metal from which it forms. The resulting internal tensile stresses may rupture interparticle bridges and hence degrade electronic transport through the porous mass. These stresses can ultimately cause a loss in the structural integrity of the electrode and sloughing of the active material may occur from the electrode surface.

The performance of porous nickel electrodes can be irreversibly affected by several modes of degradation. These electrodes are susceptible to the mechanical stresses as described above, and therefore may undergo both a degadation in the electrical resistance of the substrate particle-particle bonds and a separation of the active material from the current collector. In addition, nickel plates, like all porous electrodes, can sustain electrolyte

exhaustion within the pores which causes a decrease in the cell power due to mass transport and ohmic overpotential losses. Moreover, cycle and temperature dependent parasitic processes, such as oxygen evolution, can reduce the charging efficiency.

Each of the degradation processes adversely affects the cell operation. However, the loss in performance often cannot be attributed to a particular process. In addition, the various modes of degradation are influenced by environmental conditions such as temperature. Accordingly, the major objective of this study was to determine the effect of the main degradation processes on the performance of porous nickel electrodes over the temperature range 0 to 100°C.

The electrochemical behavior of porous nickel hydroxide/oxyhydroxide electrodes at various stages of cycling was examined using the ac impedance technique. In order to analyze the impedance data for the porous electrodes, a transmission line model of finite length was adopted. The model takes into account the resistance of the solid "active" phase, which includes the resistance resulting from the degradation of particle-particle contacts due to restructuring of the electrode. The model also contains impedance terms for the active material/solution interface, the solution within the pores, and for the interface between the pores and the current collector.

Impedance data for a planar, non-porous nickel electrode were obtained over a range of potentials and temperatures to provide an equivalent circuit with which to represent the interfacial components of the transmission line model. In order to interpret these data, cyclic voltammetry was employed to identify the regions of potential for nickel hydroxide and oxyhydroxide formation. The conversion of nickel hydroxide to the oxyhydroxide phase occurs above the reversible potential for oxygen evolution, which can affect the electrode charging efficiency and even the cycle life of battery plates. Consequently, cyclic voltammetry was utilized also to study the characteristics of the oxygen evolution reaction on planar nickel electrodes during charging. The experimental data from the cyclic voltammetry and impedance techniques coupled with the transmission line model provide an insight into the nature of the primary modes of degradation occurring within

porous electrodes, and allowed the effect of temperature on the degradation mechanism to be determined.

The electrochemistry of nickel in alkaline solutions has been investigated extensively over the last ten years by a number of workers, and these studies are summarized in the following review. The physical structures of the charged nickel oxyhydroxide phases and reduced nickel hydroxide phases are described, and the cyclic voltammetry and ac impedance characteristics are then discussed. Finally, the transmission line model is described and a mathematical formulation for the impedance of porous electrodes in aqueous solutions developed.

1. LITERATURE REVIEW

1.1 The Nickel Electrode in Alkaline Solution

The performance of nickel positive plates in battery applications is strongly dependent on the structural and electronic properties of the active materials. The literature concerning nickel in alkaline solutions contains numerous descriptions of the active nickel hydroxide and oxy-hydroxide phases.

The properties of these phases are influenced by a multitude of variables associated with fabrication techniques, operating environment, and cycling conditions. In this section, properties of the active materials on nickel electrodes are summarized, particularly in relation to the effects of various environmental conditions and film preparation procedures.

1.1.1 Potential/pH Diagram

The original potential/pH diagram published by Pourbaix[1] for the nickel/water system was recently modified[2] to include phases observed experimentally (Figure 1). The regions of stability for the four solid nickel oxide phases originally predicted by Pourbaix have been replaced by two regions, one for nickel oxy-hydroxide, NiOOH at high potentials, and the other for nickel hydroxide, $Ni(OH)_2$ at intermediate potentials and pH. In addition, the ionic species at the highest pH has been changed.

The modified potential/pH diagram in Figure 1 does not indicate the full complexity of the system. In particular, it does not show the structural variations of the nickel hydroxide and nickel oxy-hydroxide phases. Over the past decade, virtually all of the literature on this system has acknowledged the presence of at least two structural forms of both nickel hydroxide and nickel oxy-hydroxide. The two forms of oxy-hydroxide, β(III) and γ, have similar free energies of formation[2] and are not distinguishable in the potential/pH diagram. Similarly, the free energy difference between the two nickel hydroxide phases, α and β(II), is small[6], and these phases can not be distinguished.

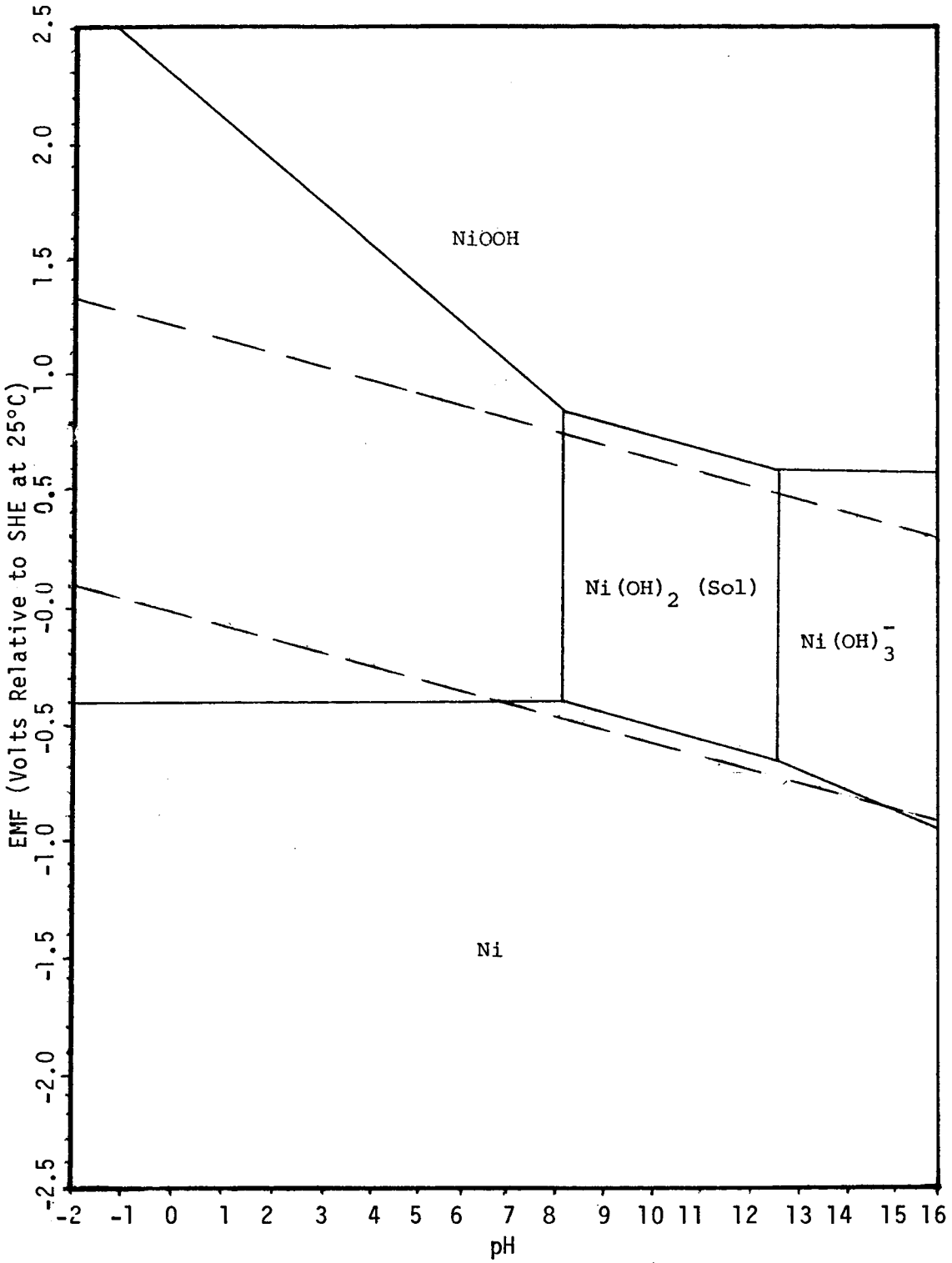

Figure 1. Revised nickel-water EMF-pH diagram at 25°C. All metal containing ionic species are at 10^{-6} activity.

Experiments in strongly alkaline solutions at potentials where dissolved divalent nickel species are predicted have failed to find evidence of these species except at elevated temperatures (40°C) and at potentials high enough for massive oxygen evolution[3]. Since alkaline battery systems are not operated at such high potentials, dissolved divalent nickel species are not considered further in this work.

Figure 1 shows that the reversible potential for oxygen evolution lies below the nickel hydroxide/nickel oxy-hydroxide transition potential. However, depending on the charging conditions, the overpotential required for a measurable oxygen evolution current is often large enough to allow oxidation of nickel hydroxide without significant charge transfer due to oxygen evolution[15].

The use of the stoichiometric formula NiOOH in Figure 1 to represent β(III)- or -nickel oxy-hydroxide is misleading. The β(III) and forms exhibit subtle variations in structure, and are distinguished by the oxidation state of nickel. The form has an average oxidation state well above 3.0. Values as high as 3.7 have been reported, but 3.5 is a more likely upper limit[5]. In contrast, the β(III) form often has a nickel oxidation state of less than 3.0. Water molecule[6-8], hydroxide ion[9], and foreign ion[10-12] incorporation into the lattice structures are also well established.

A similar situation exists for the nickel hydroxides. The stoichiometric formula $Ni(OH)_2$ does not accurately describe these phases. The α-nickel hydroxide structure incorporates water molecules, whereas the β form is thought to be largely, if not completely, anhydrous. The average oxidation state of nickel is often greater than 2.0 in these phases[40]. Despite the deviations from stoichiometry, the two nickel hydroxide structures will be denoted in this work by α- and β-$Ni(OH)_2$, while β- and γ-NiOOH will be used for the nickel oxy-hydroxide structures.

1.1.2 Crystal Structures

The divalent hydroxides, α and β(II), can both be present on discharged nickel battery electrodes. Their crystal structures can vary from highly crystalline to virtually amorphous[12-14], depending on their "age", the method

of film deposition, and film thickness. In addition, the various phases may differ with respect to hydration. The α(II) phase can be approximately represented[7,16] by the stoichiometric formula, $Ni(OH)_2 \cdot xH_2O$ where x varies from 0.5 to 0.7. However, while the β(II) phase has a similar structure, it is not hydrated.

The divalent nickel hydroxides can be oxidized to trivalent nickel oxy-hydroxides, as shown in Figure 1. The β(III) composition is described as almost exactly NiOOH according to Bode[6] but the more accepted view is that at least some divalent or tetravalent nickel species are present in solid solution depending on the oxidizing conditions[7,12]. Several authors have attempted to give detailed descriptions of the oxidation mechanism [17,24,37,41]. The oxidation of β-$Ni(OH)_2$ to β-NiOOH involves the mass transfer of roughly half of the protons from lattice sites to the electrolyte where they react with OH^- to form water[17,48].

Many investigators suggest that the β(III) phase should not be regarded as a distinct second phase. They indicate that β-$Ni(OH)_2$ oxidizes to β-NiOOH through a continuous series of solid solutions[7,12,14]. Considerable dissent has arisen especially in the more recent papers, and at present, there is more experimental support for a two phase transition[21,40-42]. Reversible potential measurements in 1 M KOH by Barnard et al.[41] indicate that the β(II) and β(III) phases exist simultaneously, with the mole fraction, X, of the β(II) component given by $0.4 < X < 0.7$. The formation of the γ-phase may occur above this range.

The oxidation of α- and/or β-$Ni(OH)_2$ gives γ-NiOOH[19,20]. The β(III) phase can be an intermediate in the latter case[40,41]. Within the phase, nickel species exist in a solid solution in the trivalent and tetravalent states. The proportion of each depends on the amount of charge extracted during oxidation. Oxidation of β- or α-$Ni(OH)_2$ to γ-NiOOH again proceeds with the removal of protons, but variable amounts of water, hydroxide, and foreign cations are simultaneously incorporated into the γ lattice.

The incorporation of foreign cations can be of considerable importance to the performance of nickel battery electrodes. For example, the alkali cations

of NaOH, KOH, and LiOH each influence electrode properties differently. They can affect the relative amounts of the various phases, the charge/discharge characteristics, and ultimately the cycle life[12,15].

1.1.3 Film Preparation

The initial film structure of a nickel electrode in alkaline solution is dependent on the film preparation procedure. The structure may then "age" or undergo charge/discharge cycling and the structural features may change significantly. Since the electrochemical behavior of the electrode is dependent on the structure and the degree of crystallinity of the film, it is important to understand the implications of film history. In this section, film structures obtained by several of the more common techniques are described.

Nickel hydroxide films have been prepared by electro-oxidation of a nickel substrate in hydroxide solution, by cathodic deposition in solutions containing divalent nickel species, or by alternate immersions in hydroxide and sulfate solution[22]. From ellipsometric studies, Hopper and Ord[23] conclude that the electrode-oxidation of nickel in alkaline solution produces a β(II) film. X-ray diffraction[24] and ellipsometric studies[23] suggest that cathodic deposition in nickel nitrate solutions produces an α film. The "colloidal" film structures produced by alternate immersions in hydroxide and nickel sulfate electrolytes have not been characterized, except by cyclic voltammetry which in itself can change the film structure.

Although Hopper and Ord [23] suggest that β(II) films are formed on electro-oxidized nickel substrates, it seems unlikely that a completely anhydrous film could form under these conditions. Visscher and Barendrecht[32] conclude that the α phase is formed initially but is converted to the β(II) phase upon subsequent anodic polarization. Hopper and Ord do not consider the possibility of a partially hydrated film or a mixture of α and β(II) phases. Evidence of partially hydrated films or "pseudo α phases" has been reported[13]. Some hydration at the film/solution interface might be expected, and water concentration gradients have been proposed[19].

Electro-oxidized nickel film structures have proved difficult to characterize because the films are not sufficiently thick. Thicknesses greater than

several hundred Angstroms are difficult to achieve potentiostatically or galvanostatically, and 40 to 50 Å are more usually observed.

Many investigators[10,14,17,33-36] have studied thick hydroxide films prepared by cathodic deposition on nickel substrates in solutions containing divalent nickel species. These films have XRD patterns typical of the α hydoxides[24], and can have thickness in excess of several thousand Angstroms[23]. Their electrochemical properties can be significantly different from those of the thin films outlined above, as will be described later (Section 1.2). This difference may be a result of increased hydration or of thickness effects alone.

1.1.4 Film Ageing

Both nickel hydroxides and oxy-hydroxides can undergo a variety of irreversible changes with time. Amorphous phases tend to crystallize, the α-phase dehydrates to the β(II) phase, the β(III) phase converts to the γ phase, and the oxy-hydroxides can self-discharge to form hydroxides. Little is known about the mechanisms of these processes, and charge/discharge cycling can give rise to complex film structures in which several of the above processes occur simultaneously.

Fresh cathodically deposited hydroxide films can be relatively amorphous[12]. However, according to Briggs and Wynne-Jones[34], a charge/discharge cycle transforms an amorphous hydroxide to a partially crystalline nickel hydroxide, with lower current densities yielding a slightly more crystalline film. Vacuum desiccation or heating a fresh precipitate also promotes crystallinity. Their results suggest that amorphous films transform rather quickly to the more ordered (α) structure, especially at higher temperatures. Therefore, film crystallinity might not be expected to have significant effects on the electrochemical properties of nickel battery electrodes, except perhaps during the very early stages of cycle life.

However, this idea has been challenged. Some authors[38] believe that crystallization is slow, and that it causes hydroxide films to change from being electrochemically active to inactive. Crystallization is associated with hydrogen bond breakage between lattice layers, and proton diffusion rates (perpendicular to the lattice layers) are reduced.

The crystallinity of electro-oxidized nickel electrode films has not been addressed in the literature. Thin β(II) films are assumed to be crystalline in this work.

Perhaps the most widely recognized ageing process is that of the dehydration of α- to β-$Ni(OH)_2$. The α phase will dehydrate spontaneously in KOH solutions or during charge/discharge cycling. Dehydration is faster in more concentrated KOH solutions[17,39]. However, the α phase may reappear[20] during discharging of γ-NiOOH. MacArthur[17] found that some α-$Ni(OH)_2$ was always present with the β(II) phase during his cyclic voltammetry experiments.

The ageing of β- to γ-NiOOH has not been discussed in the literature to any great extent. Arvia et al.[39] consider it to be a chemical process involving no change in oxidation state but they did not speculate on the mechanism. However, it could be expected to involve the incorporation of the various electrolyte species into the crystal structure.

The self-discharge of the oxy-hydroxides can also be classified as an ageing process. The potential/pH diagram (Figure 1) indicates that oxygen evolution can occur at lower potentials than oxidation of nickel hydroxide. Oxygen evolution proceeds slowly on nickel hydroxide films, and large overpotentials are required for appreciable oxygen evolution currents. However, a charged electrode does have a thermodynamic tendency to reduce itself by oxidizing water or hydroxide ions. Discharging is slow but alkaline battery electrodes need periodic recharging if left to stand at open circuit.

1.1.5 Electronic Properties

The literature relevant to the electronic properties of the passivated nickel electrode often does not distinguish between nickel oxide, NiO, and the nickel hydroxides. Similarly, electronic property differences between the α and β(II) forms, or β(III) and γ forms have not been reported. NiO exhibits the NaCl lattice structure, while the nickel hydroxides have a hexagonal layer lattice structure. This alone could result in significant differences between the two materials. The nickel hydroxides can be polycrystalline or amorphous, and can age as described earlier, but these features have not been treated. Clearly, the characterization of the electronic properties of nickel films is

far from complete. The electronic properties of nickel hydroxide are often assumed to be similar to those of lithiated NiO which is a p-type semiconductor under ambient conditions.

Nickel electrode films in a variety of basic solutions have been identified as p-type and n-type semiconductors depending on the applied potential. Photocurrent experiments by Madou and McKubre[36] indicate that films at potentials in the hydrogen evolution region are p-type like lithiated NiO films. Wilhelm and Hackerman[47] also find p-type semiconduction over the lower range of passive potentials. Madou and McKubre find n-type behavior at higher potentials in the β(II)/β(III) "charge region." Thermoelectric power measurements by Tuomi[12] also indicate n-type conduction for β(III) films, but he describes nickel hydroxide films at lower potentials as insulators. Glarum and Marshall[21] also find insulating properties at potentials near the region of hydrogen evolution. In contrast, Madou and McKubre[36] indicate that β(II) films have a high electronic conductivity. This seems likely in view of the photo-current experiments and also the appreciable hydrogen evolution currents observed on nickel hydroxide films at sufficiently negative potentials.

Mott-Schottky plots for nickel electrodes in alkaline solutions have been reported by a number of investigators [36,43,45,47]. Data for the capacitance, C as a function of potential were obtained using impedance techniques. A linear C^{-2} versus potential region is observed in each case, but over varying potential ranges, and only at lower potentials where nickel hydroxide is the stable film. The linearity of the Mott-Schottky plots suggests that a depletion type space charge layer exists within the film. Values of the space charge capacitance observed in alkaline solutions are relatively large compared with those observed for other semiconductors.

The slopes of the Mott-Schottky plots are small and negative. The negative slopes confirm that the majority carriers are holes [36,47], and their magnitudes indicate that β(II) films have very high carrier, and acceptor, concentrations. Large acceptor concentrations are found to diminish the space charge layer thickness in highly doped NiO[45], and presumably in nickel hydroxide. Since space charge layer thickness and capacitance are inversely related, the large space charge capacitances reported for hydroxide films in

basic solutions[36] can be rationalized. The space charge capacitance normally is smaller than the double layer capacitance for a semiconductor, and consequently dominates the overall capacitance[45,48].

The preceding discussion involved only electronic space charges. Space charges from uncompensated ionic defects can also occur, and can have important effects on the electrochemistry of anodic films[49,50]. Although no ionic space charges have been proposed for nickel films formed in alkaline solutions, they will be considered later in this report. However, it is important to note that simple point defect models are probably not applicable to the highly defective layer lattice structures of the nickel hydroxides and oxy-hydroxides[51].

1.2 The Electrochemistry of Nickel in Alkaline Solution

Electrochemical studies of nickel electrodes in alkaline solution have demonstrated the complexity of the system. The literature is replete with cyclic voltammograms, and to a lesser extent, complex plane impedance diagrams. Many characteristics of the system remain debatable or irreproducible, although significant progress towards an understanding of the system has been made.

The following summary is restricted to the literature concerning the ac impedance and cyclic voltammetric behavior of nickel electrodes in alkaline solutions.

1.2.1 Cyclic Voltammetry

The various crystalline film structures and their ageing characteristics were outlined in previous sections. To a first approximation, the phases are found to undergo chemical and electrochemical transformations that obey a square reaction model [19,20] (Figure 2). The vertical arrows in Figure 2 indicate chemical "ageing" transformations, while the horizontal arrows indicate electrochemical processes, as discussed below. The model neglects diagonal reactions which have been observed by two authors[13,19].

The electrochemical processes in Figure 2 give rise to current peaks in potential sweep experiments. The most commonly reported cyclic voltammogram

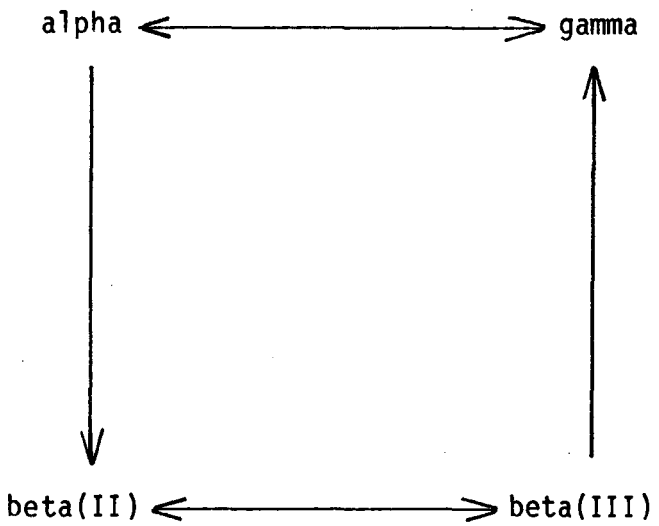

Figure 2. Square reaction model[19].

for nickel electrodes in alkaline solutions shows a single anodic peak and a single cathodic peak, corresponding to the oxidation of $Ni(OH)^2$ to NiOOH and the conjugate reduction reaction, respectively[3,15]. This is often reported as the "steady-state" voltammogram which is observed after a number of cycles. However, numerous other peaks in the immediate vicinity of the above peaks are sometimes reported[18,19]. In an extreme case, six anodic peaks and four cathodic peaks were reported[52]. Multiple peaks and peak splitting are indicative of more than one operative electrochemical process, in support of the reaction model in Figure 2. Such peaks are consistently observed with a potentiodynamic ageing technique described in several papers[22,39,42], but this procedure is not always required to observe peak multiplicity[17,18]. A number of variables may be important including pH, temperature, film preparation and structure, potential sweep rate, and anodic switching potential.

As suggested above, the α/γ and β (II)/β (III) couples give rise to anodic and cathodic current peaks at different potentials. Triple anodic or cathodic peaks are though to indicate structural variations of the various phases shown in Figure 2 or diagonal reactions[42].

Barnard and Randell[53] maintain that the peak potentials of the two electrochemical couples in Figure 2 are principally determined by the reversible potentials of the couples. The α/γ couple has the lower reversible potential at any pH, and therefore from a purely thermodynamic view point, should oxidize at less anodic potentials[41]. However, in a later paper[13], they caution against using peak potentials for phase couple identification. Subtle variations in structure were observed to change peak positions by as much as 50 mV. They still maintain that peak positions are largely determined by the thermodynamic properties of the phases, but admit that kinetic factors must also influence the voltammogram shapes.

The earlier papers by Barnard et al.[41,53] suggest that these two electrochemical couples are under complete diffusion control in conjunction with fast charge transfer kinetics and Nernstian reversibility. The cyclic voltammetric experiments of Meier et al.[39] also indicate that there is no appreciable charge transfer overpotential associated with the oxidation of hydroxides to oxy-hydroxides. They conclude that the electrochemical reactions indicated in Figure 2 are in "quasi-equilibrium." However, there is substantial evidence in several papers dicussed below that the assumption of complete electrochemical reversibility may be an oversimplification, and that film thickness appears to be an important variable[19].

The diagnostic criteria for electrochemical reversibility in cyclic voltammetry experiments involve the dependence of the peak potentials and peak currents on sweep rate[54,55]. However, the chemical transformations indicated in Figure 2 for the α and β (III) films cause peak potential shifts with time at a given sweep rate, perhaps because of the change in reversible potential. Similarly, peak current densities can be affected. These effects complicate the interpretation of the voltammograms, making it difficult to determine whether a given electrochemical couple is reversible. Potential and current peak shifts at a constant sweep rate are observed even without the appearance

of multiple anodic and cathodic current peaks. In most cases, relatively stable voltammograms are eventually recorded[22], but only after a large number of cycles although the number varies with temperature[39]. Typically, anodic peak potentials decrease during the first few cycles, and later increase before reaching a steady state. Cathodic peak potentials tend to decrease slowly during cycling[39]. The film structure can become quite complex as subsequent potential sweeps begin before ageing processes are completed. In addition to ageing effects, it has been found that repetitive potential cycling increases the total film thickness substantially[23,59].

Clearly, ageing and film thickening effects influence the interpretation of sweep rate dependent peak shifts. Reversible behavior (diffusion control) has been indicated by the sweep rate dependence only for low KOH concentrations and thick cathodically deposited films[17,19]. Diffusion control has also been observed for thick films in potential step studies[24,37]. For electro-oxidized films which are generally thinner, the peak current varies almost linearly with sweep rate, and the peak potential also shows a variation with sweep rate[42]. This behavior has been attributed[19] to the influence of charge transfer on the rate of the electrochemical reactions shown in Figure 2. However, it is important to realize that an electrode may exhibit reversible behavior at low sweep rates but conform to activation control at higher sweep rates. The above results are therefore valid only over the range of sweep rates employed in the respective experiments. Nevertheless, the literature does show that thicker films exhibit reversible behavior to higher sweep rates than do thin films. This is emphasized in the case of thin films by an increase in the separation between the conjugate anodic and cathodic current peaks with increasing sweep rate, further indicating a lack of reversibility in the associated reactions.

In summary, the electrochemical reaction rates on thin film electrodes are usually found to be controlled at least in part by charge transfer kinetics, while thick film electrodes generally show reversible behavior.

1.2.2 AC Impedance Spectra and Equivalent Circuits

Relatively few investigators have published ac impedance spectra for nickel electrodes in alkaline solutions. In most of these studies, the

frequency range was restricted due to limitations of the instrumentation [21,45,60,61]. Impedance data for porous battery electrodes are available, but in most cases values of the cell impedance are reported rather than those for the single electrode[62,63]. Some planar electrode data have been published, but virtually all the data were obtained for thick or porous films[21,36].

Complex plane plots of both thick film planar and porous battery electrode impedance data exhibit a semicircle at high frequencies and a second arc at lower frequencies. The lower frequency behavior has been shown to arise from a diffusion controlled process[36,62]. For thick film planar electrodes, the high frequency semicircle becomes smaller and essentially disappears at higher potentials[37]. The similarity between the impedance data for planar thick film electrode impedances and porous battery electrodes indicates that either thick films are porous or porosity does not influence the impedance spectra. The frequency dispersion of thin film impedance spectra are not available for comparison.

Planar electrode impedance data presented later and corresponding data from the literature were analyzed in terms of generalized equivalent circuits for film-covered electrodes in an aqueous solution. The equivalent circuits proposed here were deduced from both original and review papers on the ac impedance technique. However, as with any equivalent circuit, no claim of uniqueness can be made[64]. In the simpler cases, impedance data can be represented as passive RCL, RC, and/or RL networks in a variety of parallel or series combiantions. However, a good model will be physically descriptive of real electrode processes, and the position of the components in the circuits should take into consideration their physical location in the electrochemical system.

Even with the possibilities realized by the circuit networks above, many electrochemical systems can not be modelled adequately without an additional circuit component known as the Warburg impedance which is associated with diffusion processes in these systems.

A generalized equivalent circuit for a film-covered electrode is shown in Figure 3. The circuit shown does not allow for space charges in the film,

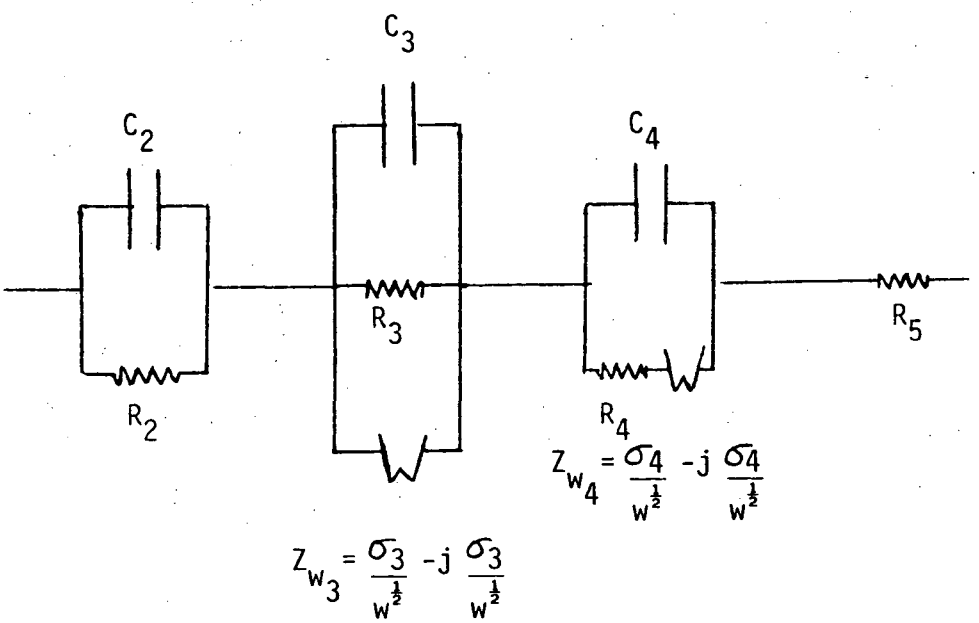

Figure 3. Generalized equivalent circuit.

electronic surface states at either interface, or any adsorption at the film/electrolyte interface. Generally, the resistance of the metal phase and the lead wires from the associated electronic circuitry is sufficiently small to be neglected.

The impedance of the metal/film interface can be represented by a parallel circuit comprised of R_2 and C_2. The capacitance represents the separation of ionic and/or electronic charge across the metal/film interface[50]. The resistance is a leakage path for charge transfer across the interface. While a parallel RC circuit is often used to represent the impedance of an interface, it can be a gross over-simplification when a semi-conductor phase is present. A variety of relaxation processes involving surface states, deep traps, and inhomogeneous doping, can occur, causing a distribution of relaxation times. More complex models have been proposed[71], but in cases involving a semi-conductor phase, the film/solution interface properties usually dominate the electrochemical properties of a system.

The impedance of the film is represented by a parallel combination of three components: the geometric capacitance, C_3, associated[65] with the dielectric constant of the film, the film resistance, R_3 corresponding to the transfer of electronic current through the film, and the Warburg impedance, Z_{w3} arising from the mass transfer of ionic species through the film. The Warburg impedance for a semi-infinite diffusion layer is given by

$$Z_{w3} = \sigma/\omega^{1/2} - j(\sigma/\omega^{1/2}) \tag{1}$$

where

$$\sigma = \frac{RT}{2n^2F^2}\left(\frac{1}{C_0D_0^{1/2}} + \frac{1}{C_RD_R^{1/2}}\right) \tag{2}$$

The subscripts O and R indicate oxidized and reduced species, respectively. For films, the semi-infinite diffusion layer assumption may not be satisfied, and equation (1) must be replaced by a more complex expression[66].

The Randles equivalent circuit[67] may be chosen to represent the film/electrolyte interface. The component C_4, represents the double layer capacitance which is in parallel with a series combination of a charge transfer resistance, R_4, and a Warburg impedance, Z_{w4}. The latter allows for the mass transport of electrolyte species to (from) the interface before (after) charge transfer.

Finally, the electrolyte can be represented simply by a resistance, R_5 which is the solution or uncompensated resistance between the reference electrode and the film/electrolyte interface.

The geometric capacitance of the film, C_3, will probably be small, but since the film dielectric constant and thickness are not accurately known, C_3 is retained in the circuit. However, Cahan[69] indicates that the relaxation of the film geometric capacitance usually occurs above 5 kHz.

Impedance, potential step, and cyclic voltammetry studies of nickel electrodes in alkaline solution indicate that the circuit should be modified. In particular, the space charge capacitance (discussed previously in Section 1.1.5) has not been included, and a resistance in parallel with the space charge capacitance is also required[48] since small dc electronic currents can flow across a space charge region. A space charge region exhibits diode characteristics, so the value of the resistive impedance is dependent on the direction of dc current flow. Under reverse bias, the resistance will be much larger[76] than R_3. Electroactive ionic species may also be transported across the space charge layer, giving rise to another Warburg impedance which may have a different coefficient, σ, from that for the rest of the film.

If the space charge region is treated as a separate film layer, then the space charge components, C_3', R_3' and Z_{w3}' can be placed in the circuit as shown in Figure 4. Tench and Yeager[45] use this approach, but in place of a Warburg impedance, they use an RC series circuit to represent electronic surface states.

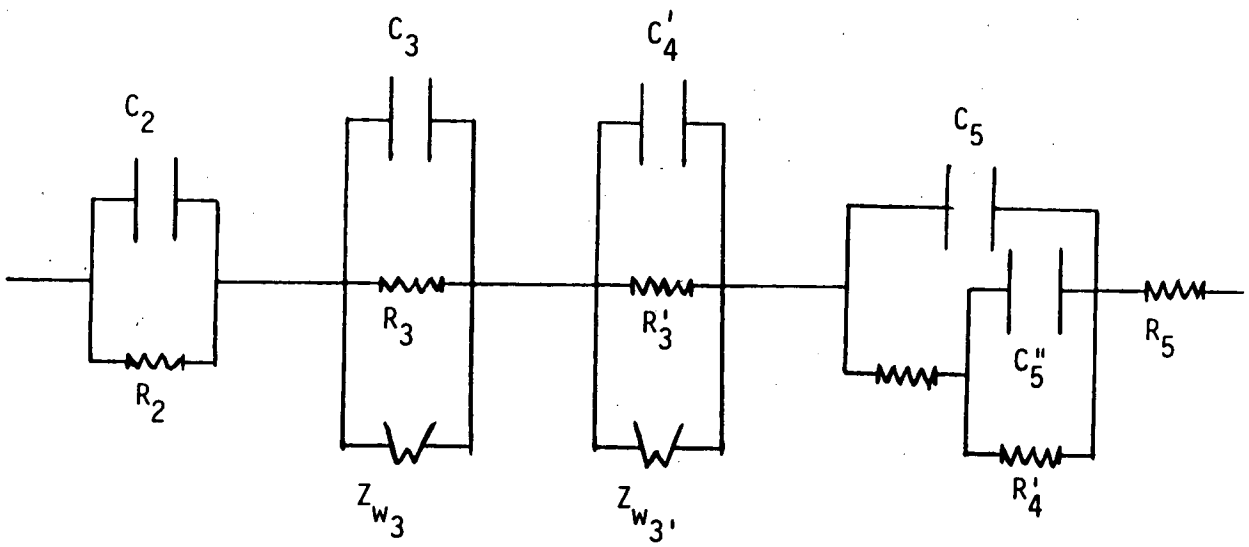

Figure 4. Equivalent circuit allowing for all relaxation processes indicated in the literature on nickel electrodes in alkaline solution.

Values of the double layer capacitance for metal/electrolyte systems with and without films present are typically found[70] to lie within the range 50 to 100 $\mu F/cm^2$. The Mott-Schottky plots given by Madou and McKubre[36] for a nickel electrode in 6.25 molal KOH indicate values of the measured capacitance generally below this range, suggesting that the capacitance is mainly associated with the space charge layer[21]. However, at higher potentials (0-400 mV vs. SHE), the magnitude of the measured capacitance is typical of that for a double layer capacitance, and the Mott-Schottky plot deviates sharply from linearity at these potentials [36]. However, DeGryse et al.[72] show that a series double layer capacitance should not affect the linearity of a Mott-Schottky plot[73].

At still higher potentials where oxy-hydroxide films are formed, values of the capacitance as large as 8000 $\mu F/cm_2$ were reported by Glarum and Marshall[21]. These workers indicated grain boundary effects may be important. However, these high values may reflect the presence of of a pseudo-capacitance associated with the accumulation of adsorbed species at the interface. Values of the pseudo-capacitance as large as 2000 $\mu F/cm^2$ have been reported for other electrochemical systems[74]. A psuedo-capacitance is therefore a viable candidate to explain a large capacitance at high potentials on a nickel electrode. In addition, pseudo-capacitive effects have been proposed[63] to account for the impedance data for porous nickel electrodes.

In the case of an equivalent circuit for a metal/electrolyte interface, a pseudo-capacitive circuit element C_4', and its associated parallel resistance, R_4', are placed[73,74] in parallel to the double layer capacitance as shown in Figure 4. When a film/electrolyte interface is involved, there is some justification for placing the pseudo-capacitance in the film section of the circuit, but for the present work, C_4' and R_4' were positioned with the interfacial components.

Impedance experiments with rotating disk nickel electrodes in KOH solutions have shown that impedance spectra are unchanged by electrode rotation speed[21,36]. This indicates that the diffusion of electroactive species in the electrolyte is a relatively fast process, and it is therefore not necessary to include the solution Warburg impedance, Z_{w4} in the equivalent circuit.

Accordingly, the modified equivalent circuit shown in Figure 4 is proposed to represent the impedance of the nickel/alkaline solution system. The circuit remains complex despite the simplifications. The impedance spectra reported by Madou and McKubre[36] show a remarkable simplicity, indicating that other refinements to the modified circuit shown in Figure 4 are in order. A discussion of such refinements is deferred to a later section to allow the impedance results from this work to be considered.

1.3 Porous Nickel Electrodes

A number of processes involving irreversible degradation affect the performance of porous nickel battery electrodes. Like all porous electrodes, nickel plates can exhibit electrolyte exhaustion within the pores leading to mass transport and ohmic overpotential losses which reduce cell power. Faradaic efficiency losses from cycle- and temperature-dependent parasitic processes such as oxygen evolution can reduce charging efficiency. Also, the structural integrity of porous nickel electrodes may be inadequate to withstand the mechanical stresses which arise during charge/discharge cycling. These stresses can result in both a degradation in the electrical resistance of the substrate particle-particle bonds and a slow separation of the active material from the current collector, often accompanied by a swelling of the porous mass.

Each degradation process can cause a gradual decline in the cell performance. However, it is often difficult to attribute the overall loss in performance to a specific process, and the major objective of this study was to determine the main processes causing degradation of porous nickel electrodes.

1.3.1 Transmission Line Model

An understanding of the electrochemical properties of a porous electrode, and of how these properties are altered by internal damage, can be achieved if a suitable model is adopted. In this study, a transmission line model is used to represent the porous electrode. The model is based on the work of DeLevie [78,79] but has been modified in two important ways. Firstly, the model developed here recognizes the finite thickness of a practical battery

electrode. Accordingly, the electrochemical behavior of the porous mass will be partly determined by processes which occur at the base of the pore between the current collector (backing plate) and the solution (impedance Z', Figure 5). Secondly, the model assumes a finite resistance for the metal phase in order to take into account the resistive degradation of metal particle-particle contacts caused by internal stresses.

As with other porous electrode models, several simplifying assumptions are made. In the case of the transmission line model, the pores are assumed to be straight, parallel, and cylindrical. Radial and axial concentration gradients of electrolyte within the pores are neglected, and an average pore electrolyte resistance is used. Similarly, an average metal phase resistance between pores is used. A uniform layer of active material is assumed to line the walls of the pores. Charge storage processes along the walls are represented by the interacial impedance, Z. In this work, a potential-dependent equivalent circuit representing the interfacial impedance, Z, and the backing plate impedance, Z', are deduced from impedance data for a planar nickel electrode.

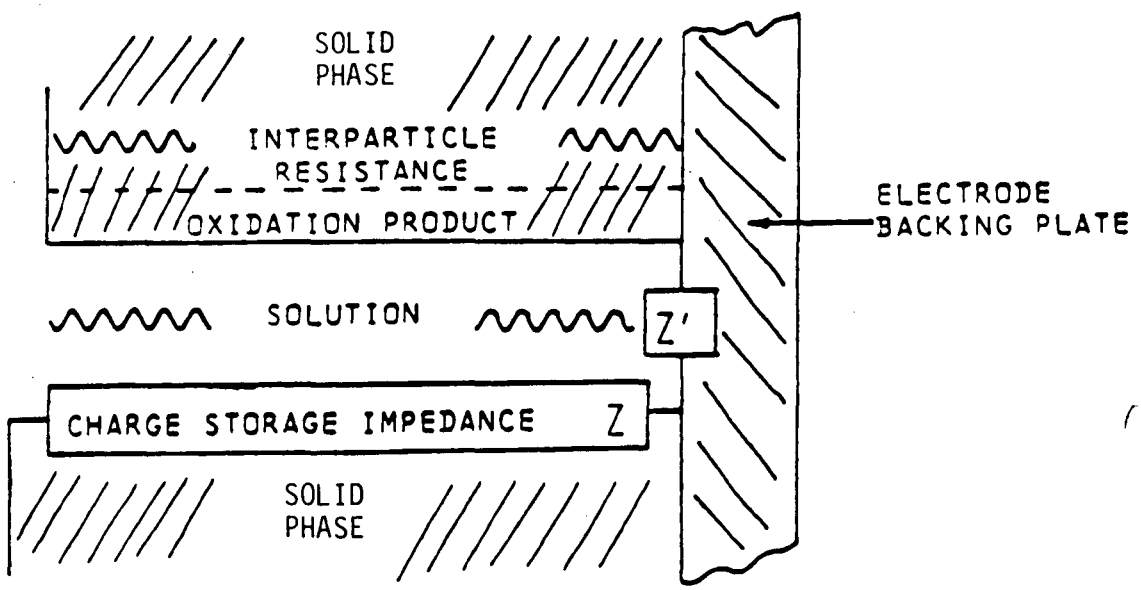

Figure 5. Model of ideal single pore.

Although details of the transmission line model derivation have been published previously[80,81], they are reproduced here since the model forms the basis of this study. The equivalent circuit for a single pore is represented by a finite form of the transmission line model, as shown in Figure 6, in which R_m and R_s represent the resistance of the particle phase in electrical contact with the current collector at the pore base, and the resistance of the solution phase per unit pore length (Ω/cm), respectively. The interficial impedance, Z, is a specific impedance per unit pore length having units of Ω cm, and Z/dx is therfore expressed in ohms. The current collector or backing plate impedance Z' has units of ohms, and is independent of pore length.

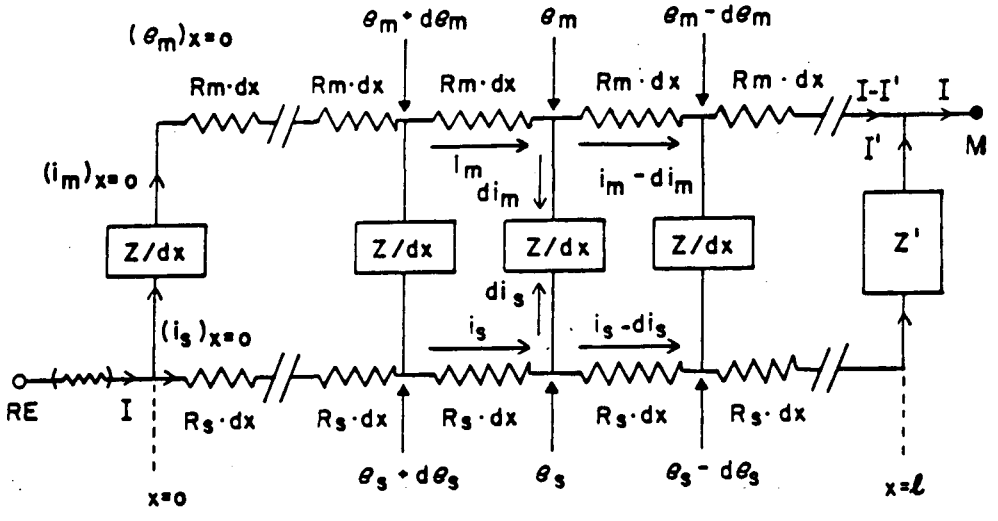

Figure 6. Discretized form of transmission model for a porous battery electrode of finite thickness.

e_m and e_s are potentials in the solid and solution phases, respecively.

i_m and i_s are currents in the solid and solution phases respectively.

I and I' are the total current and the current flowing across the electrode backing plate/solution interface at the base of the pore, respectively.

RE and M designate the reference electrode and current collector locations, respectively.

The current and potential distributions within the porous system, and the total impedance, can be derived by the application of circuit analysis equations to a typical discrete unit. Accordingly,

$$I = i_m + i_s \tag{3}$$

$$-de_m = i_m R_m dx \tag{4}$$

$$-de_s = i_s R_s dx \tag{5}$$

$$\phi = e_m - e_s = di_s(Z/dx) = -di_m(Z/dx) \tag{6}$$

Using equations (3) to (6), and assuming Z, R_m, and R_s to be independent of x, the following differential equations can be obtained:

$$\frac{d^2 i_m}{dx^2} - \gamma i_m + \frac{R_s}{Z} I = 0 \tag{7}$$

$$\frac{D^2 i_s}{dx^2} - \gamma i_s + \frac{R_m}{Z} I = 0 \tag{8}$$

$$\frac{d^2 \phi}{dx^2} - \gamma \phi = 0 \tag{9}$$

where $\gamma = \frac{R_m + R_s}{Z}$

The three second order differential equations in i_m, i_s, and ϕ must be solved subject to the following boundary conditions:

$$x = 0;\ i_s = I,\ i_m = 0,\ \frac{dd}{dx} = R_s I \text{ (mouth of the pore)}$$

$$x = \ell;\ i_s = I',\ i_m = I - I',\ e_m = 0,\ e_s = I'Z',$$

$$\phi_{(x=\ell)} = -I'Z' \text{ (base of the pore)}$$

The solutions to differential equations (7), (8) and (9) are

$$i_m = c_1 \exp(-\gamma^{1/2}) + c_2 \exp(\gamma^{1/2}x) + \frac{R_s I}{\gamma Z} \tag{10}$$

$$c_2 = \frac{1}{2\sinh(\gamma^{1/2}\ell)} \quad \frac{R_m I + R_s \exp(-\gamma^{1/2}\ell)}{\gamma Z} - I'$$

$$c_1 = -c_2 - \frac{R_s I}{\gamma Z} = \frac{-1}{2\sinh(\gamma^{1/2}\ell)} \quad \frac{R_m I + R_s I \exp(\gamma^{1/2}\ell}{\gamma Z} - I'$$

$$i_s = -c_1 \exp(-\gamma^{1/2}x) - c_2 \exp(\gamma^{1/2}x) + \frac{R_m I}{\gamma Z} \tag{11}$$

$$\phi = c_1' \exp(-\gamma^{1/2}x) - c_2' \exp(\gamma^{1/2}x) \tag{12}$$

$$c_2' = \frac{1}{2\cosh(\gamma^{1/2}\ell)} \quad \frac{R_s I \exp(-\gamma^{1/2}\ell)}{\gamma^{1/2}} - I'Z'$$

$$c_1' = \frac{1}{2\cosh(\gamma^{1/2}\ell)} \quad \frac{R_s I \exp(\gamma^{1/2}\ell)}{\gamma^{1/2}} + I'Z'$$

The potential drop between the current collector and the mouth of the pore is given by

$$V = -\phi_{(x=\ell)} + \int_0^{\ell} R_s i_s \, dx = -\phi_{(x=0)} + \int_0^{\ell} R_m i_m dx = e_{x(x=0)} - e_{m(x=\ell)} = I'Z_p$$

where Z_p is total impedance of a single one-dimensional pore.

$$I' = \frac{1}{Z'} \cdot \frac{R_s+R_m C}{\gamma^{1/2} S+\delta C} \cdot I$$

$$Z_p = \frac{R_m R_s \ell}{R_m+R_s} + \frac{2\gamma^{1/2} R_m R_s+\gamma^{1/2}(R_m^2+R_s^2)C+\delta R_s^2 S}{\gamma^{1/2}(R_m+R_s)\ (\gamma^{1/2} S+\delta C)} \qquad (13)$$

where $\gamma = \frac{R_m+R_s}{Z}$, $\delta = \frac{R_m+R_s}{Z'}$, $C = \cosh(\gamma^{1/2}\ell)$, $S = \sinh(\gamma^{1/2}\ell)$

Since the pores are in parallel, the total impedance of the porous electrode (Z_t) is

$$Z_t = Z_p/n = \frac{1}{n}\ \frac{R_m R_s \ell}{R_m+R_s} + \frac{2^{\ 1/2} R_m R_s +^{\ 1/2}(R_m^2+R_s^2)C+ R_s^2 S}{^{1/2}(R_m+R_s)\ (\ ^{1/2} S+ C)} \quad \text{(ohm)} \qquad (14)$$

where n is the number of pores per unit area.

Equation 14 represents the total impedance of n one-dimensional pores. Several simple modifications to the parameters R_m, R_s, Z and Z' allow the equation to be extended to a three- dimensional system[81]. If it is assumed that a porous film uniformly covers the current collector of area A, and $(1-\theta)$ is the fraction of that area occupied by pores, then $(1-\theta)A/n$ is the average area of the entrance to a pore. The solution phase resistance per pore becomes $\rho_s n\ell/(1-\theta)A$, and the resistance of the solid phase carrying current is $\rho_m n\ell/ A$, where ρ_s and ρ_m are the resistivities (Ω cm) of the solution and solid phases carrying respectively, and ℓ is the pore length. The parameters R_s and R_m in Figure 6 are the corresponding resistances per unit pore length. Therefore,

$$R_s = \rho_s n/(1-\theta)A \ (\Omega/cm) \qquad (15)$$

$$R_m = \rho_m n/\theta A \ (\Omega/cm) \qquad (16)$$

If the specific impedances (Ω cm^2) of the pore wall and pore base are Z_w and Z_b, respectively, then the impedance of the pore wall and pore base per pore are $Z_w/2\pi r\ell$ and $Z_b/\pi r^2$, respectively, where r is the average pore radius. Since the average pore area, πr^2, is $(1-\theta)A/n$, then r is given by

$$r = \frac{(1-\theta)^{1/2}A^{1/2}}{(n\pi)^{1/2}} \text{ (cm)} \tag{17}$$

Using equation 17, the three-dimensional impedance of the pore wall per pore and per unit pore length is

$$Z = \frac{Z_w\ell}{2\pi r\ell} = \frac{Z_w n^{1/2}}{2\pi^{1/2}(1-\theta)^{1/2}A^{1/2}} \tag{18}$$

Similarly, the backing plate or current collector impedance Z'is given by

$$Z' = Z_b/\pi r^2 = Z_b n/(1-\theta)A \tag{19}$$

The above expressions for R_m, R_s, Z, and Z', now in a three-dimensional form, are used in Equation 14. The expressions for Z_w and Z_b are determined from planar electrode impedances as discussed later in Section 4.

2.0 EXPERIMENTAL TECHNIQUES

2.1 Test Cell

A teflon cell (Figure 7) was used since glass is subject to attack by alkaline solutions. The cell was provided with input ports for the electrolyte solution, high purity argon to purge the solution, and a copper/constantant thermocouple. The purging gas was deoxygenated by bubbling it through vanadyl sulfate[85], passed through the cell, and vented through an output port.

An 8 molal KOH solution containing 1% LiOH was used as the electrolyte in all experiments. The solution was prepared from reagent grade KOH and LiOH together with double-distilled, demineralized water. All solutions were purged with argon in a solution reservoir for a minimum of two days prior to any experiment. This procedure was required for reproducibility in the impedance experiments. An 8 molal solution was selected even though the maximum conductivity of KOH solutions occurs[86] at a concentration of about 5 molal. The higher concentration is used to prevent freezing at lower temperatures. The LiOH was added so as to be consistent with battery cycling experiments reported in the literature. The addition of lithium is usually regarded as beneficial to the performance of porous electrodes[10,12,15], although recent experiments[87] have shown that lithium has little effect on the capacity during cycling.

A square sheet of platinum was used as a counter electrode. It was positioned directly over and parallel to the surface of the working electrode, as indicated in Figure 7. A small hole in the center provided access for the Luggin capillary to the reference electrode.

A Hg/HgO reference electrode was used in all experiments, and all potentials in this report are given with respect to this reference. A Hg/HgO paste was prepared by intimately mixing the two ingredients in roughly equal proportions. The paste was placed in a teflon container located above the cell, and contact with the electrolyte was provided by cotton fibers in a teflon capillary. No liquid junction correction was required with this

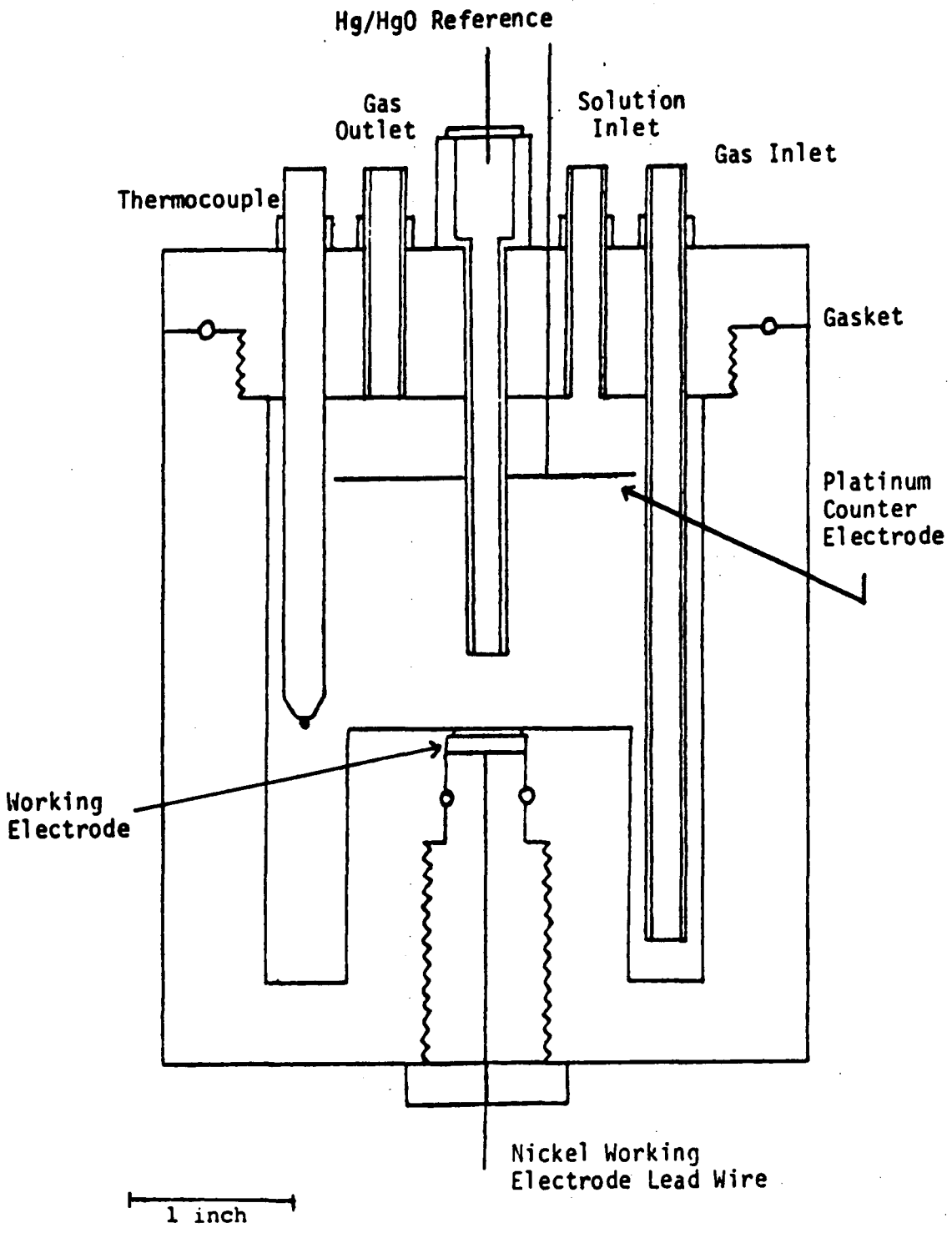

Figure 7. Test cell

arrangement since the reference and working electrodes were in contact with the same electrolyte. The reversible potential of the Hg/HgO electrode can be calculated[88] using equation (20).

$$E = E^\circ - 9.923 \times 10^{-5} T(2 \log m_{KOH \pm} - \log a_{H_2O}) \quad (20)$$

Data for the activity of H_2O, a_{H_2O} and the stoichiometric mean molal activity coefficient, $\gamma_\pm$ as a function of temperature and concentration of alkali hydroxide have been given previously[88]. At 298 K, E° = 0.0984 V and for 8 molal KOH at this temperature, the values of a_{H_2O} and $\gamma_\pm$ are 0.5545 and 5.902, respectively[88].

The same cell arrangement was used for both planar and porous nickel working electrodes. The working electrodes were of three types: planar nickel electrodes, rolled and bonded porous electrodes, and sintered porous electrodes. The preparation of each of these electrodes is described in the following section.

The planar as well as the rolled and bonded electrodes were positioned in the cell by pressing disks of the specimens against a slightly undersized lip with a threaded plug, as shown in Figure 7. An area of 1.27 cm^2 was exposed to the electrolyte. No evidence of crevice corrosion or other edge effects were observed in any experiment.

Sintered electrodes were mounted in the test cell in a similar manner, but were exposed to the electrolyte through a small square opening in a teflon disk placed immediately above the electrode. The exposed area of the sintered porous electrodes was 0.102 cm^2. The smaller area increased the sintered electrode impedance by a factor of ten, allowing an improvement in the accuracy of measurement.

Experiments were performed at temperatures ranging from 0 to 100°C. For all non-ambient temperatures, the test cell was immersed in a heating/cooling bath containing ethylene glycol. The temperature was controlled to within ±2°C, as indicated by the thermocouple inside the test cell.

2.2 Electrode Preparation

2.2.1 Planar Electrodes

All planar electrode experiments were performed with the same nickel specimen. A disk of commercially pure (99.5%) nickel was polished with 0.05 micron alumina powder and then rinsed thoroughly in distilled water. Immediately after the addition of the electrolyte solution to the cell, the sample was polarized. Less than 10 minutes usually elapsed between polishing and polarizing the sample, with only a few seconds between solution contact and polarization. The nickel electrode was repolished prior to each test and fresh electrolyte solution used.

This procedure follows that used in a study[9] to measure the thickness as a function of time at constant potential. The results from that study indicated that polarization for two hours is sufficient to develop a relatively time-independent film thickness. For example, at 0 V, the film thickness is about 15.2 Å after two hours and 16.4 Å after three hours. At 0.5 V, the thickness changes from 42.9 Å to 45.3 Å after two and three hours, respectively. For both potentials, the change in thickness is only about 6% and is considered negligible for this study. Since a steady-state system is required for valid impedance data, planar electrodes were polarized for a full two hours prior to initiating impedance measurements.

2.2.2 Rolled and Bonded Electrodes

The porous electrodes used in this study were prepared by established electrode manufacturers. Detailed preparation procedures are proprietary and were not fully disclosed to the authors of this report. Inquiries about the fabrication of the rolled and bonded electrodes should be referred to Energy Research Corporation, Danbury, Connecticut.

Electrode disks of 1.27 cm diameter were cut from manufactured battery plates. Smaller electrodes could not be cut without significant edge damage. The electrodes consisted of active material on each side of a nickel current collector backing plate. Active material on one side was carefully removed to expose the plate, leaving a half thickness of 0.112 cm. The threaded plug arrangement in the test cell (Figure 7) was used to press a nickel lead wire to the current collector plate.

The active material was supported by a teflon "web". The web comparised only 1 w/o of the total electrode material, with the remainder being 30% graphite, 1% cobalt hydroxide, and the balance nickel hydroxide. The graphite served as the current carrier to the backing plate, and the cobalt was added to increase capacity during cycling[89]. A capacity of 0.29 A-hr/gm was reported, based on a one electron transfer from nickel hydroxide to oxy-hydroxide.

2.2.3 Sintered Electrodes

Little information was available to the authors about the fabrication procedure for the sintered porous electrodes. They were supplied for this work by the Berkeley Laboratory.

The structural features of the sintered electrodes are very different from the rolled and bonded electrodes. In the case of the sintered electrodes, nickel powder is sintered to a nickel wire mesh, and NiOOH is chemically deposited in the pores. The sintered nickel metal (note, not graphite) carries the current to the wire mesh which serves as a backing plate. Planar, square wafers were easily cut from a large battery plate without significant edge damage. The capacity was 0.015 A-hr/cm^2 of projected area.

2.3 Cyclic Voltammetry

Only planar nickel electrodes were studied using cyclic voltammetry. Freshly polished nickel electrodes were inserted into the cell, and upon contact with electrolyte, were immediately polarized to a potential of -0.850 V which is in the hydrogen evolution region. The solution and cell were then heated or cooled to the desired temperature. After achieving temperature stabilization, a Princeton Applied Research Model 175 Universal Programmer coupled to a Princeton Applied Research Model 173 potentiostat was used to impose a triangular potential/time perturbation on the system. Current/voltage curves were obtained using an X-Y recorder, and the data transferred in digital form to floppy diskettes for subsequent analysis by microcomputer. All the potential and current density data on disk were accurate to within ± 3 mV and ±0.5 mA/cm^2, respectively.

Various sweep rates from 1 to 100 mV/s were employed, and the potential was swept from below the hydrogen evolution potential to well above the oxygen evolution potential before reversing the sweep direction. At a given temperature, V/I traces were first recorded at 100 mV/s, then at progressively lower sweep rates. Following the lowest sweep rate, V/I traces were recorded at progressively higher sweep rates up to 100 mV/s.

2.4 ac Impedance Measurements

Impedance data were measured using either a Solartron 1172 or 1250 Frequency Response Analyzer (FRA). Each instrument was linked via an IEEE 488 interface to an Apple II-Plus microcomputer which stored data on floppy disk. Data were normally recorded over a frequency range from 10 kHz to about 5 mHz, and all recorded data was averaged over ten cycles at a given frequency. The 1250 model measures the potential and current simultaneously, whereas the 1172 model measures them sequentially. The measurement time on the latter is approximately twice that of the former (typically 75 minutes compared with 150 minutes for the above frequency range).

A sinusoidal voltage from the FRA was superimposed on an applied dc bias from a PAR Model 173 potentiostat (Figure 8). The potential and current input leads to the FRA were taken directly from the cell. This configuration allows accurate impedance measurements to be obtained irrespective of the frequency response of the potentiostat. A unit gain voltage follower based on an AD 521J amplifier was placed between the cell and the potential input of the FRA to avoid polarizing the reference electrode. The amplifier has a differential input impedance of 3×10^8, and a flat frequency response (±1%) at unity gain to 75 kHz. The voltage follower was accurate to 0.1 mV dc relative to an HP digital voltmeter.

The amplitude of the sinusoidal voltage was 10 mV rms which provided a linear response, as required for valid ac impedance measurements. No deviation from the recorded spectrum at 0.5 V was observed with a 15 mV rms signal, but a small difference was observed using 25mV, and a large difference with a 50 mV perturbation. Second harmonic spectra were always at least one order of magnitude smaller than first harmonic impedance data at the lower

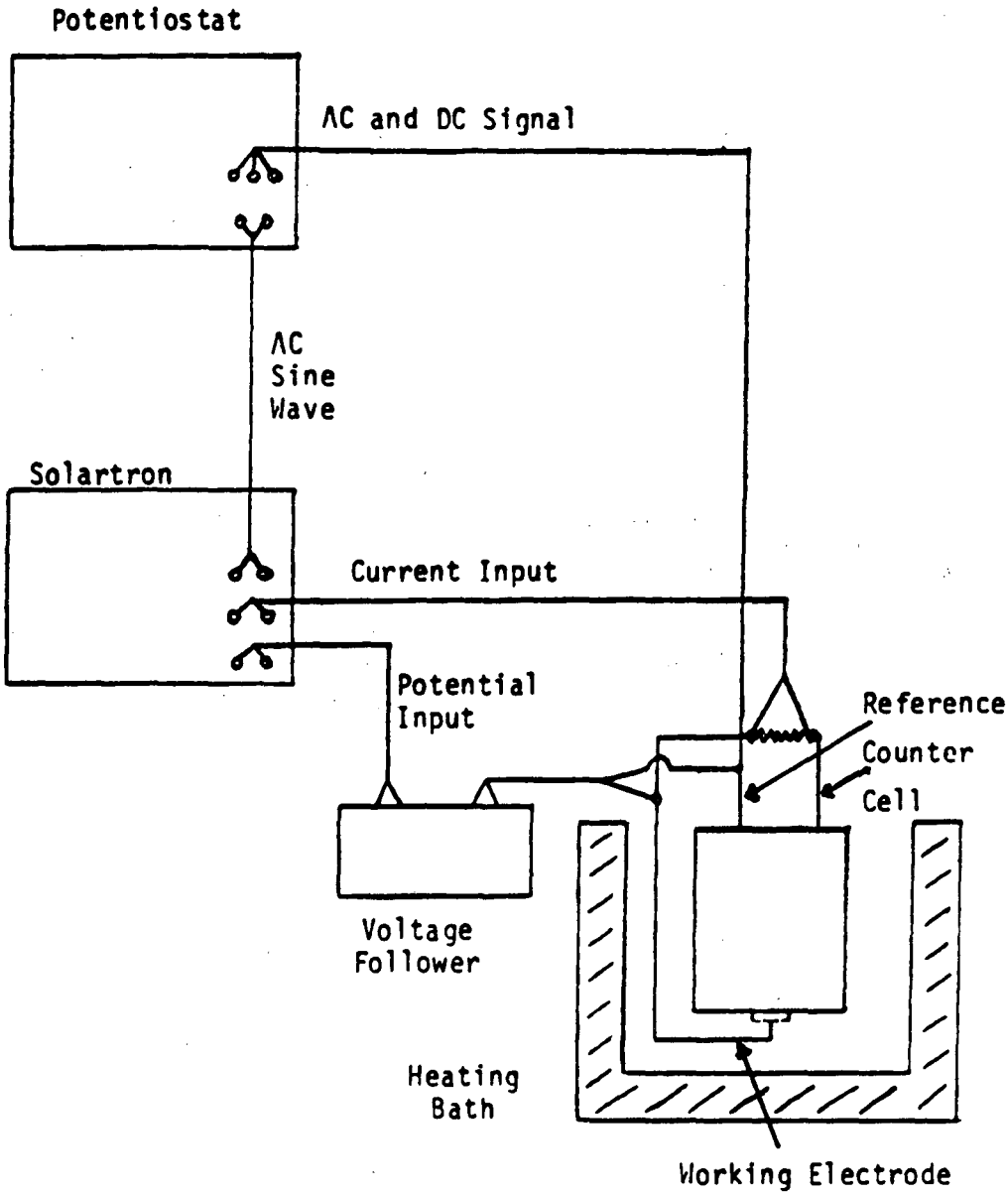

Figure 8. Apparatus used for impedance measurements.

frequencies. Furthermore, by programming the correlator of the FRA to integrate over 10 cycles, noise and harmonics of the fundamental signal are effectively rejected with the resulting long integration times. The impedance of a dummy cell was routinely measured and compared with calculated data to ensure that the FRA and associated circuitry were in proper working condition.

Planar electrode impedance spectra were obtained over a range of dc potentials, in most cases sequentially without repolishing the electrode between measurements. Electrodes were first polarized for two hours at the lowest potential of a given measurement sequence, typically -0.15 V. The impedance spectrum was recorded, followed by a potential step, usually 0.1 V, to the next potential. After one hour, the impedance spectrum at this potential was recorded, and the procedure normally repeated up to about 0.5 or 0.6 V.

Porous electrode impedance data were recorded in either the fully discharged (0 V) or the fully charged (0.5 V) condition. The data were measured periodically after subjecting the electrode to selected numbers of charge/discharge cycles. The cycling process is described below. One hour elapsed at a constant dc potential before impedance spectra were recorded.

2.5 Charge/Discharge Cycling

Porous electrodes were cycled using a constant current from an ECO Model 545 Galvanostat/Electromenter. A range of charging currents was employed, and electrodes were always discharged at twice the charge rate. They were usually charged to 100% of rated capacity, and were fully discharged (100% DOD) on each cycle. Four or five "conditioning" cycles were completed before impedance data were recorded.

Electrodes were charged and discharged at a constant current either for selected time intervals or to selected charge and discharge potentials. The galvanostat had provision for automatic current reversal at selected potentials by pre-setting front panel potentiometers. However, in most cases, it was necessary to use constant charging and discharging times. In this case, two electronic timers were used to control switches connected to charge and discharge trigger inputs on the galvanostat. When the charging efficiency was

end of the set discharge time. A voltage comparator based on an LM 311 amplifier was constructed and included in the timer circuitry to stop the discharging current prematurely at any selected potential. The comparator closed a switch which grounded a reset trigger and stopped the discharging current until the next charging cycle started.

3.0 PLANAR NICKEL ELECTRODES - CYCLIC VOLTAMMETRY

The primary objective in using cyclic voltammetry was to determine the importance of the oxygen evolution reaction during nickel hydroxide oxidation. Oxygen evolution can occur as a parasitic reaction during the charging of nickel battery electrodes, and it may contribute to electrode degradation by generating internal stresses within the electrode pores. The high KOH concentration used in this study serves to increase the importance of the oxygen evolution reaction by decreasing its reversible potential. The influence of this reaction on electrode performance cannot be neglected, especially at higher temperatures.

A number of important electrode characteristics in addition to the features electrode characteristics in addition to the features of the oxygen evolution reaction are described in the cyclic voltammetry results presented here. These results supplement the impedance work described later in Sections IV and V, and contribute to an understanding of the degradation processes occurring on nickel battery electrodes during cycling.

3.1 Results

3.1.1 Ambient Temperature

For many cycling experiments at ambient temperature, only one anodic peak around 0.5 V was recorded prior to the oxygen evolution curve at somewhat higher potentials. A cathodic peak at about 0.3 V was observed on the reverse sweep. Similar voltammograms have been reported for nickel in various alkaline solutions[3,15]. The anodic and cathodic peaks correspond to the oxidation of nickel hydroxide and reduction of nickel oxy-hydroxide, respectively, as discussed in Section 2.3.

At a constant sweep rate of 100 mV/s, no steady state voltammogram was observed even after cycling continuously for over 19 hours (Figure 9). Although the anodic peak currents increased steadily with cycling time (Figure 10), the decreasing slope with increasing cycle time indicates that a steady state voltammogram might eventually be observed.

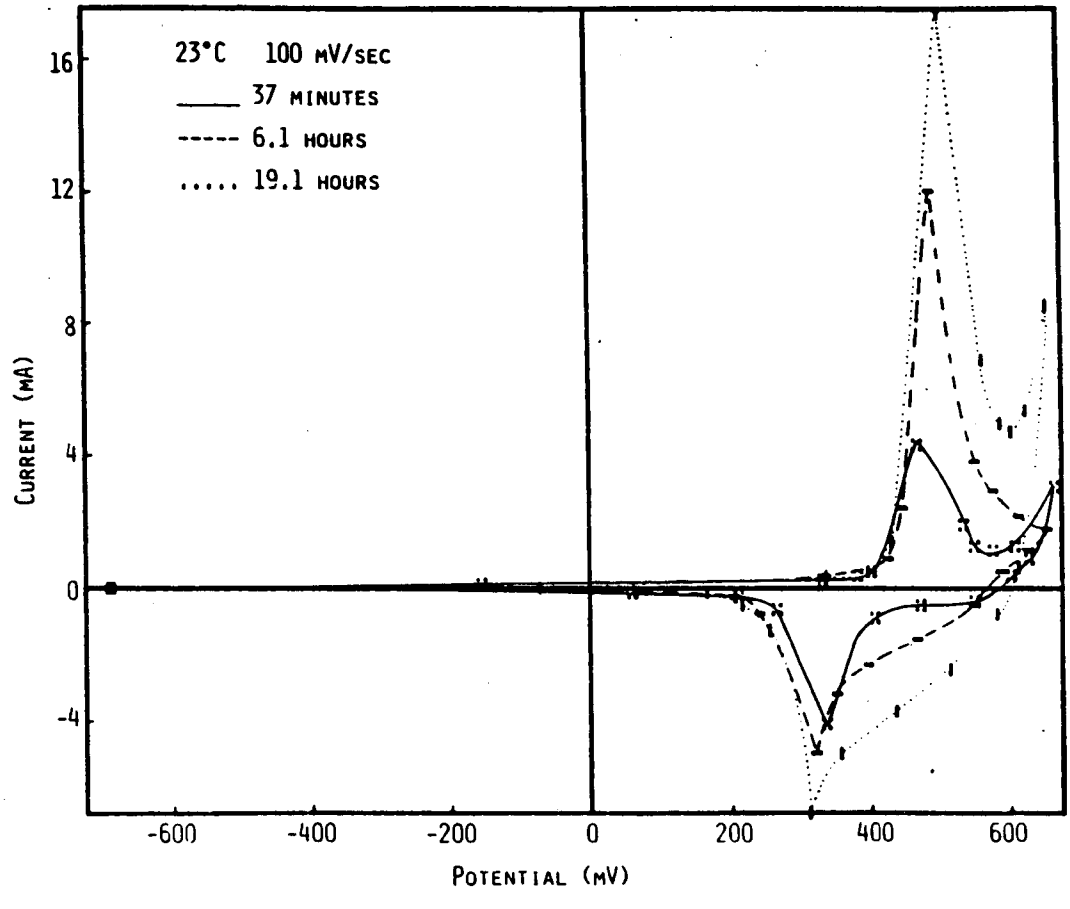

Figure 9. Cyclic voltammograms for a planar Ni electrode after various cycling times.

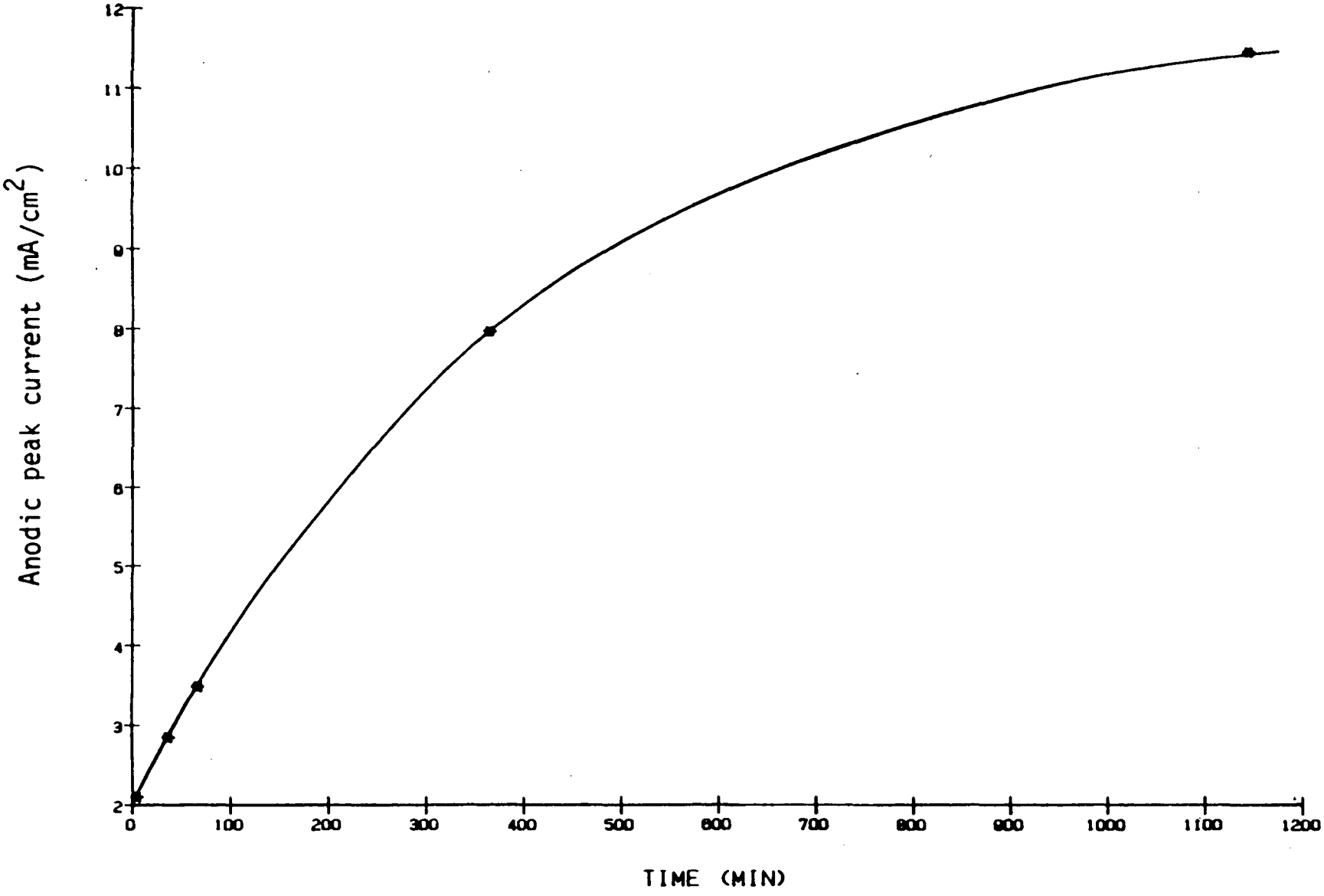

Figure 10. Dependence of anodic peak current on time at 100 mV/s and 23°C.

Cycling time has only a minor effect on the proximity of the $Ni(OH)_2$ oxidation peak to the oxygen evolution curve. Figure 11 shows that the anodic peak potentials initially decrease and then increase with cycling time, in a manner similar to that reported by Meier et al.[39]. The lower curve shows peak potentials after correcting for the IR drop between the reference and working electrodes. The uncompensated resistance at ambient temperature was found to be about 1.5 Ω from the impedance results described later, and the IR drop could therefore be calculated using the peak current density.

In contrast to the anodic data, cathodic peak potentials are low at short cycling times, increase to a maximum and then fall slowly (Figure 12). As a result of the changes of the peak potential with time, the anodic/cathodic peak separations are also time-dependent.

The charge associated with a given anodic peak was determined following the procedure used by Weininger[43], and was found to increase with cycling time (Figure 13). No correction is made for electrode capacitive charging since the electrode capacitance obtained from impedance measurements (Section IV) gives rise to a maximum charging current ($i = Cv$ where v=100 mV/s) of only 0.25 mA at ambient temperature.

The shift in the anodic peak potential with cycling time (Figure 11) can be interpreted most easily by assuming that peak potentials are to a large degree determined by the reversible potentials of the α/γ and β(II)/β(III) couples, as asserted by Barnard and Randell[53]. In view of the lower reversible potential of the α/γ couple, the shift can be explained as an initial increase and subsequent decrease in the mole fraction of the alpha phase in the hydroxide film. This suggests that the β(II)/β(III) couple dominates the electrochemistry after the first few tens of cycles. However, the irreversibility of the $Ni(OH)_2$/NiOOH reaction (Section 1.2.1) indicates that this explanation is an oversimplification.

The peak potentials associated with the film transformation would shift in the anodic direction also if the film thickness increased during cycling. The increasing anodic peak charge (Figure 13) indicates continuing film growth which is further supported by the ellipsometric study by Hopper and Ord[23].

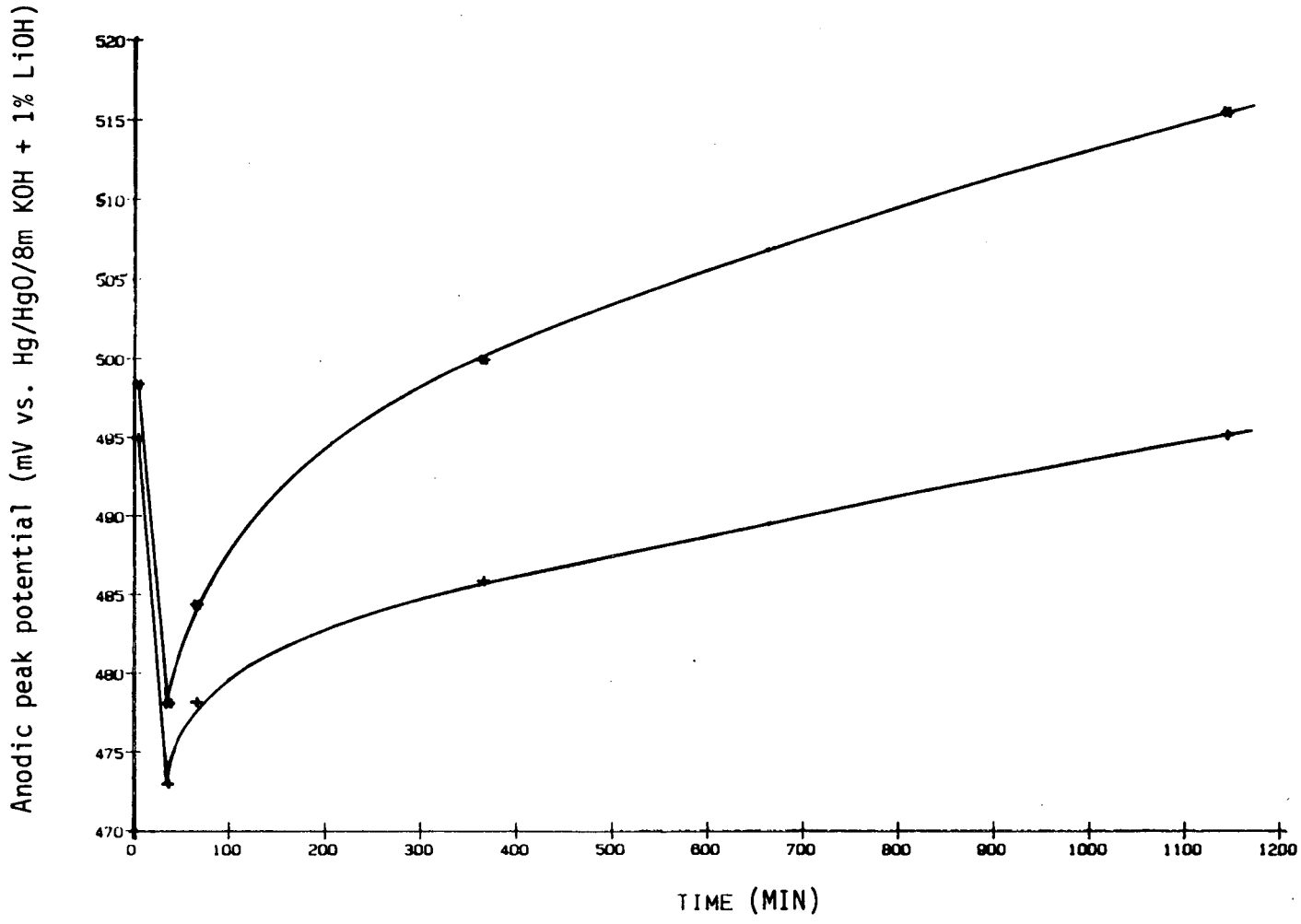

Figure 11. Dependence of anodic peak potential on cycling time at 100 mV/s and 23°C. The symbol + indicates data corrected for the IR potential drop.

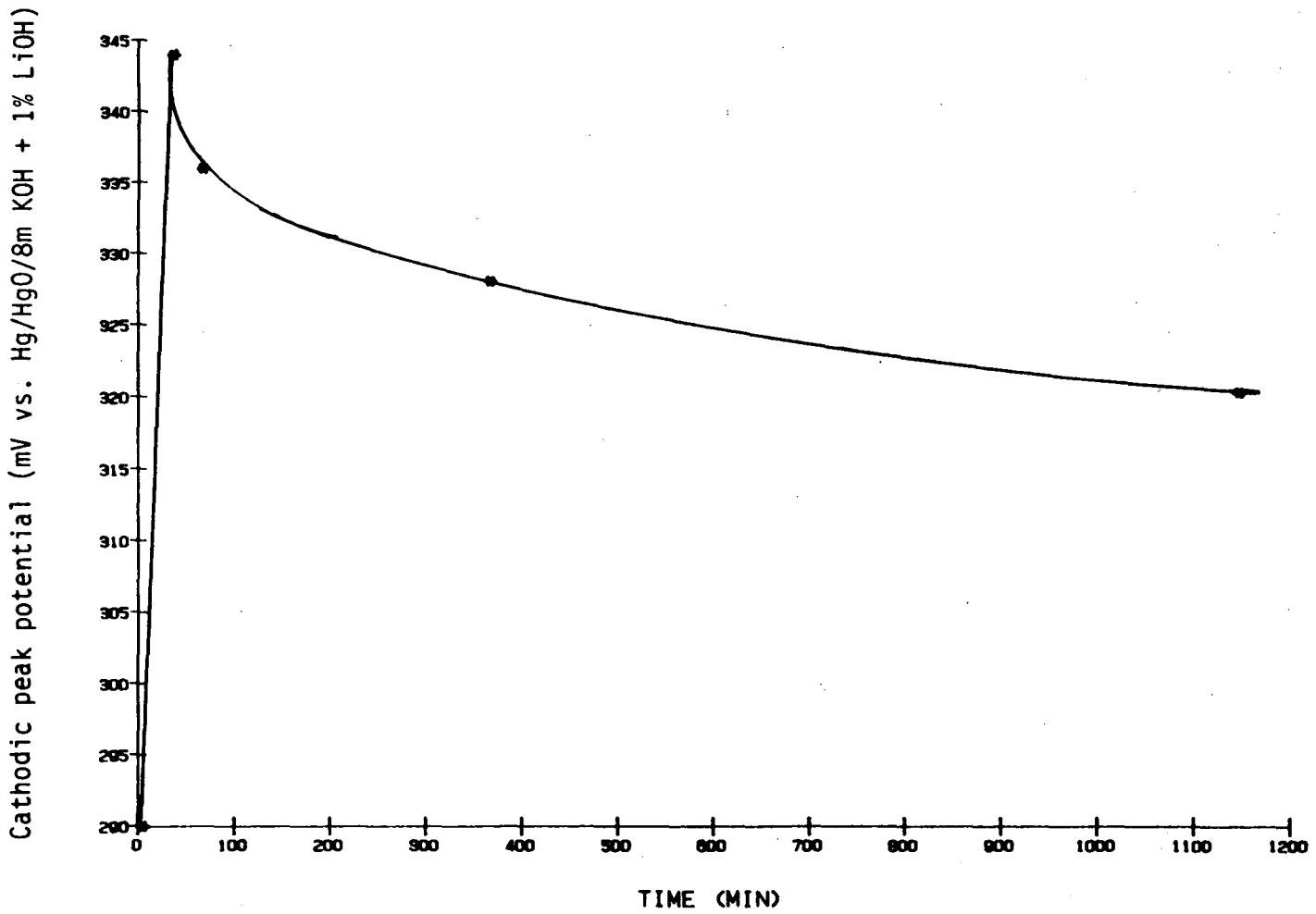

Figure 12. Dependence of cathodic peak potential on cycling time at 100 mV/s and 23°C.

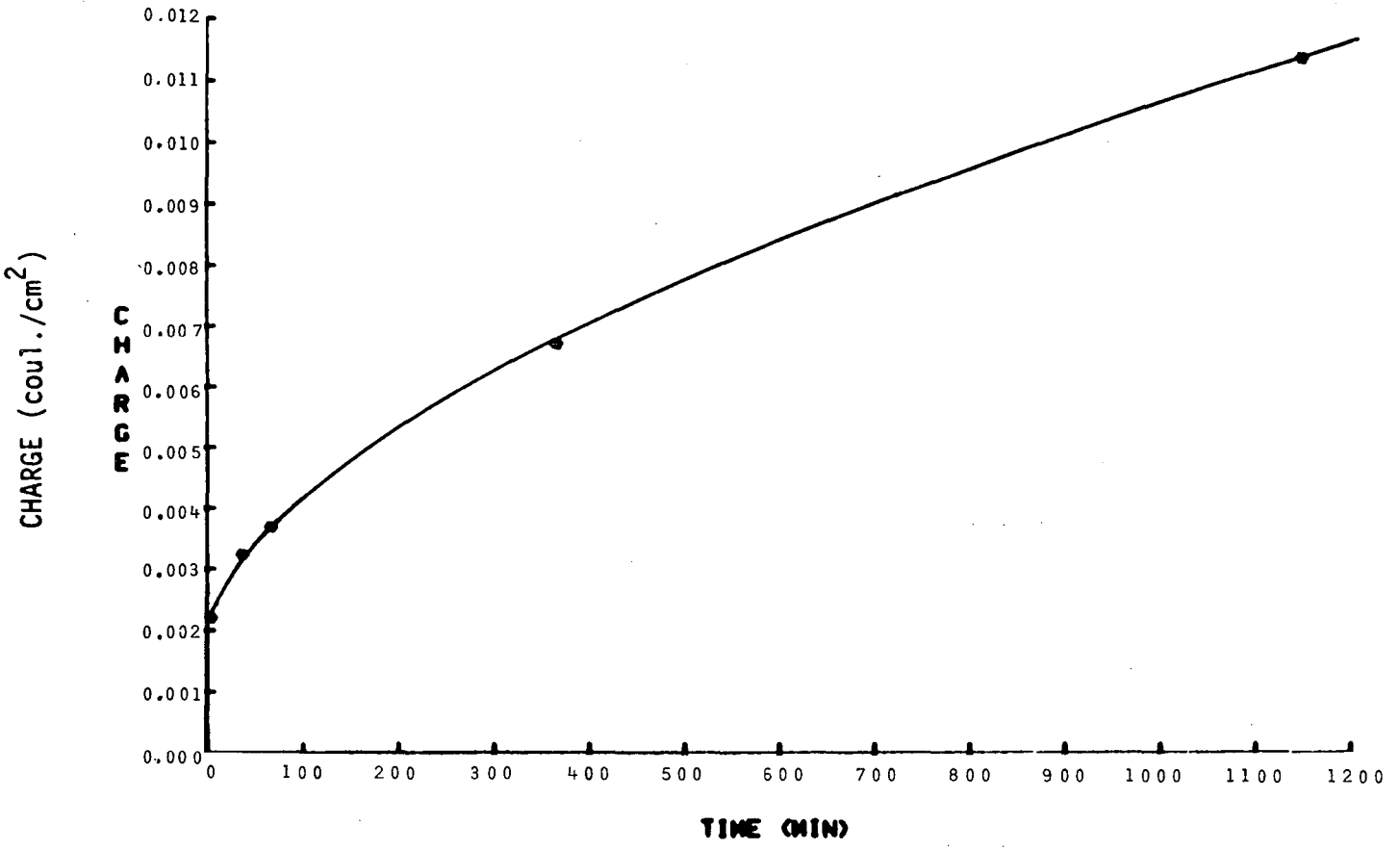

Figure 13. Dependence of anodic charge on cycling time at 100 mV/s and 23°C.

Cathodic peak currents and the associated cathodic charge are difficult to determine and cannot be compared with the anodic behavior discussed above. On anodic sweeps, the oxygen evolution current obscures the current decay from nickel hydroxide oxidation, so that the base line for cathodic currents is not well defined.

If the zero point is taken as the current zero indicated on the ordinate of Figure 9, then cathodic peak currents versus cycle time are obtained as shown for curve 2 in Figure 14. For comparison, curve 1 shows the anodic peak currents from Figure 10. At longer times, the cathodic peak currents are less than the corresponding anodic peak currents, and furthermore it was found that the cathodic charge at any cycle time is much less than the anodic charge. If the cathodic current zero point is taken as the minimum recorded current between the hydroxide oxidation peak and the oxygen evolution line, then cathodic peak currents are shown as curve 3 in Figure 14.

As mentioned earlier, not all of the voltammograms recorded at ambient temperature show just one anodic peak. Under similar cycling conditions, some experiments yielded voltammograms showing two anodic peaks (Figure 15), as reported by many authors using similar techniques and electrolytes[17,18,22,39,42]. It can be seen that although the curves in Figure 15 pertain to different sweep rates, the left peak disappears as the right peak becomes more prominent with cycling. Subtle variations in experimental procedure were possibly responsible for the peak doublet. It should be noted that only one cathodic peak was recorded at all temperatures, and just one anodic peak at non-ambient temperatures.

3.1.2 Non-ambient Temperatures

Non-ambient-temperature voltammograms reveal a number of important features concerning the electrode. Figure 16 shows voltammograms at 0, 45, and 80°C after cycling at 100 mV/s for 10 cycles. Peak currents and anodic charge increase considerably at higher temperatures (Figures 17 and 18), suggesting a greater degree of transformation of $Ni(OH)_2$ to NiOOH and/or the formation of thicker films at higher temperatures in a given number of cycles. This suggests that an increased electrode capacity might be anticipated if batteries were operated at higher temperatures.

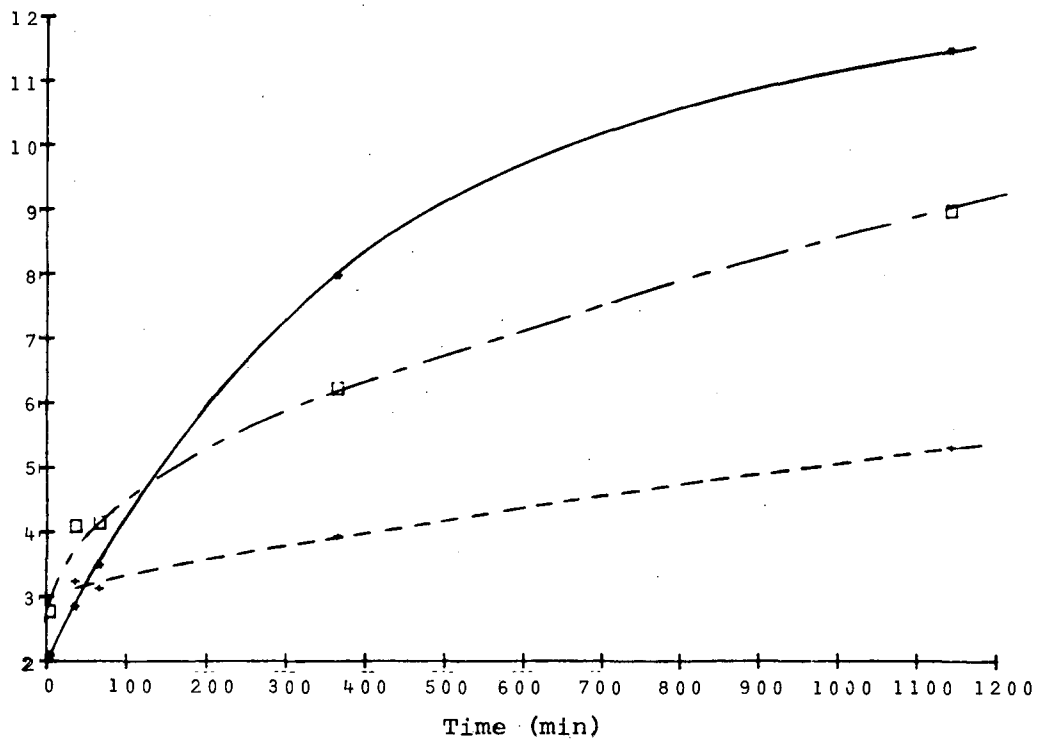

Figure 14. Dependence of peak current on cycling time at 100 mV/s and 23°C.

———— Curve 1. Anodic peak currents from Figure 20.

--------- Curve 2. Cathodic peak currents with current axis zero taken as baseline.

—— - —— Curve 3. Cathodic peak currents with current minimum after anodic peak taken as baseline.

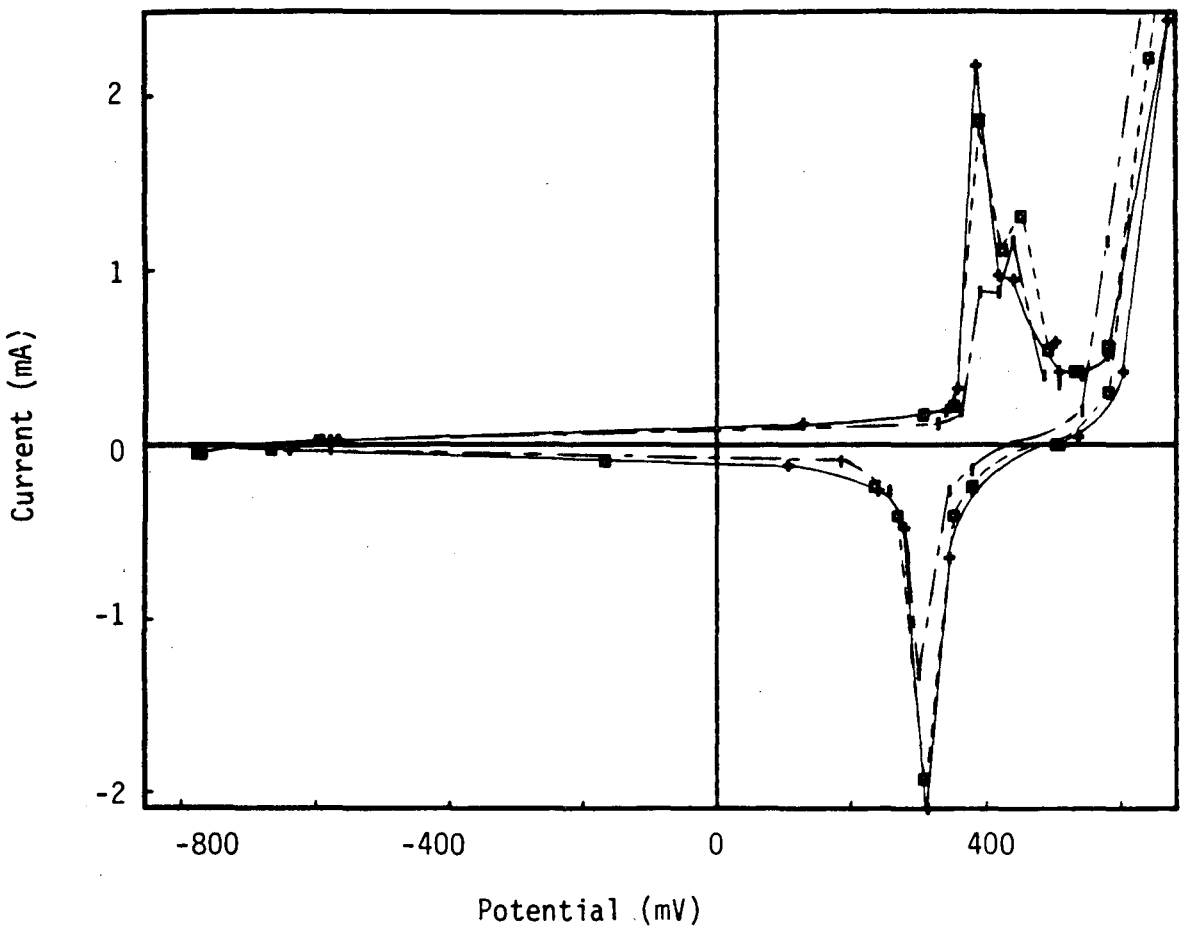

Figure 15. Ambient temperature cyclic voltammograms showing two anodic peaks and single cathodic peaks. Ten cycles were executed at each sweep rate before voltammograms were recorded. (———)100 mV/s, (------) 80 mV/s, (— - —) 40 mV/s).

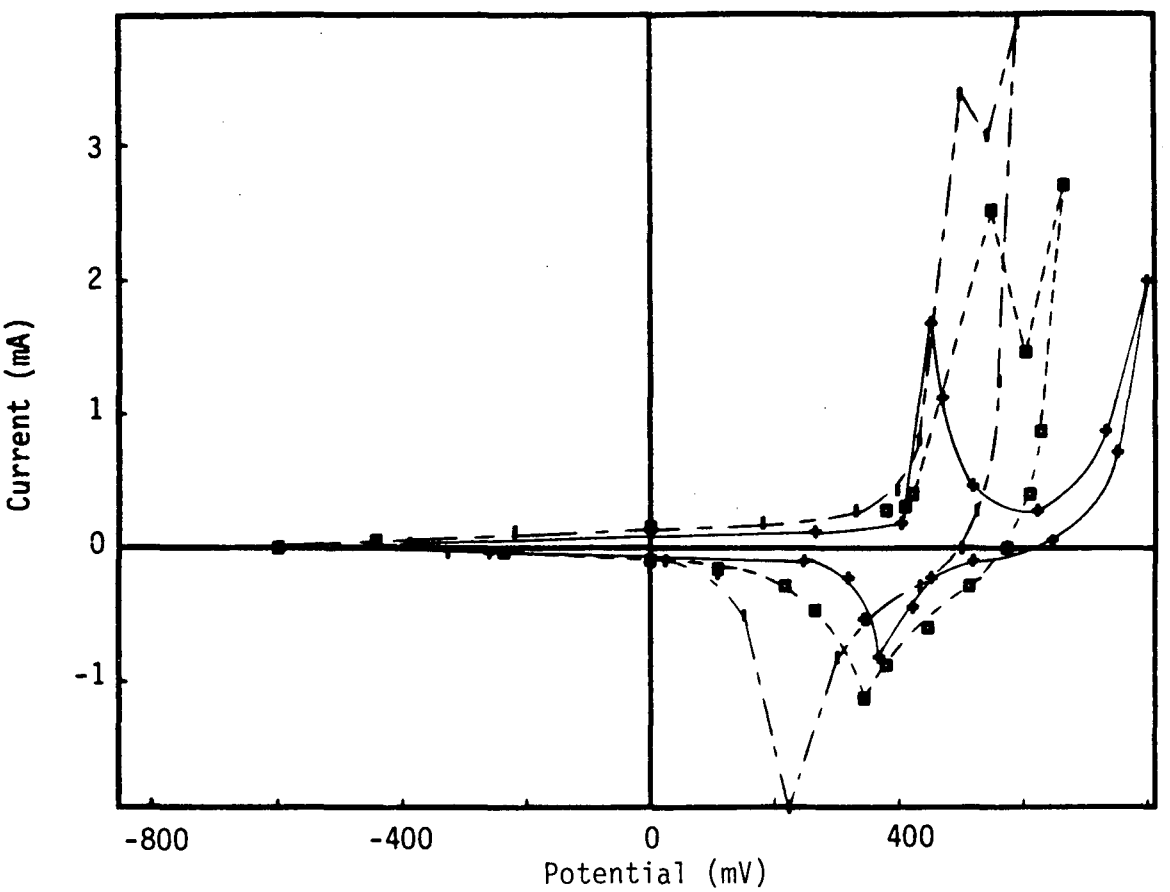

Figure 16. Cyclic voltammograms after 10 cycles at 100 mV/s and 0°C (———), 45°C (------), and 100°C (— - —).

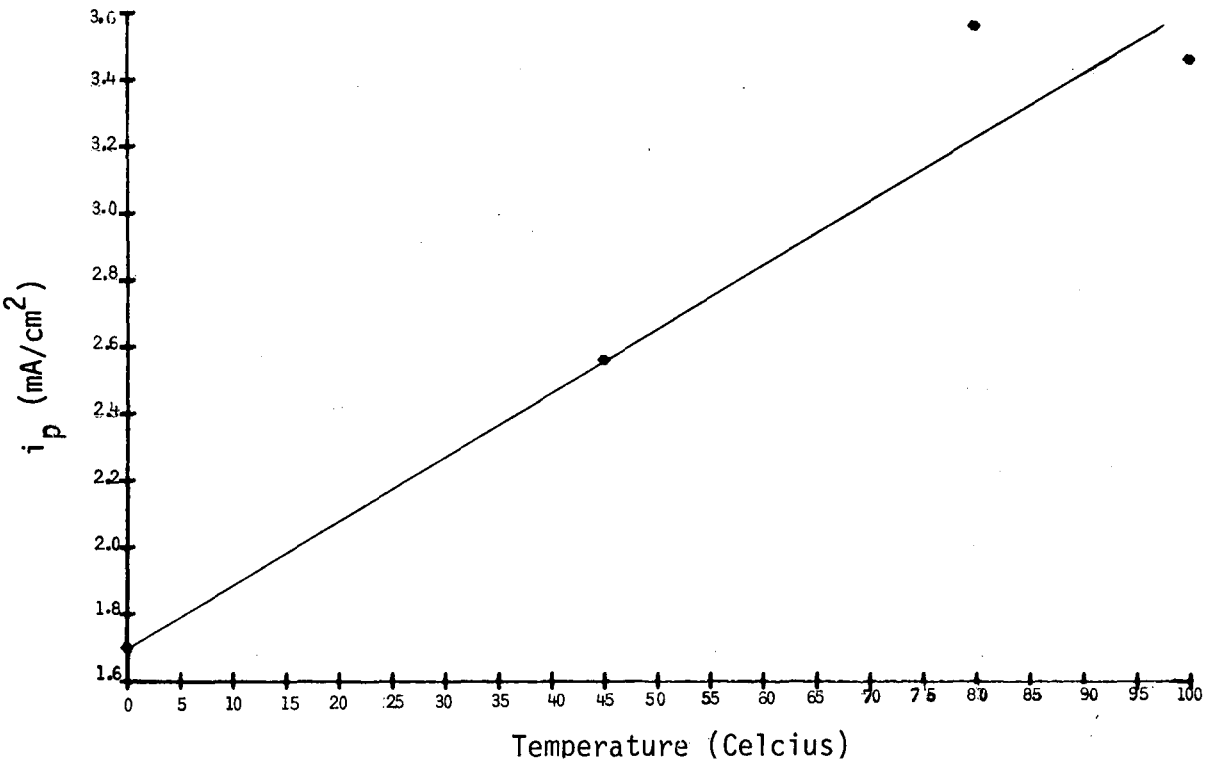

Figure 17. Dependence of anodic peak current on temperature after 10 cycles.

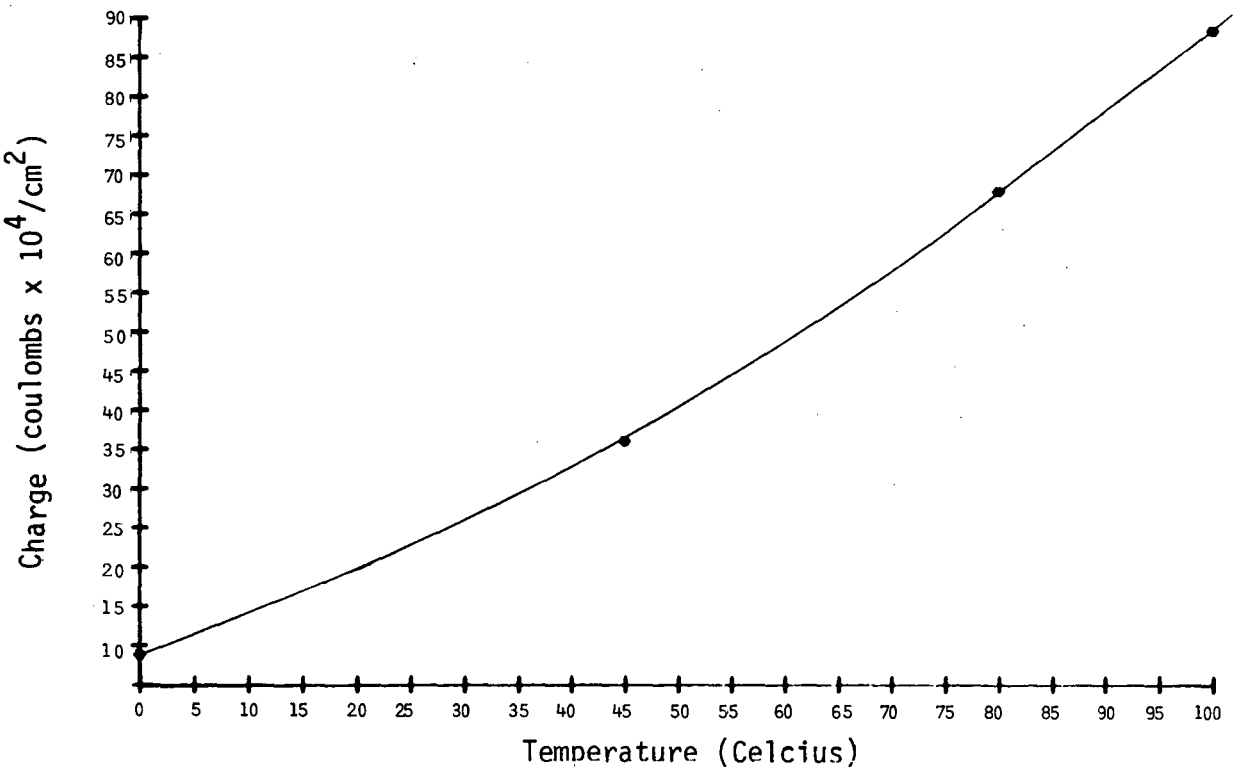

Figure 18. Anodic charge associated with the $Ni(OH)_2$ oxidation peak at various temperatures.

However, the voltammograms in Figure 16 also show that temperature affects the proximity of the oxygen evolution curve to the anodic peak. At 0°C, the oxygen evolution curve is much more noble than the anodic peak. At 45 and 80°C, the oxygen evolution line appears at progressively lower potentials, presumably because of a negative shift in reversible potential. Furthermore, at higher temperatures, the anodic peak shifts closer to the oxygen evolution curve with increasing cycle time (Figure 19). Eventually, the peak cannot be resolved but the cathodic peak is still observed indicating that hydroxide oxidation occurs simultaneously with oxygen evolution. At 100°C, the shift in the anodic peak occurs even more rapidly with increasing cycle number (Figure 20), but at 0°C, virtually no shift in the peak with cycle time is observed (Figure 21).

Above ambient temperature, the combination of the anodic peak shift to more noble potentials and the decreasing reversible potential for oxygen evolution suggests that the charging efficiency of $Ni(OH)_2$ battery electrodes will decrease. Oxygen evolution consumes charge that would otherwise be used for the desired $Ni(OH)_2$ oxidation reaction. A decreased charging efficiency is in fact observed at higher temperatures, as described in Section V.

3.1.3 Sweep Rate Dependence

The voltammograms presented above were all recorded at a sweep rate of 100 mV/s. One cycle at this sweep rate is recorded in about 30 seconds. A battery electrode cycle is typically much longer, and the electrochemical reaction rates of battery electrodes are usually fixed by controlling the charge/discharge current. Despite the difference in experimental control of the electrode kinetics, factors influencing the effect of sweep rate on the voltammograms are still pertinent.

The dependence of peak current on sweep rate for temperatures of 0°, 45° and 60°C is shown in Figure 22. In all cases, the peak current increases with sweep rate but the data, at least for 0° and 45°, do not exhibit a square root relationship characteristic of diffusion-controlled processes. Only two data ponts could be obtained for 60°C, and none at higher temperatures due to the shift in the anodic peak described above. The anodic peak disappeared before a series of voltammograms can be recorded at decreasing sweep rates.

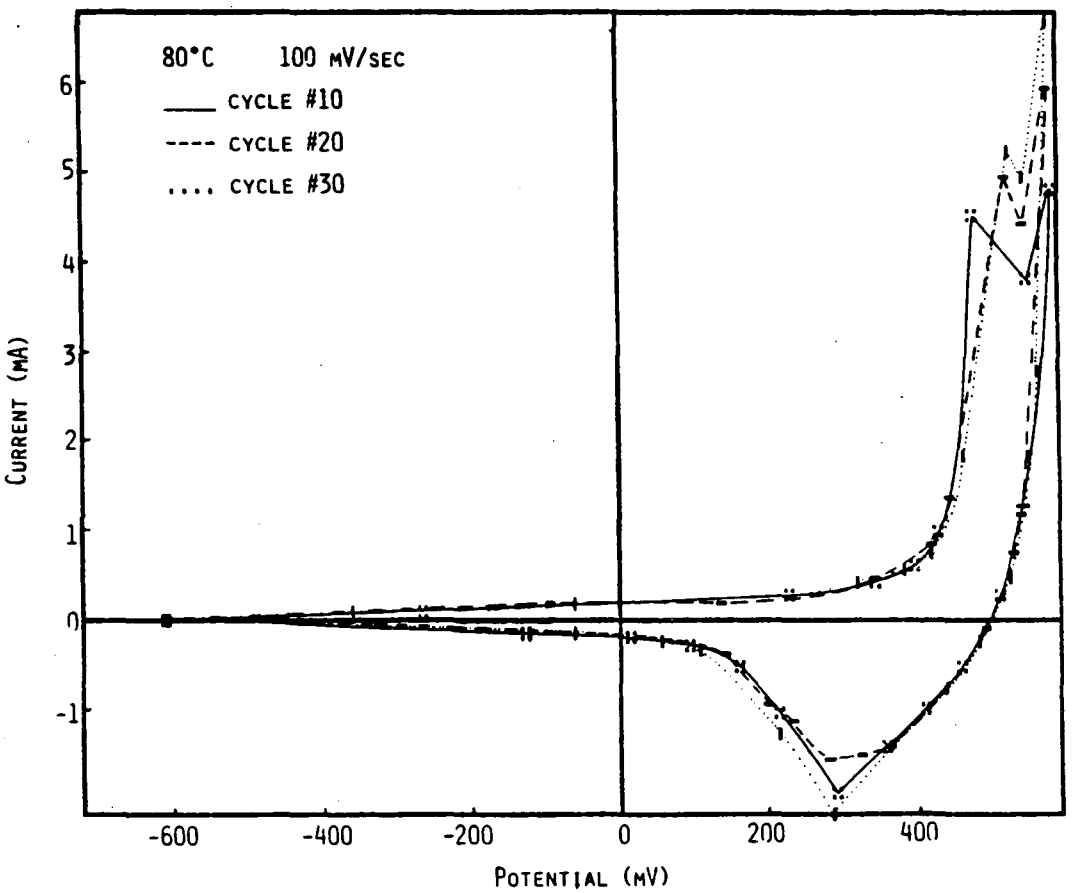

Figure 19. Cyclic voltammograms recorded at 80°C and 100 mV/s after 10 cycles (———), 20 cycles (------) and 30 cycles (.......).

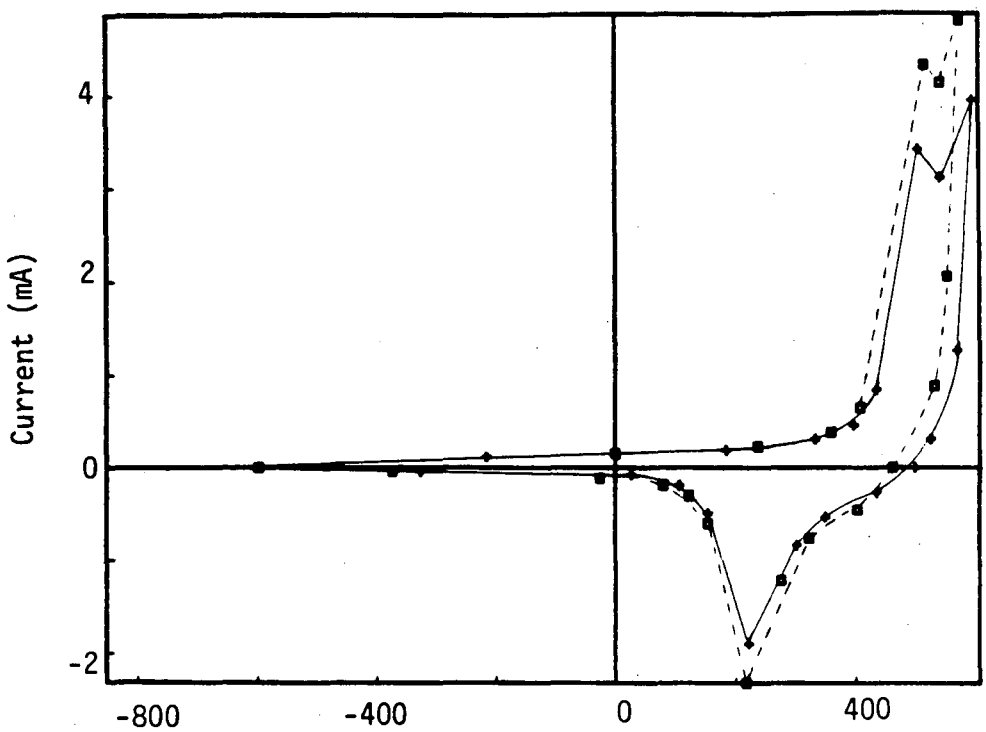

Figure 20. Cyclic voltammograms recorded at 100°C after 10 cycles (———) and 20 cycles (------).

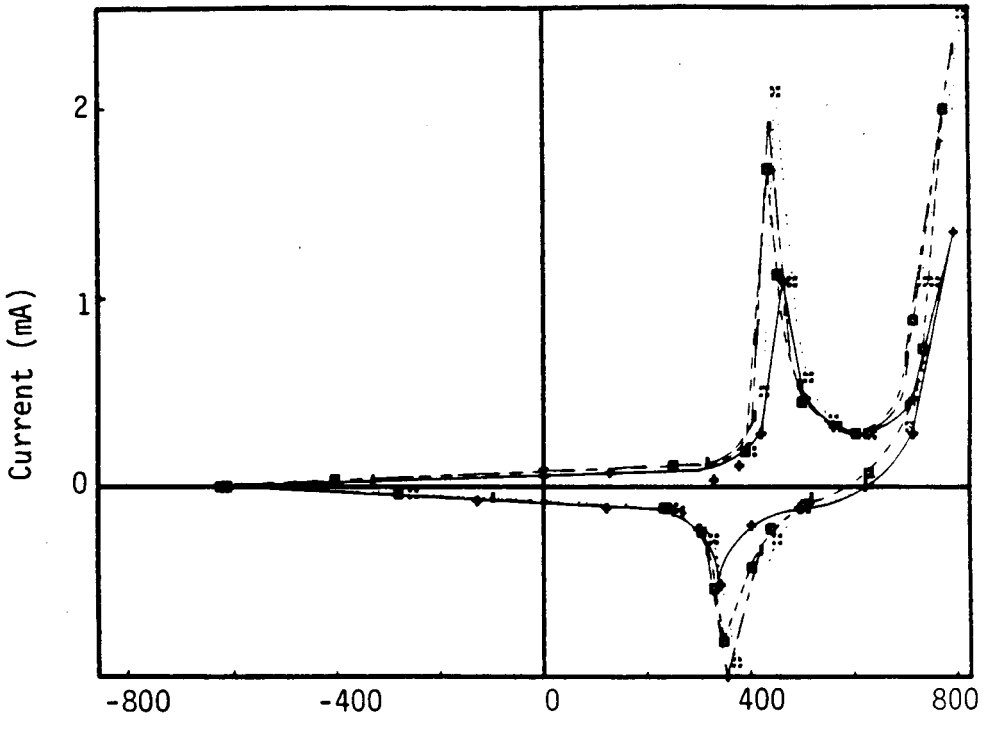

Figure 21. Cyclic voltammograms recorded at 0°C after 3 cycles (———), 10 cycles (------), 15 cycles ( ), and 20 cycles (.....) at 100 mV/s.

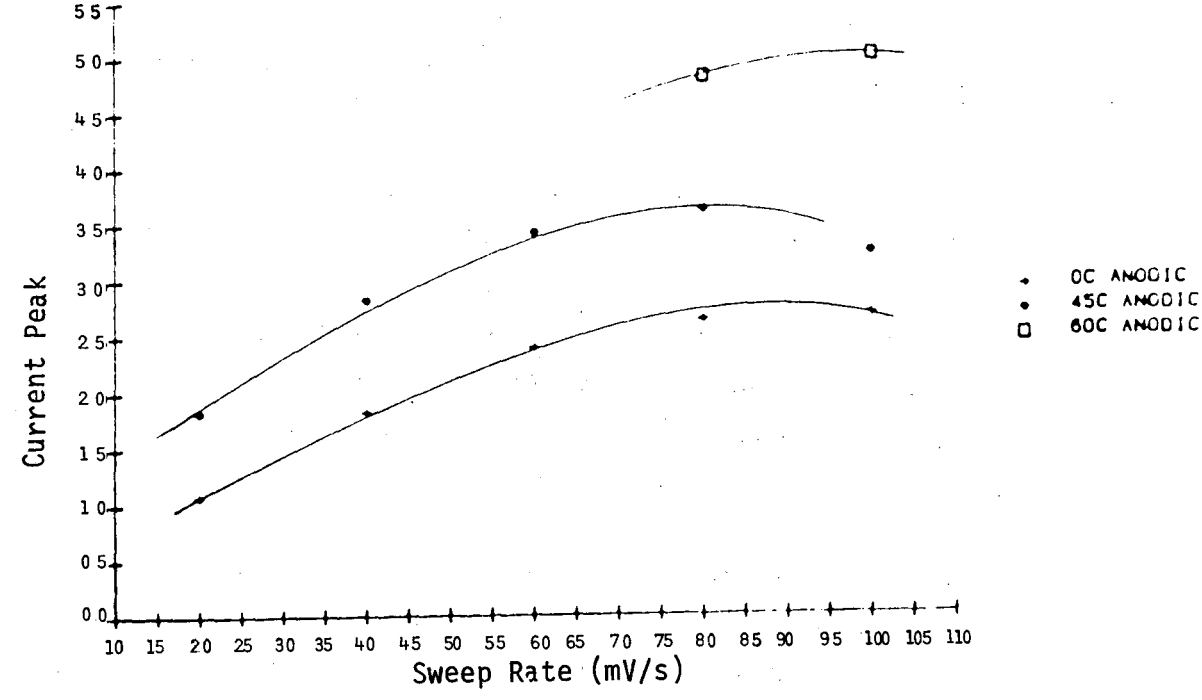

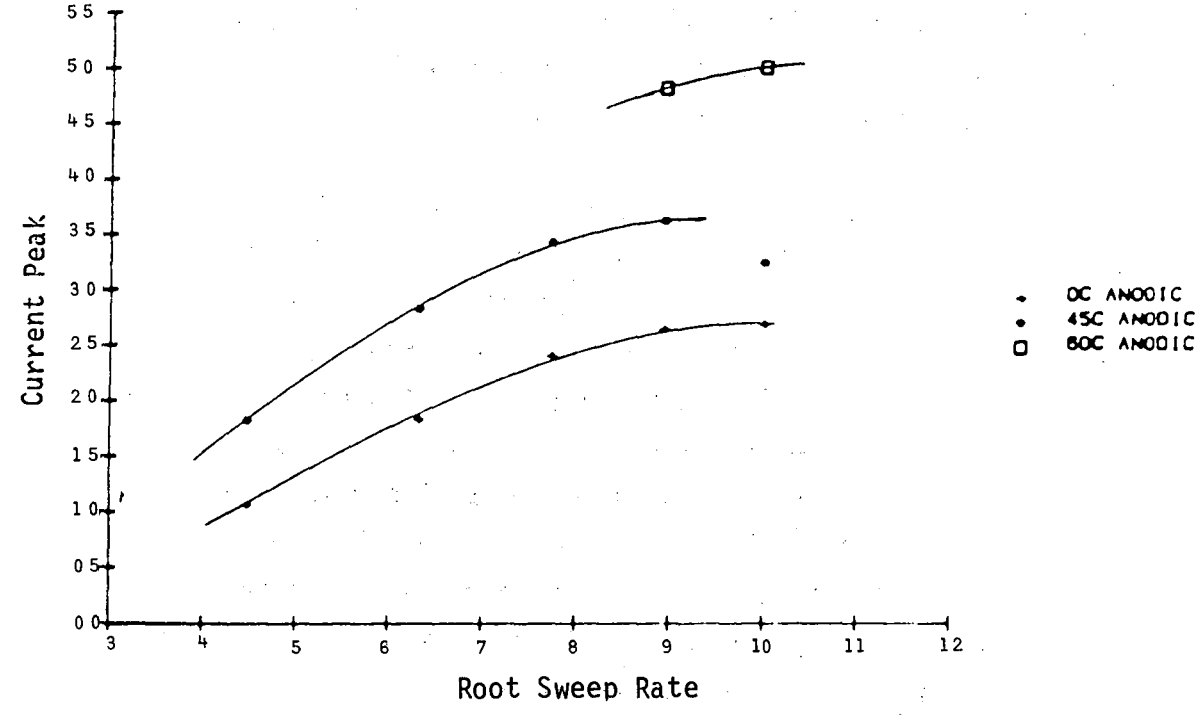

Figure 22. Dependence of anodic peak current on sweep rate and square root sweep rate. (Currents in mA/cm^2 and sweep rate in mV/s).

4.0 PLANAR NICKEL ELECTRODES - AC IMPEDANCE

The transmission line model, described in Section 1.3, requires a knowledge of the interfacial electrolyte/pore wall and electrolyte/backing plate impedances. It is assumed in this work that these impedances can be accurately described by the impedance of a planar electrode in the same electrolyte. With this assumption, the transmission line can be viewed as a model for predicting the impedance of a porous electrode based on the knowledge of the impedance for a planar electrode.

The above assumption can be justified by several arguments. Firstly, neglecting pore wall curvature, the basic structure of the sintered battery electrode at the electrolyte/pore wall interface, consisting of the metal, film, and electrolyte, should be identical to that for a planar electrode. The structure of the rolled and bonded electrodes deviates somewhat from this geometry as described in Section 2.2, but is similar if the graphite is regarded as a substitute for the metal phase. Secondly, the use of a concentrated electrolyte in this study should avoid electrolyte depletion within the pores of a porous electrode. The electrolyte concentration at the pore wall is expected to be approximately the same as that at the film/electrolyte interface for a planar electrode.

In this study, impedance data for a planar electro-oxidized (thin) film electrode are used to provide the interfacial impedance in the transmission line model. It can be argued that the impedance data for a planar thick film electrode should be used since the active material in nickel battery electrodes is typically chemically or electrochemically deposited to a relatively large thickness. However, it is essential that the impedance data for the planar electrode pertain to a non-porous film. Porosity can develop during film deposition when using chemical and electrochemical film deposition techniques. Electro-oxidized films are assumed to have comparatively smooth surfaces, and porosity effects on the impedance data for thin film electrodes are therefore considered to be negligible.

Impedance data for electro-oxidized nickel electrodes are presented in this section. The data are analyzed in terms of equivalent circuit models,

and the circuit components related to electrode processes occurring within the hydroxide films.

4.1 Impedance as a Function of DC Bias Potential at Ambient Temperature

In general, the impedance data are presented in the form of Bode plots which show the dependence of the magnitude of the impedance, /Z/, and the phase angle, ϕ, on the angular frequency, ω. These parameters are given by

$$/Z/ = (ZR^2 + ZI^2)^{1/2} \tag{21}$$

$$\phi = \mathrm{Tan}^{-1} \frac{ZI}{ZR} \tag{22}$$

$$\omega = 2\pi f \tag{23}$$

where ZR and ZI are the real and imaginary components of the impedance, respectively, and f is the frequency in Hz of the ac signal.

Impedance data were measured sequentially at applied dc potentials over the range -0.5 V to 0.6 V. Figures 23 and 24 show a typical sequence of Bode plots at ambient temperature. The dc potential sequence for these data involved 0.1 V increments with one hour at each potential prior to the impedance measurement.

The impedance magnitude is shown to decrease with increasing potential, and a large decrease is observed when the oxy-hydroxide phase is formed at 0.5 V. Phase angles generally show two maxima within the frequency range studied (typically 10 kHz to 6 mHz). The high frequency maximum shifts sharply to lower frequencies when the oxy-hydroxide phase is formed at the higher potentials. However, both /Z/ and ϕ exhibit similar features above and below the hydroxide/oxy-hydroxide transition.

It was shown that variation of the polarization sequence has little effect on the impedance data for a given potential in the range from 0 to 0.5 V.

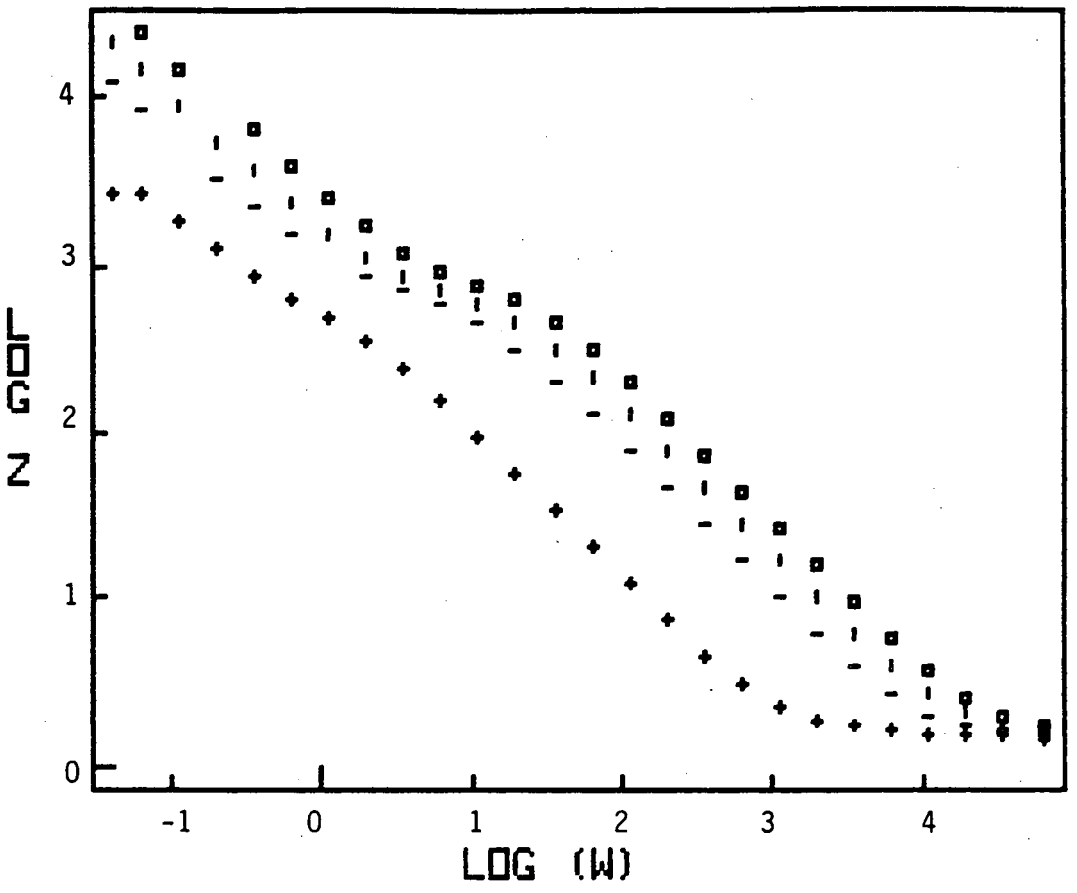

Figure 23. Bode plot of |Z| data obtained at ambient temperature for a sequence of applied dc potentials showing in order 0 V (top curve), 0.2, 0.4 and 0.5 V (bottom curve)

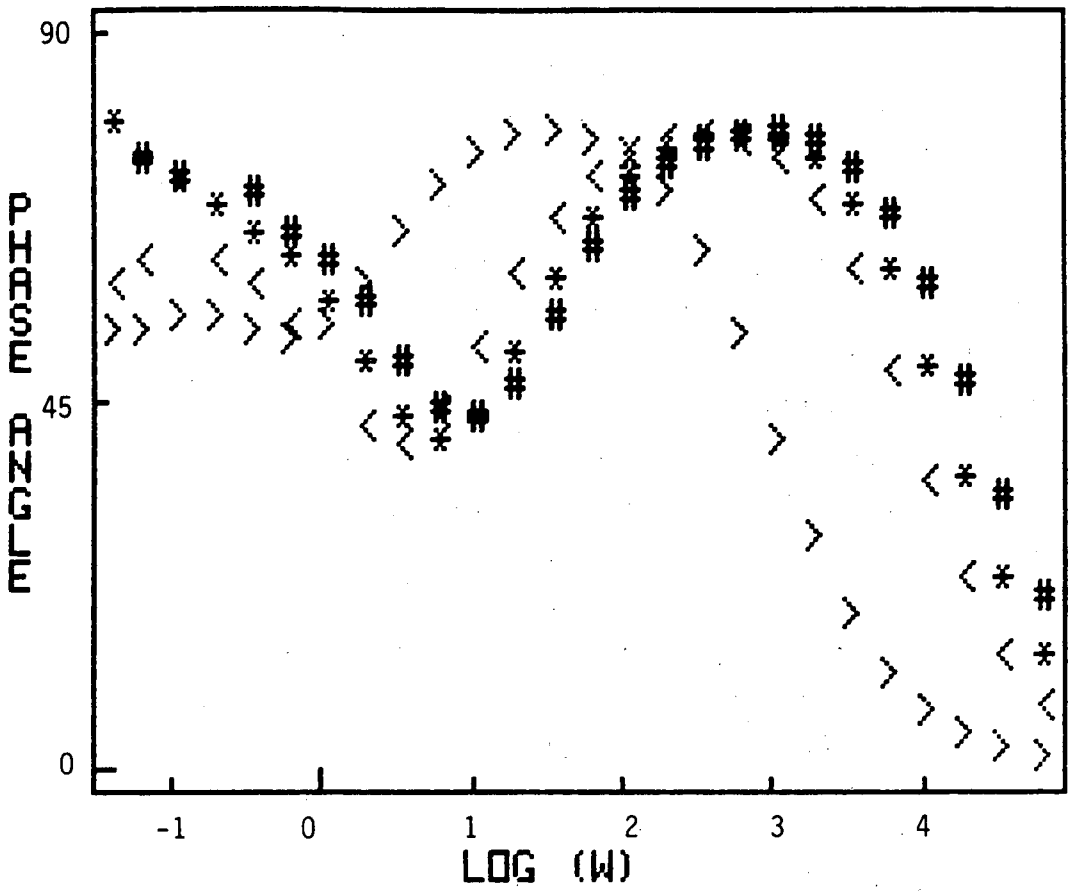

Figure 24. Bode plot of phase angle data corresponding to Figure 23. #=0 V, *=0.2 V, <=0.4 V and >=0.5 V.

However, significant differences between data recorded at the same potential were observed in one instance. Specifically, when an electrode was polarized directly to 0.5 V after immersion in the electrolyte, the impedance magnitude was increased from that for an electrode previously polarized at lower potentials. This effect was not caused by a difference in the immersion time since only minor changes in the electrode impedance occurred with time. The above shift more likely indicates that the degree of the $Ni(OH)_2$/NiOOH conversion is different for the two polarization sequences. In this case, or for other reasons, the previously polarized NiOOH films are likely to be structurally, and electrochemically, different from films formed directly at high potentials.

None of the above polarization procedures included a decreasing sequence of dc potentials. An ellipsometric study of the film thickness as a function of time and potential has shown that thicker films are formed at higher potentials. The film thickness would not be expected to decrease upon lowering the potential since dissolution of the films is neglible and also, the combined thermodynamic stability of the $Ni(OH)_2$ and NiOOH films covers the entire potential range.

Several impedance spectra were recorded outside the -0.15 to 0.5 V potential range. An important change in the impedance data was observed at -0.5 V (Figure 25). The polarization resistance ($ZR_{W=0} - ZR_{W-\infty}$) at this potential is found to be relatively small, and the phase angle dropped to almost zero at low frequencies. At higher potentials, the phase angle remained above 45 degrees, although it generally exhibited a decrease in the low frequency region. In one experiment at 0.5 V, a minimum frequency of 0.56 mHz was employed, yet the phase angle still remained at about 30 degrees.

At -0.5 V, the hydroxide film should behave like an insulator according to Glarum and Marshall[21]. However a lack of electronic conductivity in the film must be more than offset by an increase in ionic conductivity to explain the small polarization resistance. This is consistent with previous ellipsometric work[9] which showed an increase in film thickness at very low potentials.

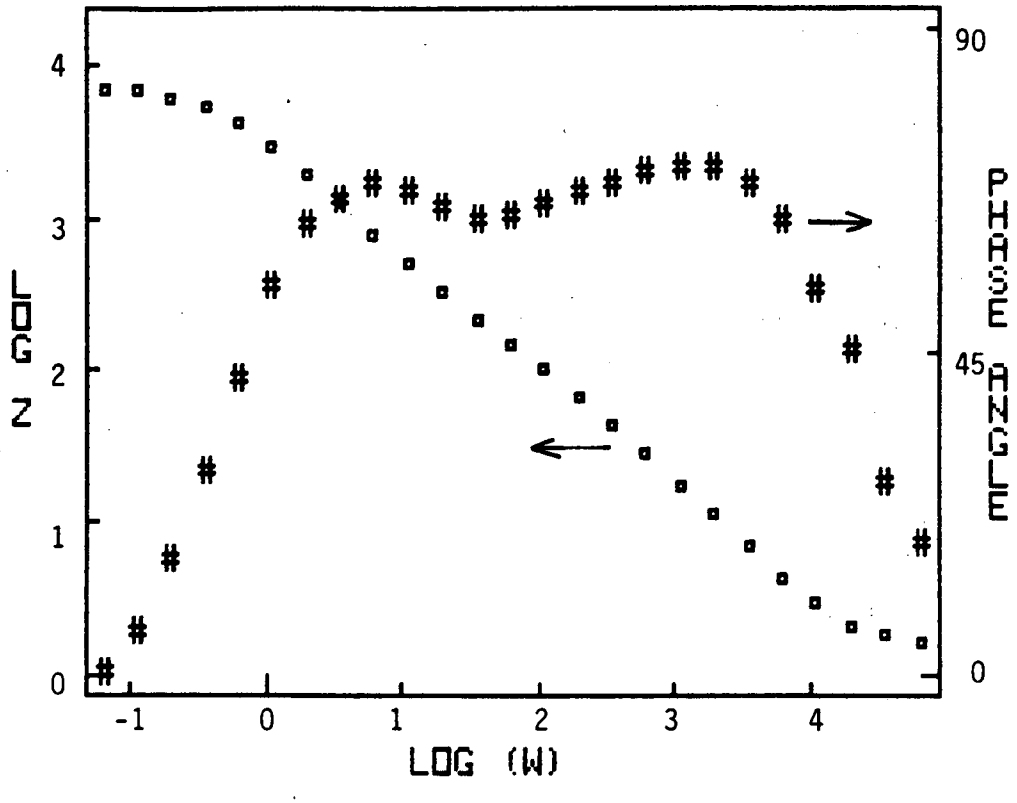

Figure 25. Bode plot of impedance data at -0.5 V and ambient temperature.

At 0.6 V, the impedance spectrum changed drastically from that at 0.5 V. The impedance magnitudes were much smaller, and the phase angles showed only a single maximum (Figures 26 and 27). The impedance data at 0.6 V can be explained by an activation-controlled step in the oxygen evolution reaction. The oxy-hydroxide film is an n-type semiconductor with a sufficiently high conductivity at 0.6V to support oxygen evolution at the film/electrolyte interface. The reaction proceeds easily as indicated by the low values of the impedance magnitude. At 0.5 V, the film is still n-type, but either the conductivity or the overvoltage is not sufficient to allow the oxygen evolution reaction to proceed at a significant rate.

4.2 Equivalent Circuits

The planar electrode impedance data presented in Section 4.1 can be adequately modelled by more than one equivalent circuit. Several circuits have been analyzed in detail, and they are discussed in this section. The circuit components are plotted against potential and temparature, and are examined in terms of their electrochemical significance.

4.2.1 Impedance data at Ambient Temperature

A number of simplified equivalent circuits can be derived from the complex circuit (Figure 4) developed earlier. Most of them were found to be unsuitable but the series and parallel circuits given in Figures 28 and 29, respectively, were shown to provide appropriate models of the electrode impedance. The parallel network is a modified form of the series equivalent circuit which itself is obtained directly from the generalized circuit in Figure 4 by incorporating several refinements. Firstly, the impedance of the metal/film interface and also the adsorption impedance are both assumed to be negligible. Of course, these assumptions do not imply that either charge transfer at the metal/film interface or adsorption processes are absent, but rather that these processes exert little influence on the electrode kinetics. Secondly, it is assumed that the impedance of the film can be represented by just one parallel combination without specifying at this stage whether it involves components related to the "bulk" film or the space charge region.

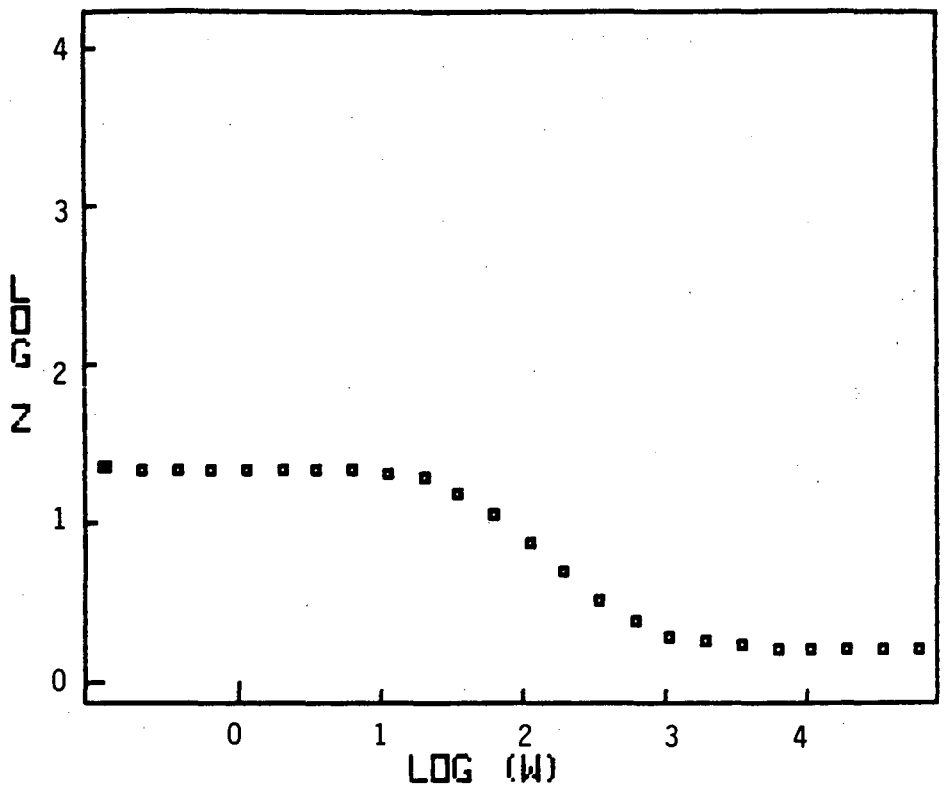

Figure 26. Bode plot of |Z| data at 0.6 V and ambient temperature.

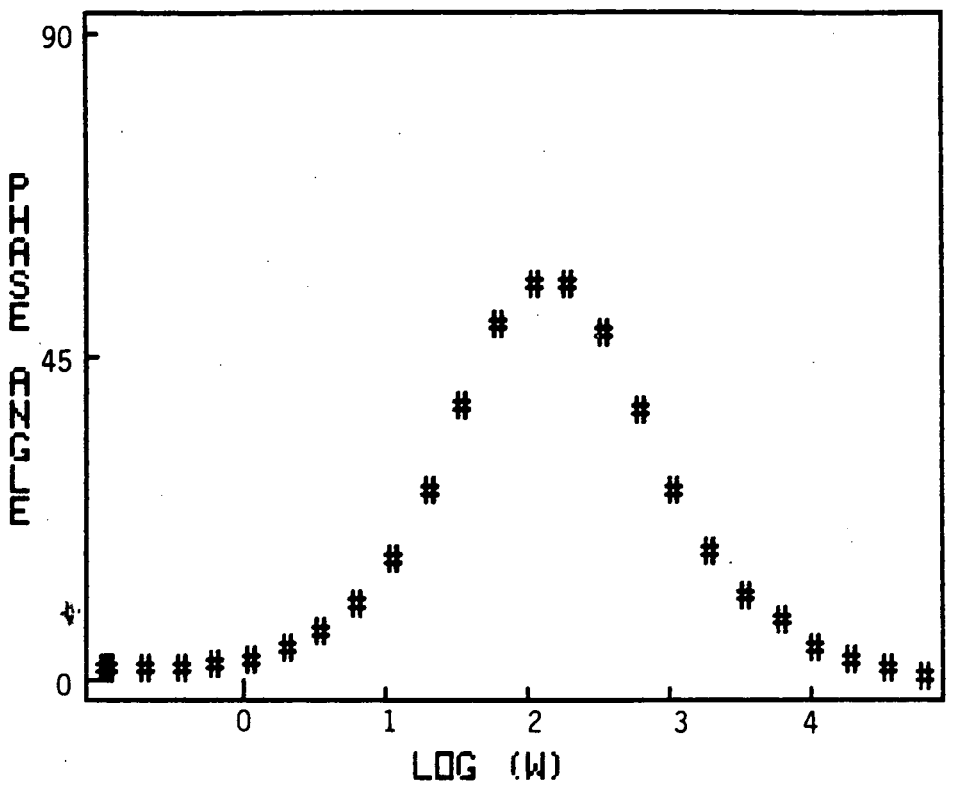

Figure 27. Bode plot of phase angle data corresponding to Figure 26.

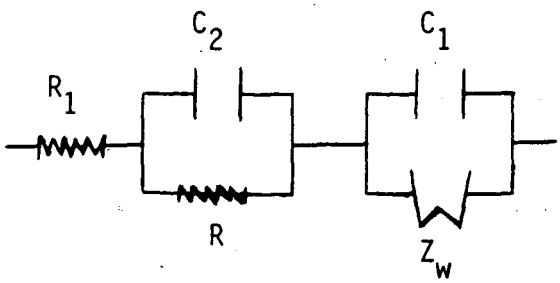

Figure 28. Series equivalent circuit to represent the impedance of a planar nickel electrode in 8 m KOH + 1% LiOH.

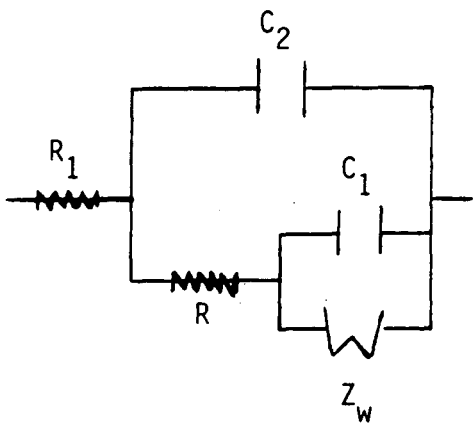

Figure 29. Parallel equivalent circuit to represent the impedance of a planar nickel electrode in 8 m KOH + 1% LiOH.

Although the Bode plots of experimental data do not indicate the presence of a Warburg impedance, the growth of multilayer films generally involves diffusion control to some extent. Moreover, the impedance results obtained by Madou and McKubre[36], and Zimmerman et al.[63] for thick films on nickel clearly show that a Warburg impedance associated with the film dominates the low frequency region of the impedance spectrum over a wide potential range. While electro-oxidized films, as formed in the present study, are not considered to be thick, a Warburg impedance should still be present in such cases, but it would appear to have a less conspicuous effect on the impedance data. Accordingly, a Warburg impedance is included in each equivalent circuit but the parallel resistance, R_3 or R_3' in Figure 4, is assumed to be large compared with the Warburg impedance, and can therefore be neglected.

The impedance expressions derived for these circuits are as follows:
For Figure 28,

$$Z_{Total} = R_1 + \frac{A}{A^2+B^2} + \frac{D}{D^2+E^2} - j\ \frac{B}{A^2+B^2} + \frac{E}{D^2+E^2} \qquad (24)$$

where $A = \frac{\omega^{1/2}}{2}$, $B = C_1 + \frac{\omega^{1/2}}{2}$, $D = \frac{1}{R}$, $E = C_2$

For Figure 29,

$$Z_{Total} = R_1 + \frac{D - j\,[G(B^2+D^2) - B]}{[1 - 2GB + G^2(B^2+D^2)]} \qquad (25)$$

where $G = \omega C_1$, $A = \frac{EE}{EE^2+FF^2}$, $B = \frac{-FF}{EE^2+FF^2}$, $D = A+B$, $EE = \frac{\omega^{1/2}}{2}$, $FF = C_1 + EE$

In both cases, a semi-infinite diffusion layer is assumed for the Warburg diffusion impedance, and equation 2 is used in the derivation of the above

equations. A circuit modelling process was performed with software developed for Apple II-Plus microcomputers (Appendix 1).

Experimental impedance spectra were compared with theoretical spectra calculated using Equations 24 and 25 and it was shown that the impedance expressions for both of the equivalent circuits could reproduce the experimental data over the whole frequency range. Furthermore, these circuits appear to be applicable above and below the $Ni(OH)_2/NiOOH$ transition potential.

The components in the two circuits were optimized with a second software package (Appendix 2) developed to minimize the sum of the square differences between the experimental and theoretical impedance data. Examples of fitted data at 0 and 0.5 V are shown in Figures 30 to 33. Clearly, the essential features of the experimental data are reproduced by the model.

The sum of the squares error between the theoretical and experimental data over the -0.15 to 0.5 V range was similar for the two equivalent circuits. Consequently, no conclusions about the merits of one circuit over the other can be drawn from the curve fitting procedure.

The optimized values of the circuit components proved to be useful in the selection of the best equivalent circuit. Values of the components for the two equivalent circuits are plotted as a function of potential in Figure 34 to 38. The resistance, R, and Warburg coefficient, σ, for the circuits decrease with increasing potenial. Both capacitances in each circuit increase with potential, particularly above the hydroxide/oxy-hydroxide transition potential. Larger capacitances, smaller resistances, and smaller Warburg coefficients all correspond to smaller impedances, consistent with the smaller impedance magnitudes observed experimentally at more noble potentials (Figures 23 and 24).

The smaller capacitance, labelled C_2 in Figures 28 and 29, together with the resistance R exhibit the higher frequency relaxation shown in the Bode plots (Figures 23 and 24). Mott-Schottky plots of $1/C_2^2$ versus E (Figure 39) show a straight line at the lower potentials for data derived from the circuit

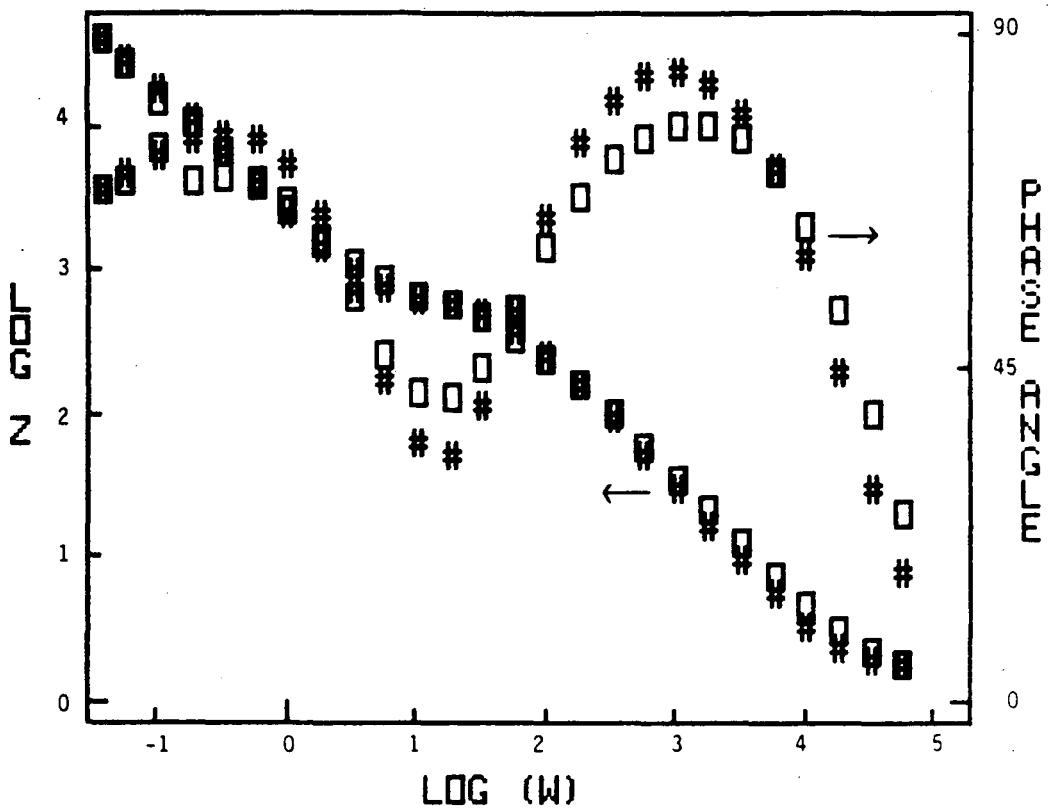

Figure 30. Bode plots of experimental (#) and calculated (□) impedance data at 0 V and 23°C. The calculated data were obtained using the equivalent circuit in Figure 28.

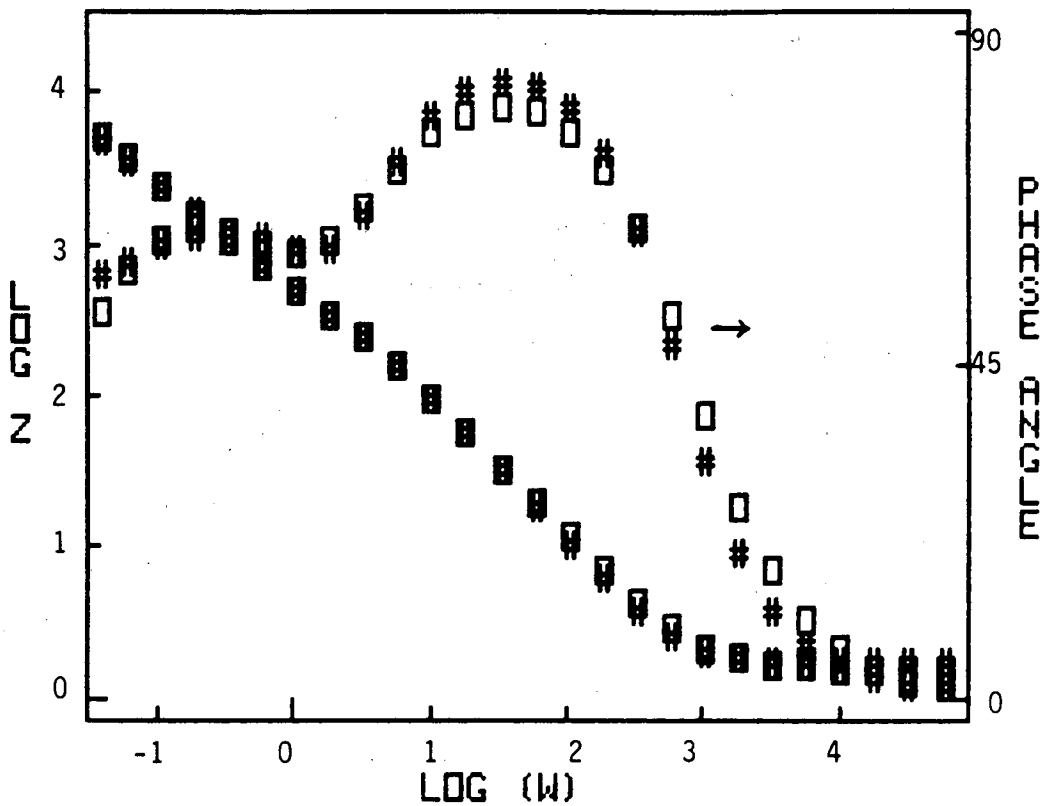

Figure 31. Bode plots of experimental (#) and calculated (□) impedance data for 0.5 V and 23°C. The calculated data were based on the equivalent circuit in Figure 28.

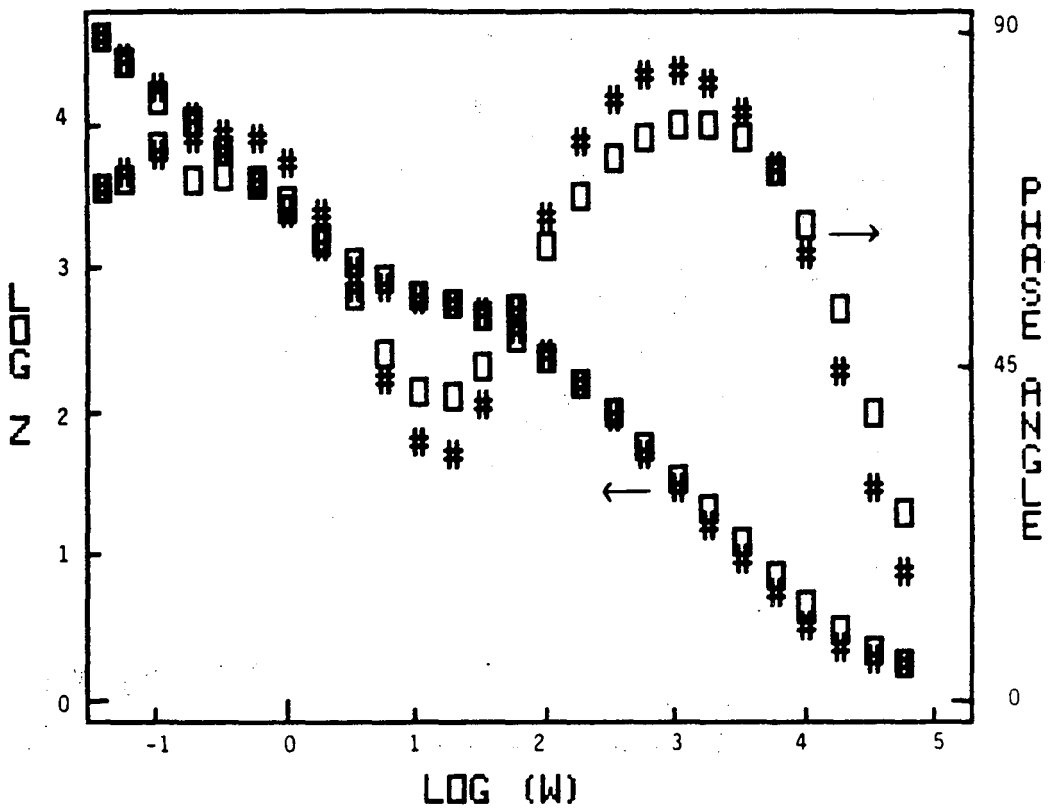

Figure 32. Bode plots of experimental (#) and calculated (□) impedance data at 0 V and 23°C. The calculated data were based on the equivalent circuit in Figure 29.

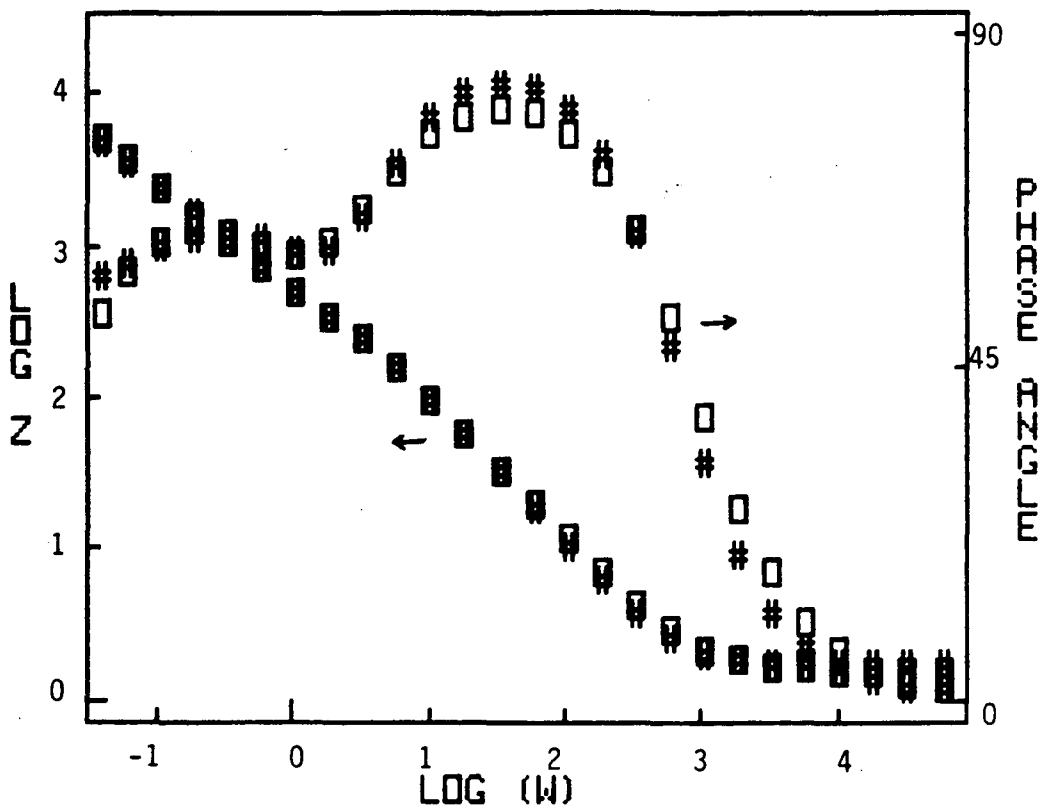

Figure 33. Bode plots of experimental (#) and calculated (□) impedance data at 0.5 V and 23°C. The calculated data were based on the equivalent circuit in Figure 29.

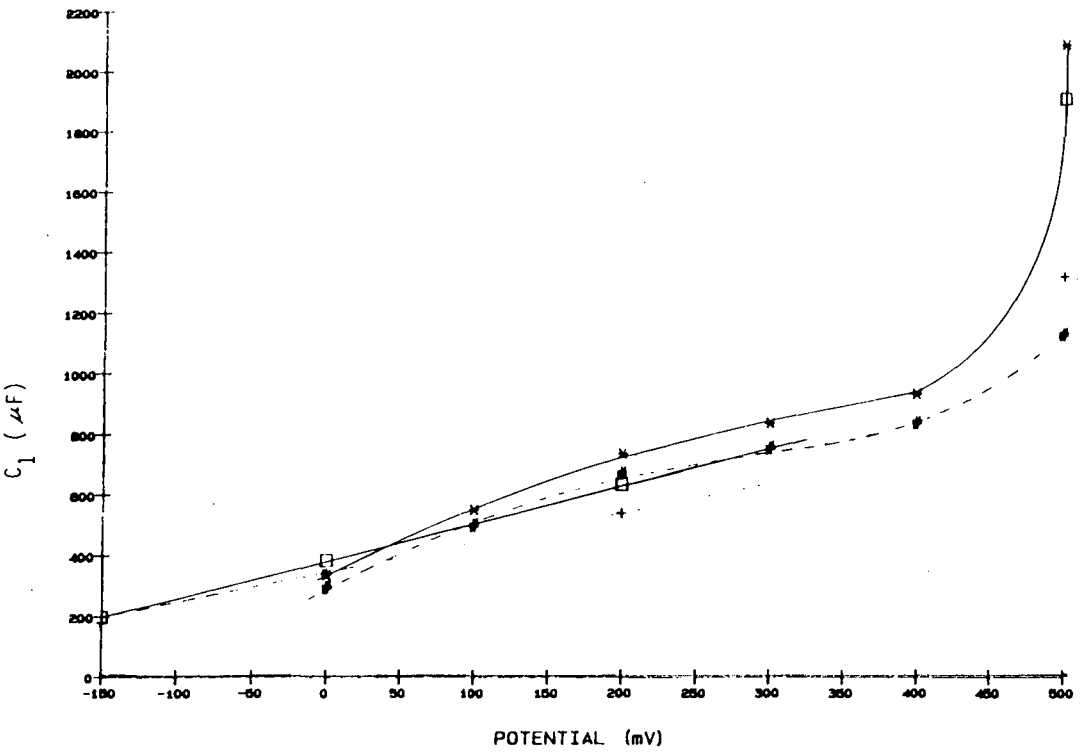

Figure 34. Dependence of the capacitance, C_1 on potential for two applied dc bias sequences. Values of C_1 were derived for the equivalent circuits in Figures 28 (——) and 29 (----).

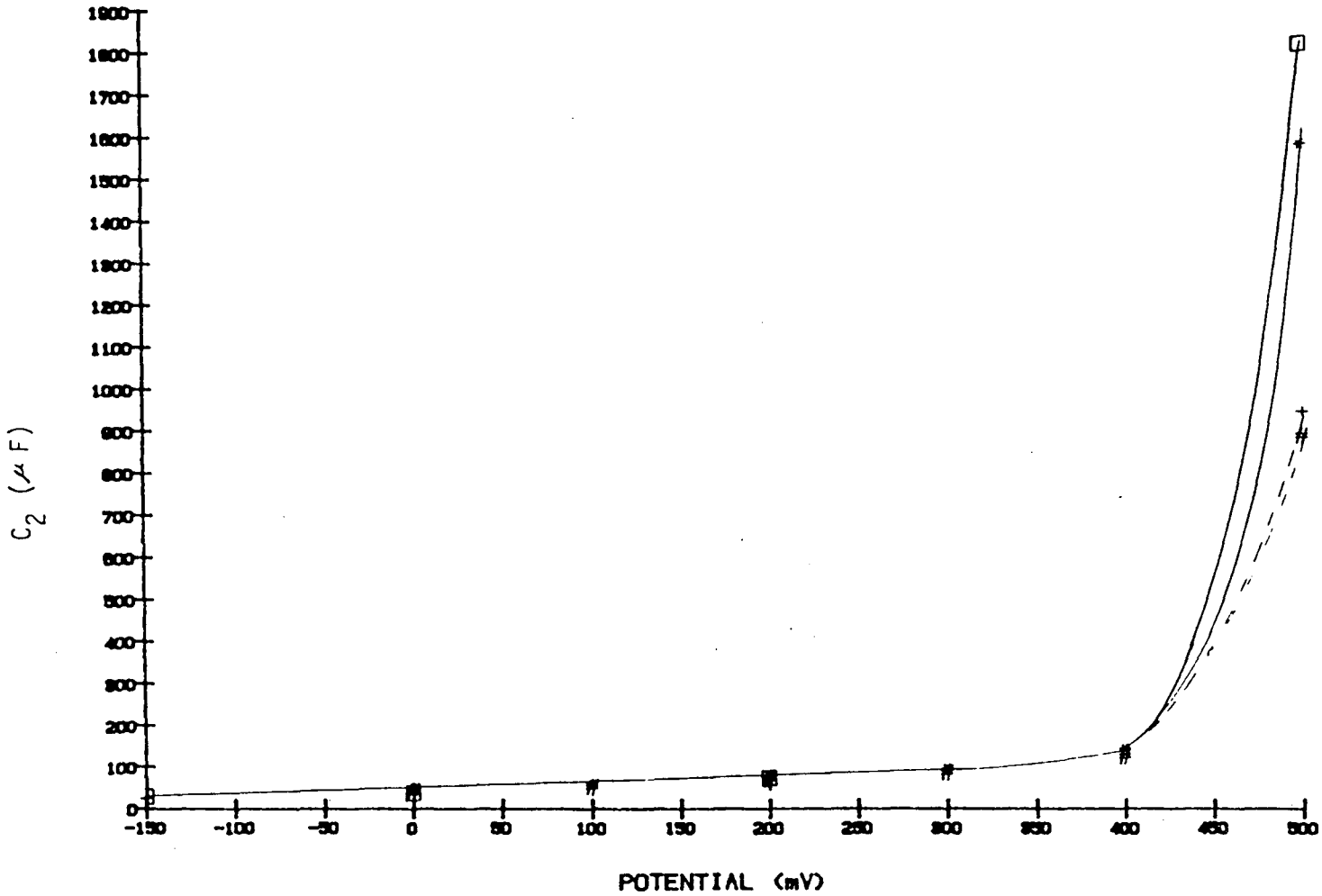

Figure 35. Dependence of the capacitance C_2 on potential for two applied dc bias sequences. Curves for C_2 as specified in Figure 34.

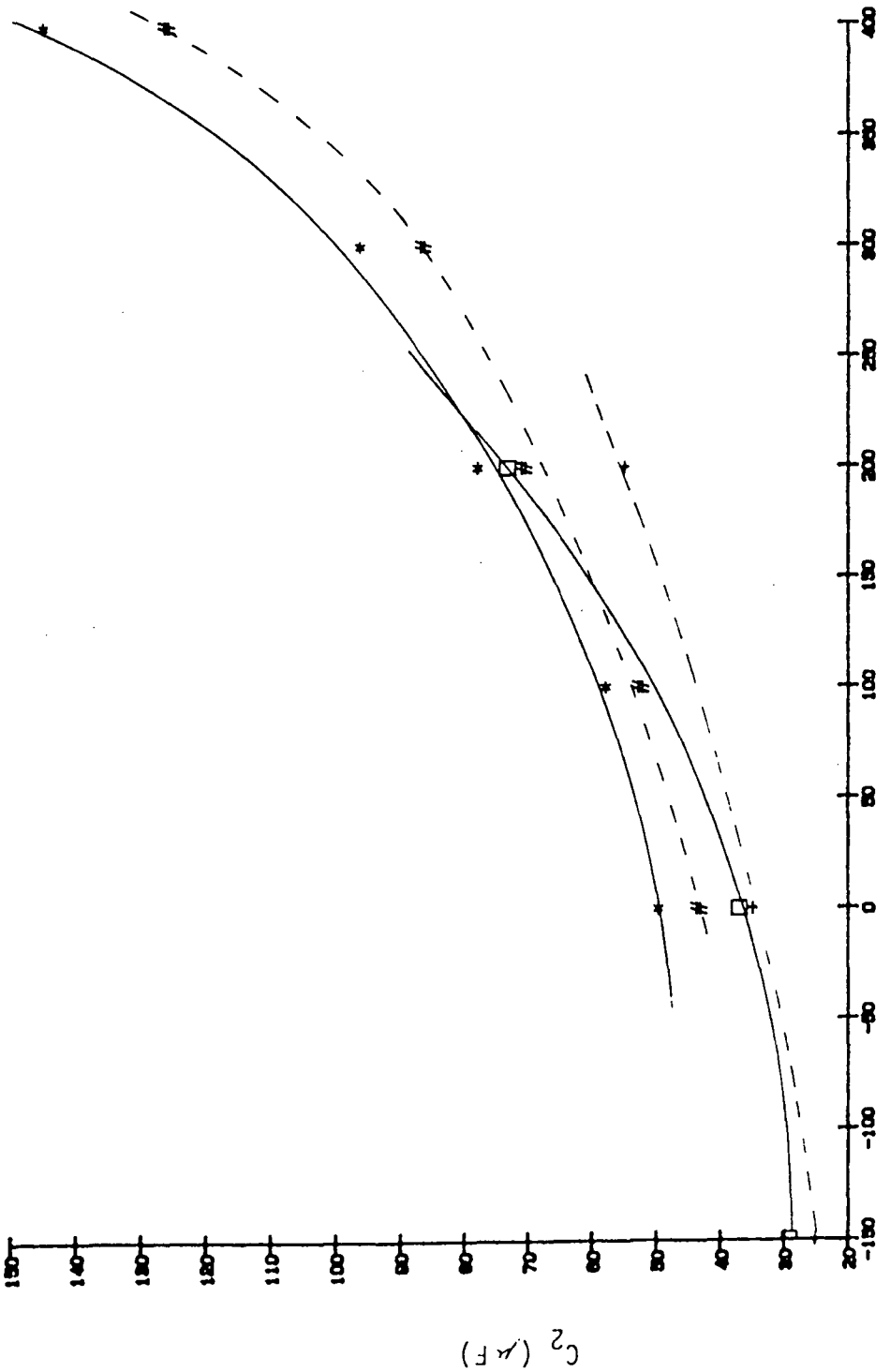

Figure 36. Data from Figure 35 expanded to resolve the low potential region.

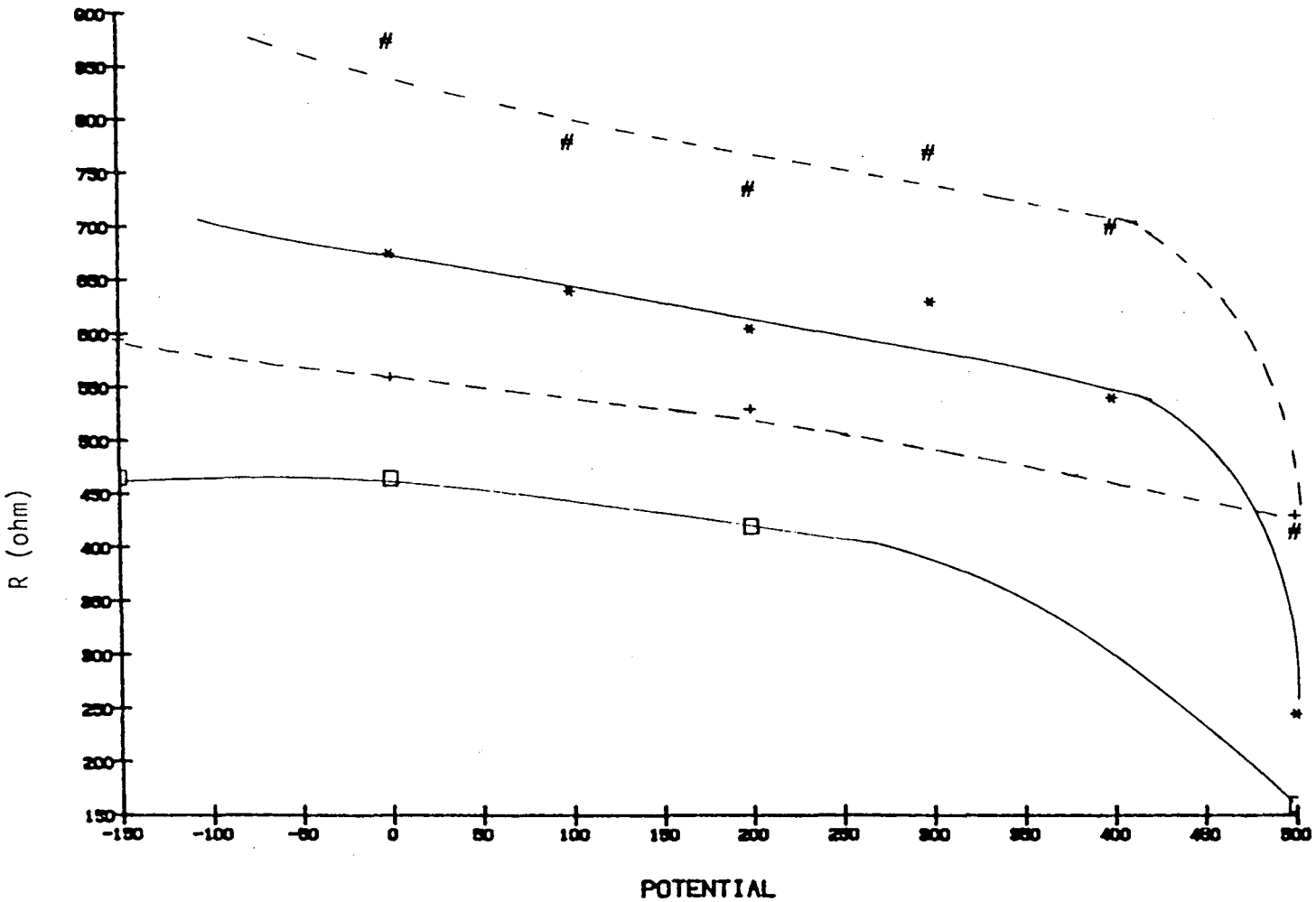

Figure 37. Dependence of resistance R on potential for two applied dc bias sequences. Curves for R as specified in Figure 34.

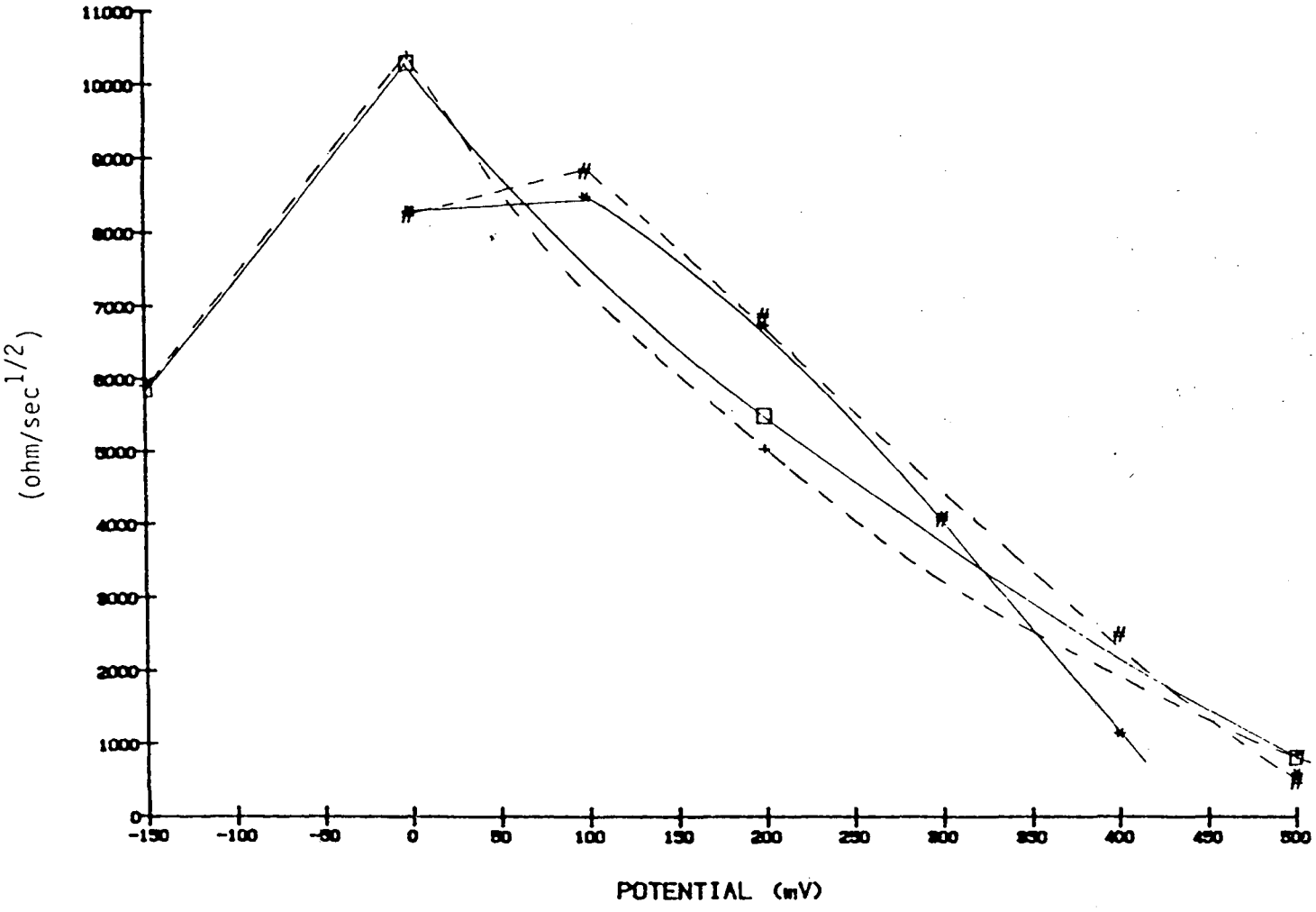

Figure 38. Dependence of the Warburg coefficient σ on potential for two applied dc bias sequences. Curves for σ as specified in Figure 34.

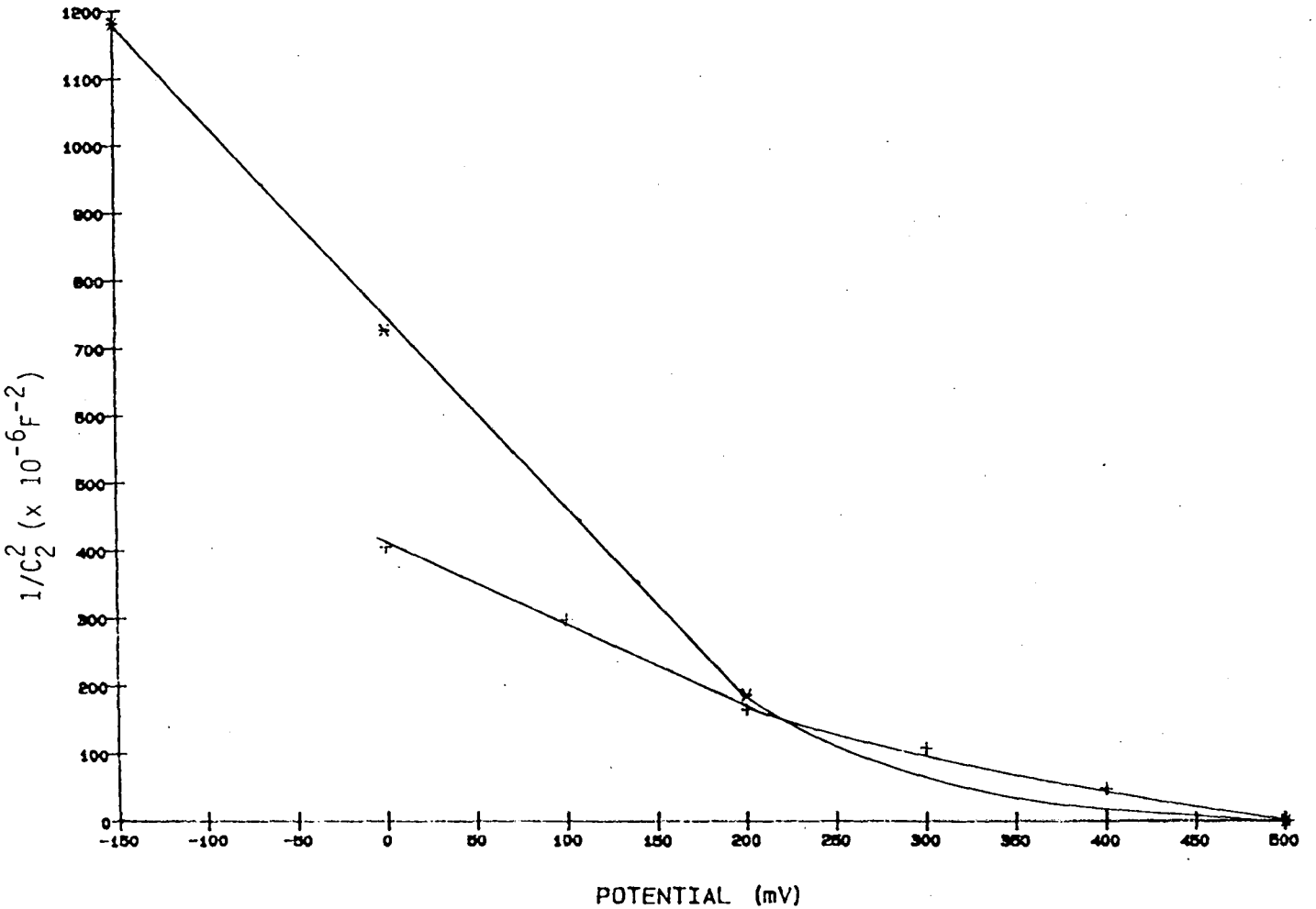

Figure 39. Mott Schottky plot of $1/C_2^2$ against E using capacitance C_2 data for the equivalent circuit shown in Figure 28.

in Figure 28. Madou and McKubre[36] also observed a linear dependence over this potential range. Their slope was about one order of magnitude more negative (about -3.4×10^7 compared with -2×10^6 mV^{-1} μF^{-2}), indicating an acceptor concentration of about one order of magnitude larger ($4 \times 10^{20}/cm^3$ compared with $2.4 \times 10^{19}/cm^3$) since the slope and acceptor concentration are inversely related[36]. Values of the capacitance derived from the circuit shown in Figure 29 do not obey the Mott-Schottky relationship as indicated by the curvature in Figure 40. These results suggest that the circuit in Figure 28 is a better model even if only on the basis that it allows the capacitance of the space charge region to be more clearly resolved. However, the imaginary part of the electrode impedance (Z") at 1 kHz is approximately inversely proportional to the capacitance causing the high frequency relaxation shown in the Bode plots. If this capacitance conforms to the Mott-Schottky relationship, a plot of $(Z")^2$ versus E will be linear. No equivalent circuit is assumed for such a plot. Figure 41 shows data taken from two measurement sequences over the range -0.15 to 0.5 V. A linear dependence is observed for both sequences between about -0.15 to 0.2 V, indicating that the high frequency capacitance, C_2, for either of the proposed circuits can be identified with the space charge layer.

A similar assertion was made previously by Madou and McKubre[36] and Tench and Yeager[45] for their respective electrolytes, as discussed in Section 1.1.5. Specifically, the capacitance was associated[45] with a depletion layer of p-type charge carriers in the semi-conducting hydroxide film.

Clearly, the Warburg impedance is not parallel to the space charge capacitance, C_2 and it therefore must relate to a diffusion process in the "bulk" film, assuming that distinct space charge and bulk layers exist.

The resistance in parallel with the space charge capacitance in Figure 28 may be associated with an electronic leakage current through the depletion layer, although the magnitude of this resistance would seem to be small for a space charge depletion layer. Such a parallel combination is commonly placed in equivalent circuits describing semiconductor electrodes,[80,81] although no order of magnitude for this type of resistance is readily available. However, the resistance may also correspond to a charge transfer process involved in the formation of $Ni(OH)_2$.

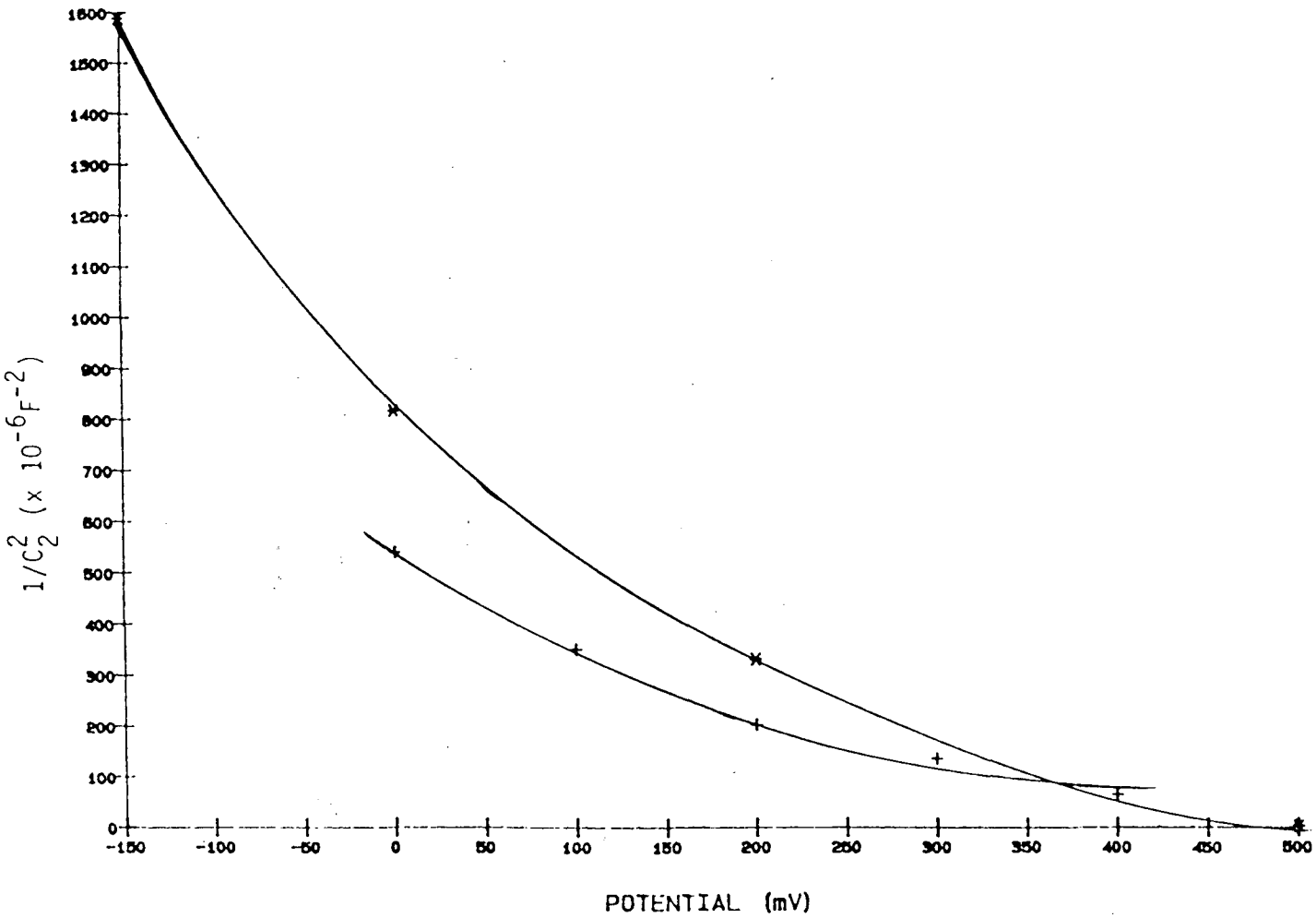

Figure 40. Mott Schottky plot of $1/C_2^2$ vs E using capacitance C_2 data for the equivalent circuit shown in Figure 29.

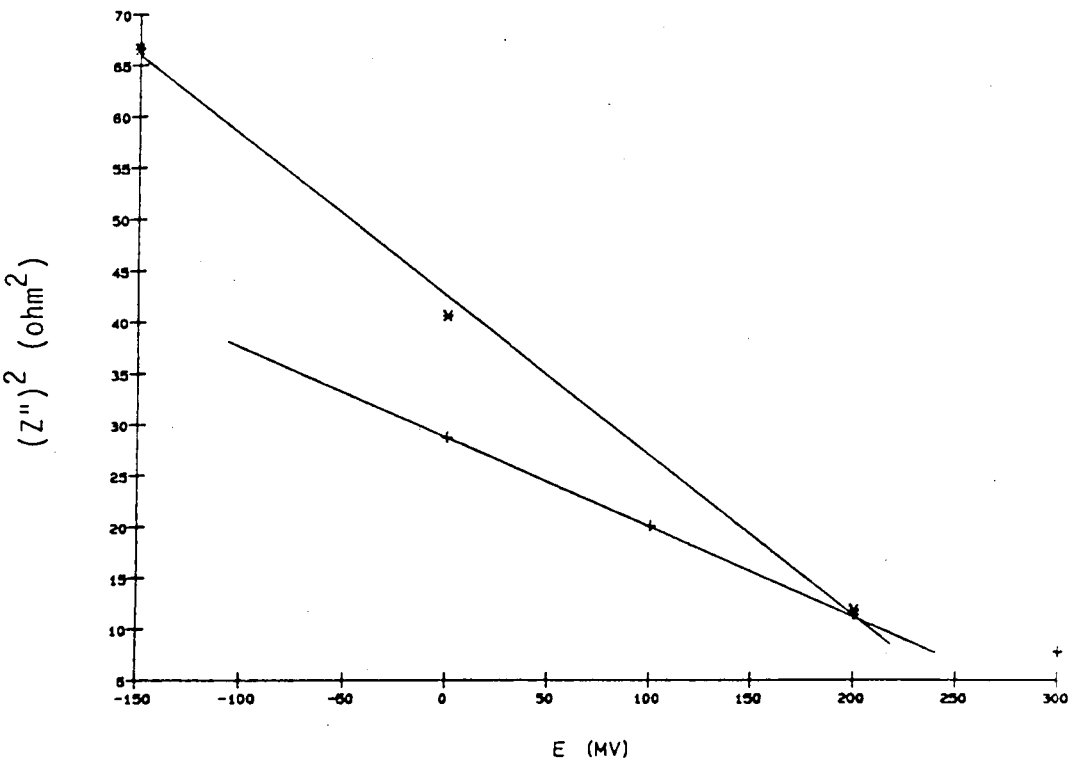

Figure 41. Dependence of $(Z")^2$ on potential for two applied dc bias sequences. Z" is the imaginary part of the electrode impedance of 1 kHz.

The impedance data at lower frequencies can be represented by a capacitance in parallel with a Warburg impedance. Although a semi-infinite diffusion layer is assumed, for the Warburg impedance (Equation 2), a finite diffusion layer will exist if mass transport occurs in the hydroxide or oxyhydroxide film.

Curve fitting results suggest that the semi-infinite diffusion layer assumption is just adequate for representing impedance data at low frequencies down to 63 mHz. The finite diffusion layer equation is required to represent phase angle data at lower frequencies, since a parallel W/C circuit for which a semi-infinite diffusion layer is assumed cannot produce a phase angle below 45°. Zimmerman *et al.*[63] observed an infinite diffusion layer Warburg impedance in the $Ni(OH)_2/NiOOH$ transition region but concluded that a solid state diffusion process comprising proton transport within the film was involved. Madou and McKubre also observed a Warburg impedance and showed that the electrode impedance was independent of electrode rotation speed. This confirmed that the diffusion process occurred within the film, and they likewise considered the diffusing species in the $Ni(OOH)_2/NiOOH$ conversion region to be protons.

Zimmerman and co-workers calculated the product of $CD^{1/2}$, where C and D are the concentration and diffusion coefficient of the proton, respectively, to be 1×10^{-7} mol cm^{-2} $s^{-1/2}$, while Madou and McKubre obtained a corresponding value of 3×10^{-9} mol cm^{-2} $s^{-1/2}$. Neither of these groups reported any potential dependence, and both of them used thick film electrodes. Zimmerman and co-workers used porous electrodes while Madou and McKubre used potentiodynamically cycled electrodes. Some porosity is possible on the latter electrodes.

For the thin films used in the present study, the Warburg coefficient was found to be potential-dependent. At ambient temperature, the value of $CD^{1/2}$ ranged from about 1×10^{-11} mol cm^{-2} $s^{1/2}$ at 0 V to 3×10^{-10} cm^{-2} s^{-1} at 0.5 V.

The $CD^{1/2}$ value obtained in this study for 0.5 V is an order of magnitude smaller than the value reported by Madou and McKubre, and three orders of

magnitude smaller than that found by Zimmerman et al. The combined data from all three studies show a clear trend to smaller values at $CD^{1/2}$ with thinner and/or less porous films.

It is well established in the literature[89] that the Bode plots in Figures 23 and 24 can also be produced by capacitive behavior at both high and low frequencies. The log Z versus log ω slopes approach -1 over the high and low frequency ranges, and two phase angle maxima occur within these ranges. Two separate capacitive relaxations are possible, and the equivalent circuits shown in Figures 42 and 43 were examined as models.

These circuits are also found to be adequate models from which the impedance data can be fairly well reproduced. At 0 V, for example, values of R_2 and C_2 approaching 100 kΩ and 700 μF, respectively, are required to obtain a reasonable low frequency fit. If a film thickness of 50 Å is assumed, the value of R_2 corresponds to a resistivity of 2×10^{11} Ω cm which is similar to the value reported for films on iron[92].

Another circuit exhibiting two capacitive relaxations is shown in Figure 44. This circuit can also reproduce the measured impedance spectra reasonably well. It is commonly used for modelling the impedance of semiconducting films. The parallel R_1/C_1 components describe the space charge layer, while the series R_2C_2 components describe surface states, typically at the semiconductor/electrolyte interface[45,48,82]. Preliminary curve fitting results showed that the R_2C_2 product required to fit the low frequency impedance spectra at 0 V is about 0.3 s, whereas Bard et al.[82] report values of 10^{-5} to 10^{-4} s for a number of semiconductors in non-aqueous electrolytes.

The large difference in time constants may indicate that surface states within the bandgap do not cause an observable relaxation within the experimental frequency range, or that the surface states relax very slowly on nickel films in aqueous environments. If surface states are presumed to arise from lithium ion incorporation/adsorption in or on the film, then removal of lithium ions from the electrolyte should eliminate the low frequency capacitive behavior from the impedance spectra. Such an experiment was performed, but the low frequency capacitive behavior was still observed. Intrinsic

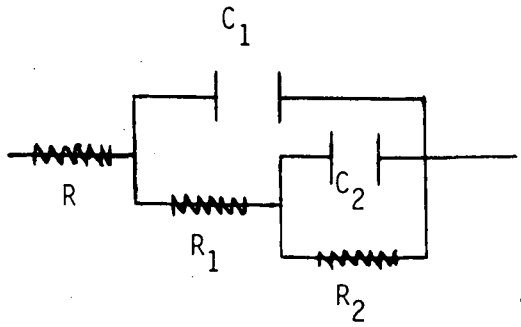

Figure 42. Alternate equivalent circuit for planar nickel electrode impedances.

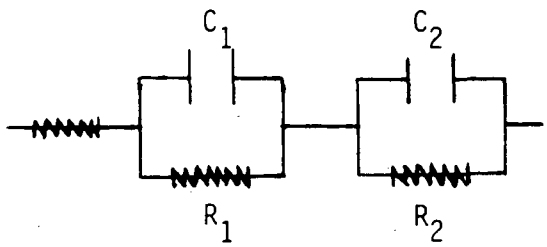

Figure 43. Alternate equivalent circuit for planar nickel electrode impedances.

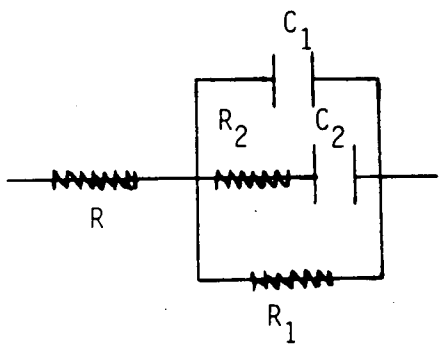

Figure 44. Alternate equivalent circuit for planar nickel electrode impedances.

surface states arising from the discontinuity in the lattice structure at the film/electrolyte or film/metal interfaces can still be present, so a surface state capacitance cannot be ruled out.

All of the equivalent circuits described in this section model the low frequency relaxation as a capacitance in parallel or in series with a resistance, or in parallel with a Warburg impedance. The capacitance ranges from about 118 to 1570 $\mu F\ cm^{-2}$ at potentials from -0.15 to 0.5 V, respectively, for all of the circuits. Values of 1/C are not linearly dependent on E (Figure 45), and are too large to be associated with the dielectric capacitance of the film. Similarly, the values of the capacitance are, in general, too large for a typical double layer capacitance, and do not obey the Mott-Schottky relationship (Figure 46). Furthermore, Madou and McKubre[36] and Zimmerman et al.[63] observed only a Warburg impedance at low frequencies on thick film electrodes. Nevertheless, the large capacitance was regularly observed at low frequencies in the present Bode plots and is most likely a pseudo-capacitance associated with the adsorption of some species on the hydroxide film surface.

4.2.2 Impedance Data at Non-Ambient Temperatures

Planar electrode impedance spectra were recorded for temperatures of 0, 23, 40, 60 and 100°C. Spectra were similar at temperatures from 23°C to 100°C. However, at 0°C the high frequency relaxation shifts markedly to lower frequencies, and only the beginning of the low frequency relaxation is observable at the minimum frequency employed (Figure 47 and 48). At the higher temperatures, higher minimum frequencies were required to avoid data scatter due to extraneous noise, and again only the beginning of the lower frequency relaxation is observable.

Despite the restricted low frequency region, the features of the non-ambient temperature data appear very similar to the ambient temperature spectra. It therefore seems reasonable to assume that the same equivalent circuits remain applicable, and that the components are only moderately affected by temperature, except at 0 V where large increases in both capacitances are observed.

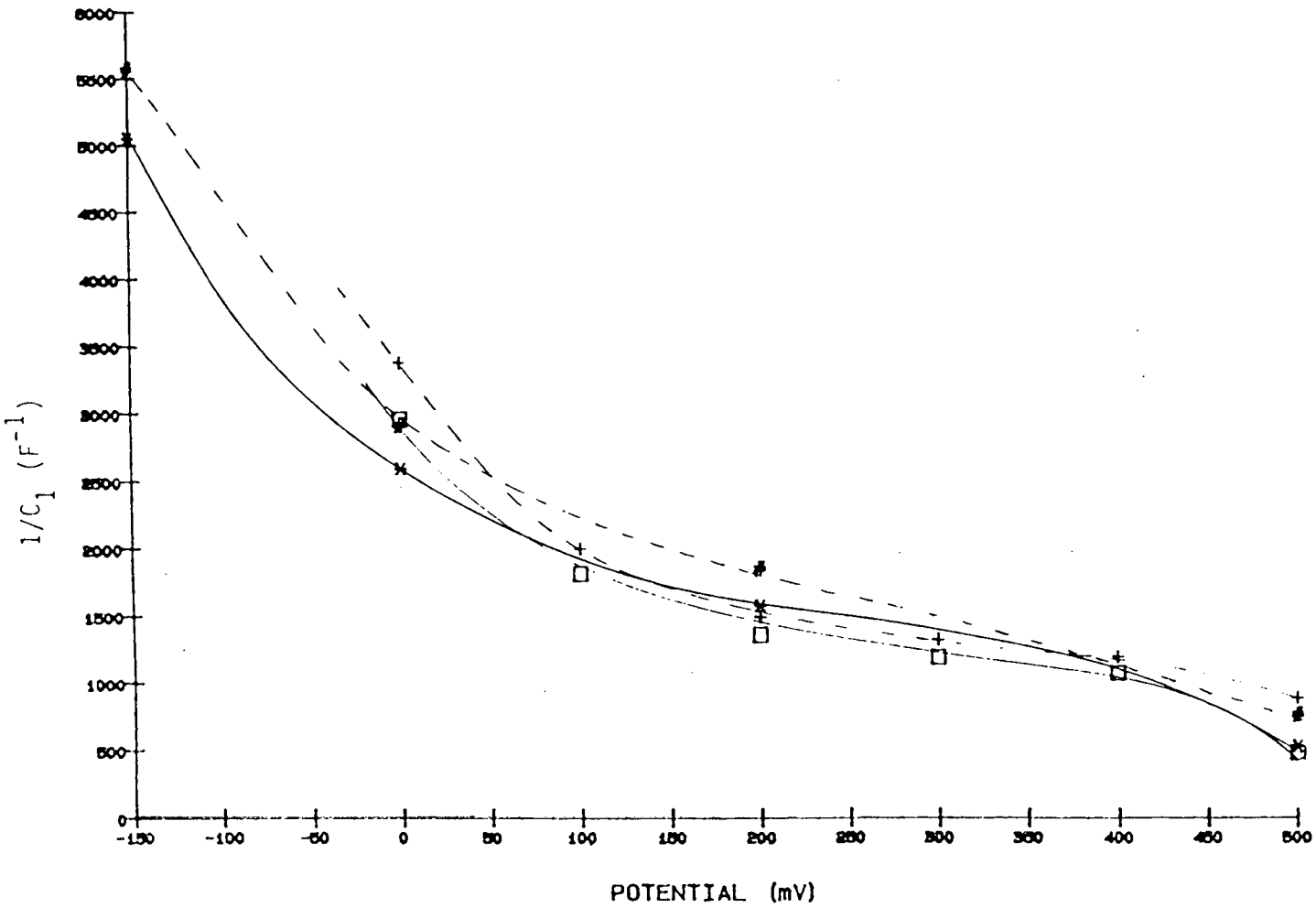

Figure 45. Dependence of $1/C_1$ on potential. Values of C_1 were derived for the equivalent circuits shown in Figures 28 (———) and 29 (-----).

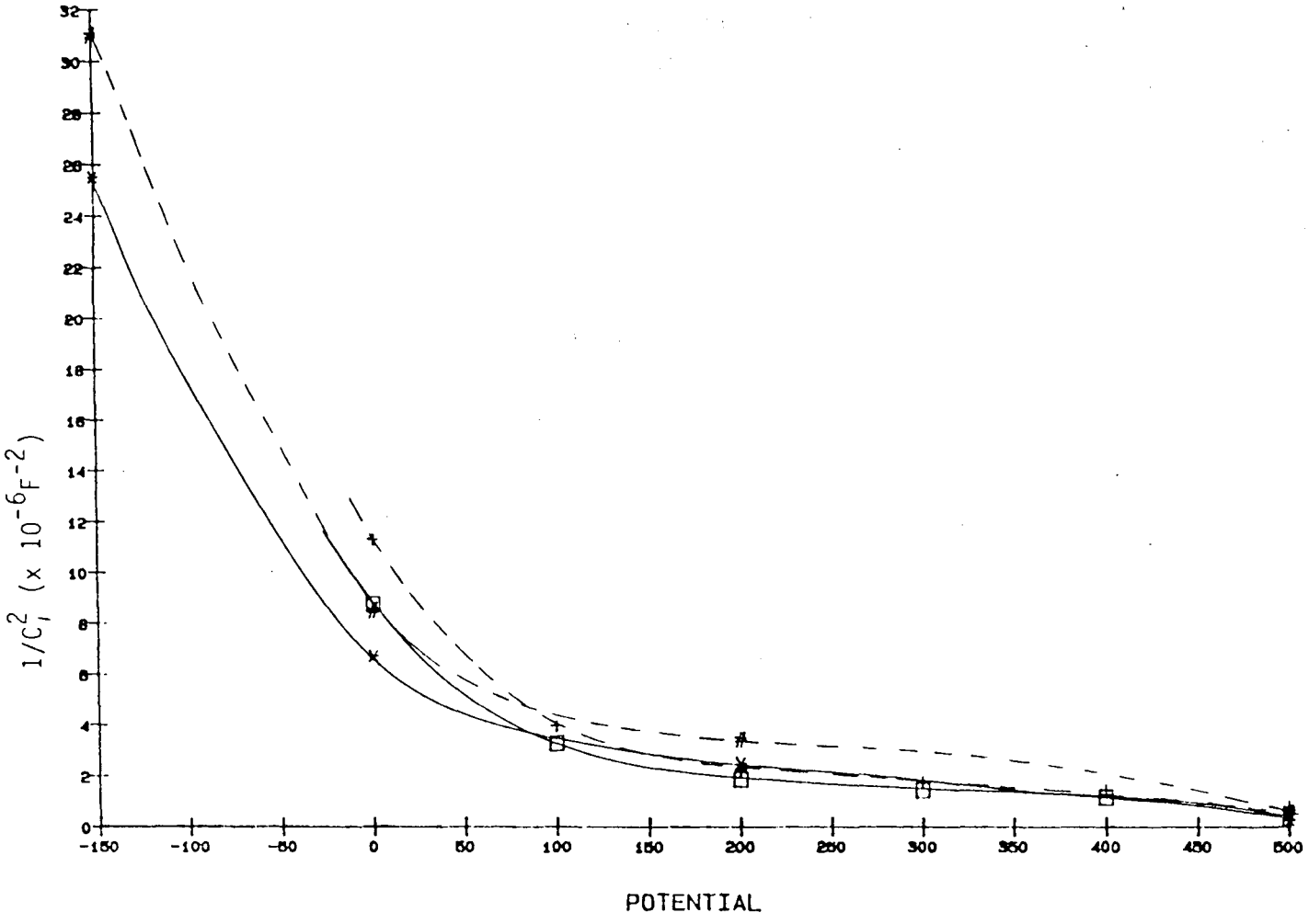

Figure 46. Mott Shottky plot of $1/C_j^2$ against E using capacitance C_j data for the equivalent circuit shown in Figures 28 (———) and 29 (-----).

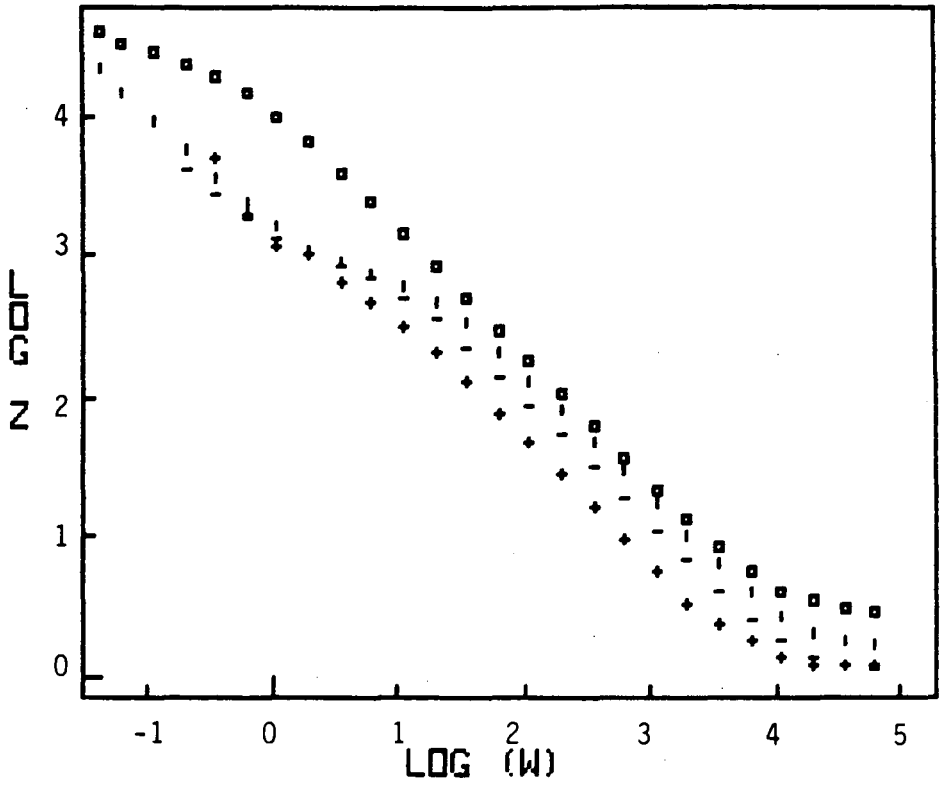

Figure 47. Bode plot of log |Z| data for a planar electrode at 0.2 V and 0 (□), 23 (1), 60 (-), and 100°C (+).

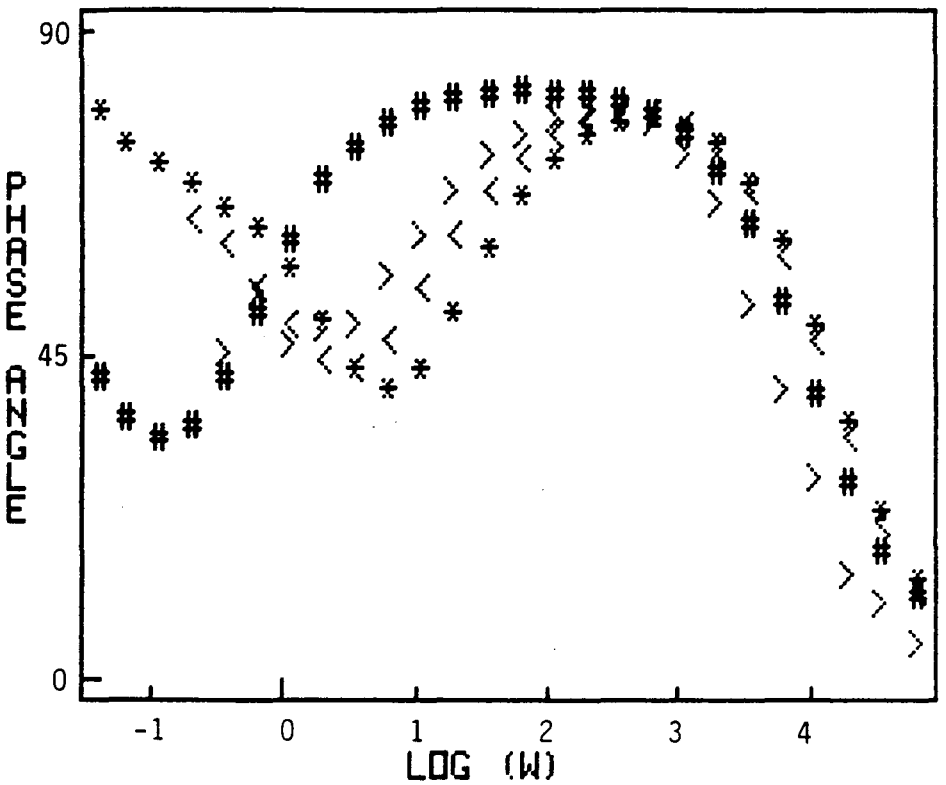

Figure 48. Bode plot of phase angle data corresponding to Figure 47 at 0 (#), 23 (*), 60 (<), and 100 (>).

5.0 POROUS BATTERY ELECTRODE IMPEDANCE

The transmission line model (TLM) in its three dimesional form contains eight independent variables (see Section 1.3). Two of these variables are the pore wall and backing plate interfacial impedances which are treated as planar electrode impedances in this study, as discussed in Section IV. It was shown in the previous section that the impedance of a planar nickel electrode can be represented by various equivalent circuits. However, the four components (ignoring the solution resistance) contained in each of these circuits, in addition to frequency and applied dc potential, makes a total of 16 variables required to define the impedance of a porous nickel battery electrode.

In this section, the TLM is used to study the degradation processes of porous electrodes. Each of the 16 variables in the model are first determined as accurately as possible in separate measurements. Theoretical impedance spectra are then calculated from the model and are compared with experimental spectra. Adjustments to key parameters allow the theoretical spectra to progressively follow the experimental impedance data during degradation induced by galvanostatic cycling at various temperatures. Despite the complexity of the TLM, the model clearly shows cycle dependent trends in several variables.

5.1 Initial TLM Parameter Value Assignments for Rolled and Bonded Electrodes

1. Pore wall and backing plate impedances, Z and Z', can be represented by the equivalent circuits for a planar electrode, as presented in Section 4. The components in these circuits are the only ones in the TLM with a well-defined dependence on frequency and potential. Any of the equivalent circuits shown in Figures 28, 29, 42, 43, and 44, could have been used to represent Z and Z'. However, the circuit shown in Figure 28 was considered to provide the most appropriate representation and was therefore selected for the TLM. Average values of the components at a given potential were used as initial inputs to the TLM.

2. The number of pores, n, varies with the number of galvanostatic cycles. Scanning electron micrographs of new and cycled rolled and bonded electrodes are shown in Plates 1 and 2, respectively of Figure 49. No pores

Plate 1. Uncycled.

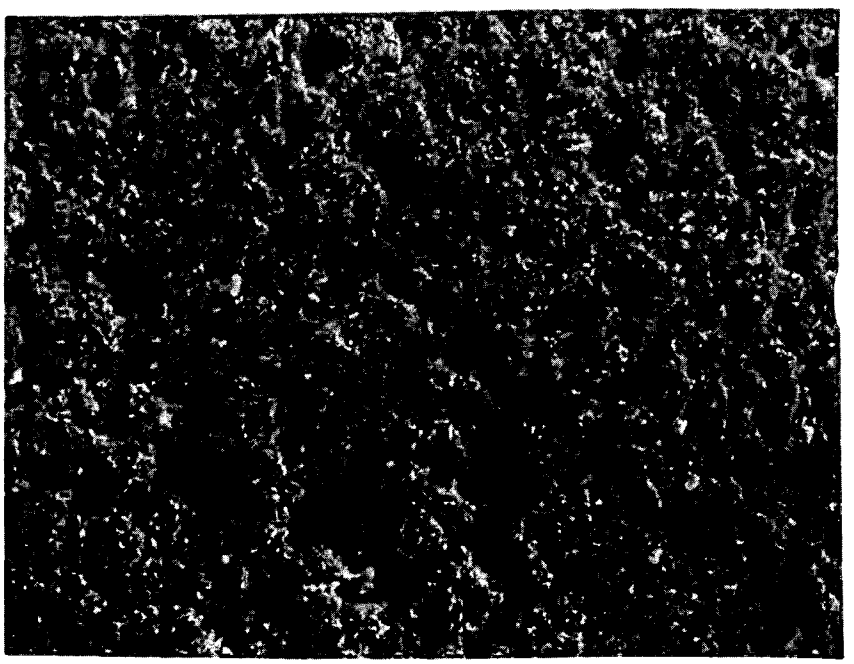

Plate 2. Cycled 26 times with 40 minutes charging time to rated capacity and 20 minutes discharge time to 100% DOD.

Figure 49. Scanning electron micrographs (100x) of rolled and bonded electrode at 0°C.

are visible on the new electrode, while many thousands are visible on the cycled electrode.

It is assumed in the derivation of the TLM that all pores on the electrode are identical in size. The pore size distribution in Plate 2 varies from a maximum diameter of about 64μm to some diameter too small to be resolved. However, most of these pores do not carry a significant current. If electrolyte concentration gradients are neglected, the resistance of the solution within a pore is given by $(\rho_s \ell/A)$ where ℓ is the length. This resistance is larger in smaller diameter pores, and in the limit of small pore diameter, virtually no current flows in the pore solution so that the pore is effectively inactive. The three dimensional form of the TLM does not allow for pore diameter variations, so pore uniformity is implicitly assumed. A fraction of the total number of pores visible in Plate 2 is used here to allow for the inactivity of smaller pores. The number of pores, n, used in the TLM is between 0 and about $1 \times 10^5/cm^2$ depending on the number of galvanostatic cycles. The latter number is arbitrarily taken as 2/3 of the total number of pores, about $1.5 \times 10^5/cm^2$, resolvable in Plate 2.

3. The average pore length, ℓ, can be approximated as the thickness of the electrode (0.11 cm).

4. The projected electrode area is 1.27 cm^2 for rolled and bonded electrodes.

5. The fraction of the total surface area covered by pores $(1-\theta)$ in Plate 2 is roughly 0.3. In Plate 1, it is clearly about 0.0. Since n increases with the number of galvanostatic cycles, $1-\theta$ must likewise increase.

6. The resistivity of the solution, ρ_s, within the pores is dependent on the KOH concentration. In this study, the KOH concentration is assumed to be essentially constant along the length and radius of the pores since the use of a high concentration of KOH should avoid electrolyte depletion with the pores. While this assumption may not be strictly obeyed, the KOH/H_2O conductivity data of Lown and Thirsk[86] show that a 60% increase in conductivity is realized by halving the KOH concentration from 8 M to 4 M.

This is within an order of magnitude, whereas the uncertainty in the number of pores is much greater. Therefore, the solution resistivity is approximated as a constant having a value[86] of 3.1 Ω cm.

7. The solid phase resistivity, ρ_m, is expected to increase with the number of galvanostatic cycles. A loss of capacity during cycling can be caused by a loss of cohesion between the particle-particle bonds comprising the porous electrode, thereby causing an increase in the solid phase resistivity. The solid phase in rolled and bonded electrodes contains graphite which has a resistivity[4] of 0.0014 Ω cm while the resistivity of nickel hydroxide can be approximated as 1×10^{11} Ω cm at 0 V and 23°C. The latter resistivity is obtained by extrapolating electrode impedance spectra for a planar electrode to the real axis in order to obtain a polarization resistance which is then multipled by A/ℓ, where A is the electrode area (1.27 cm^2), and ℓ is the film thickness of about 50 Å. This assumes that firstly, the double layer and other electrolyte effects do not influence the impedance data of the planar electrode at low frequencies, and secondly, the polarization resistance is essentially determined by the resistance of the film. The initial uncycled value of the solid phase resistivity is arbitrarily taken as 10 Ω cm. The graphite is assumed to significantly influence the solid phase resistivity.

5.2. TLM Modelling of the Impedance of Rolled and Bonded Electrode Impedances

The equations from the transmission line model were incorporated into a computer program written in Applesoft Basic for Apple II-Plus microcomputers (Appendix 3). The interfacial and backing plate impedances were calculated using the impedance equations derived for the equivalent circuit shown in Figure 28. Applesoft Basic contains no special capabilities for handling complex numbers, so all computations were performed by treating the real and imaginary parts of the impedance data as separate arrays, and using the established rules of complex algebra. The program produces Bode plots of the theoretical and experimental impedance data for a given a set of parameters in the TLM.

The program was used to obtain an approximate theoretical fit of experimental data. A trial and error method was employed. After an approximate fit was obtained, parameter value assignments were subsequently optimized with a commercial software package called OPTDES (Design Optimization).

OPTDES was used to minimize the sum of squares error in the complex plane. In a typical optimization sequence, the interfacial and backing plate impedances for 0 V and electrode area were held constant while the remaining variables were optimized. Some or all of the components in the interfacial and backing plate impedance expressions were then allowed to vary along with the other variables. Direct substitution of the parameter value assignments described in Section 5.1 produces the theoretical impedance spectrum shown in Figures 50 and 51.

For comparison, experimental impedances are shown for a rolled and bonded electrode cycled twice at 23°C, with 40 minutes charging to rated capacity, and 20 minutes to 100% DOD. The experimental data were measured after the electrode was held for one hour at 0 V, as described in Section 2.

Figures 50 and 51 show that the features of the experimental impedance spectrum are present in the theoretical spectrum. However, the fit of the theoretical curve clearly needs to be improved. The OPTDES curve fitting procedures indicated that small adjustments to several parameters significantly reduced the sum of the squares error between the experimental and theoretical spectra. These adjustments from the initial value assignments are discussed below.

1. The pore length, ℓ, required for an improved fit of the theoretical data is about three times the electrode thickness of 0.35 cm. Evidently, tortuosity of the pores increases the active pore length by this amount.

2. The number of pores required for a good theoretical fit is about 23000. A smaller number was expected after only two galvanostatic cycles, since no pores are observed on new electrodes. However, the experimental data shown in Figures 52 and 53 lend some support to this finding. A large

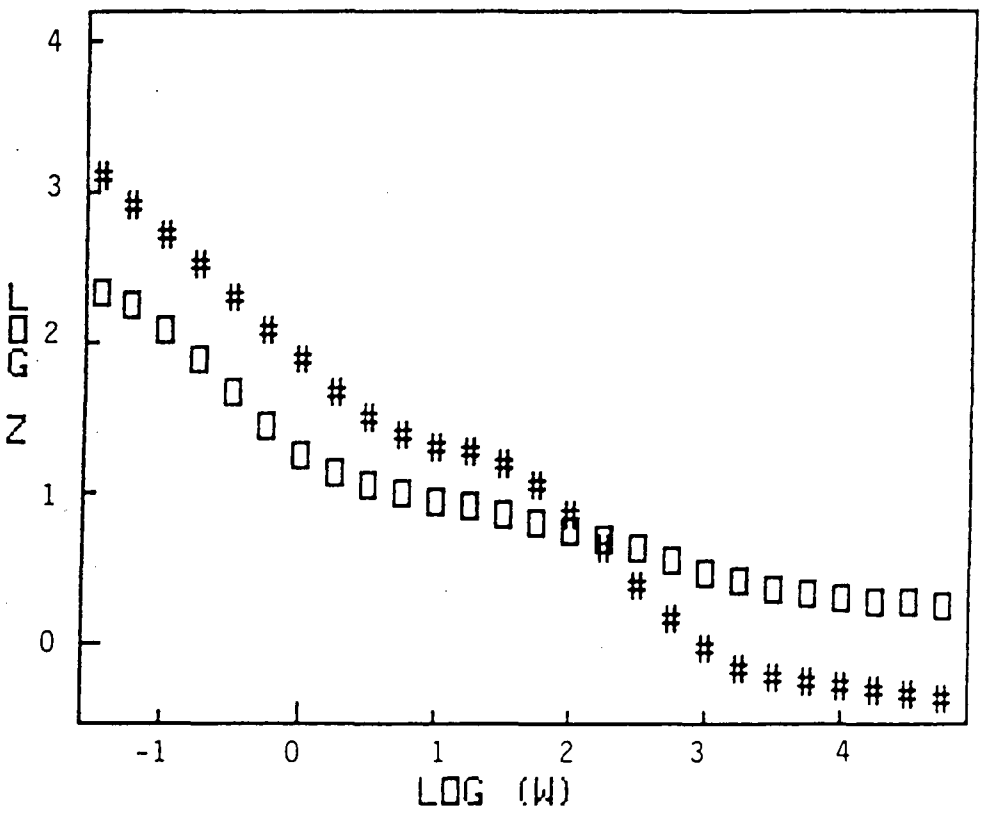

Figure 50. Bode plot of experimental (#) and calculated (□) log |Z| data for a porous rolled and bonded electrode at 0 V. The calculated data were obtained using the TLM and equivalent circuit shown in Figure 28. Cycling conditions: 40 min chg to capacity, 100% DOD in 20 min.

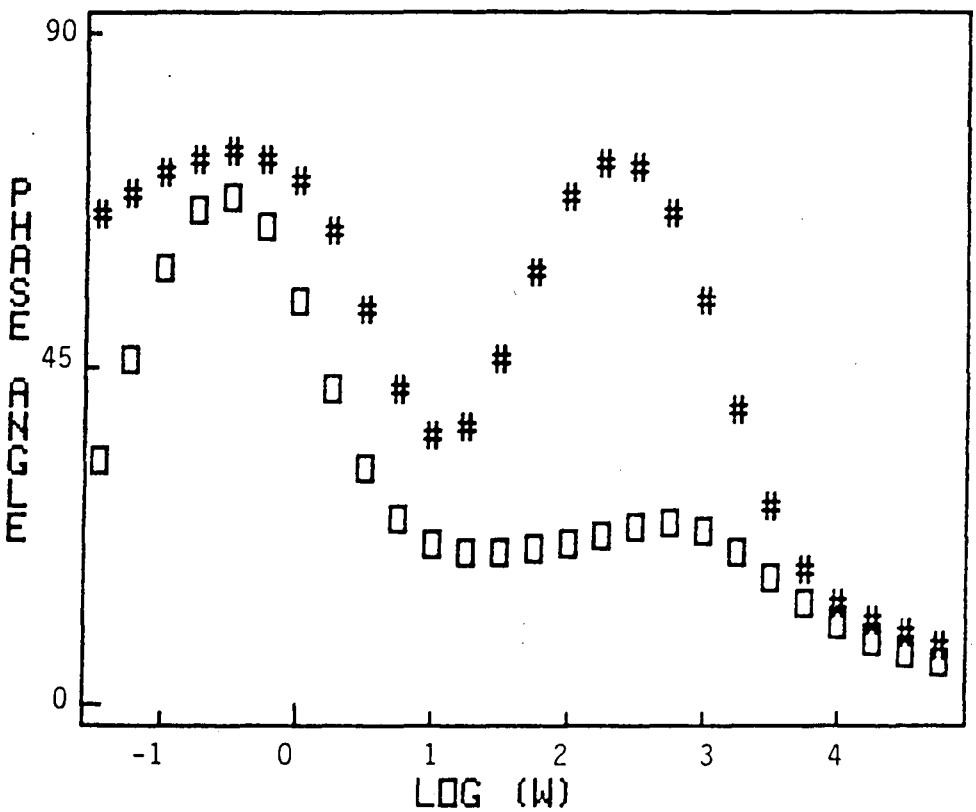

Figure 51. Bode plot of phase angle data corresponding to Figure 50.

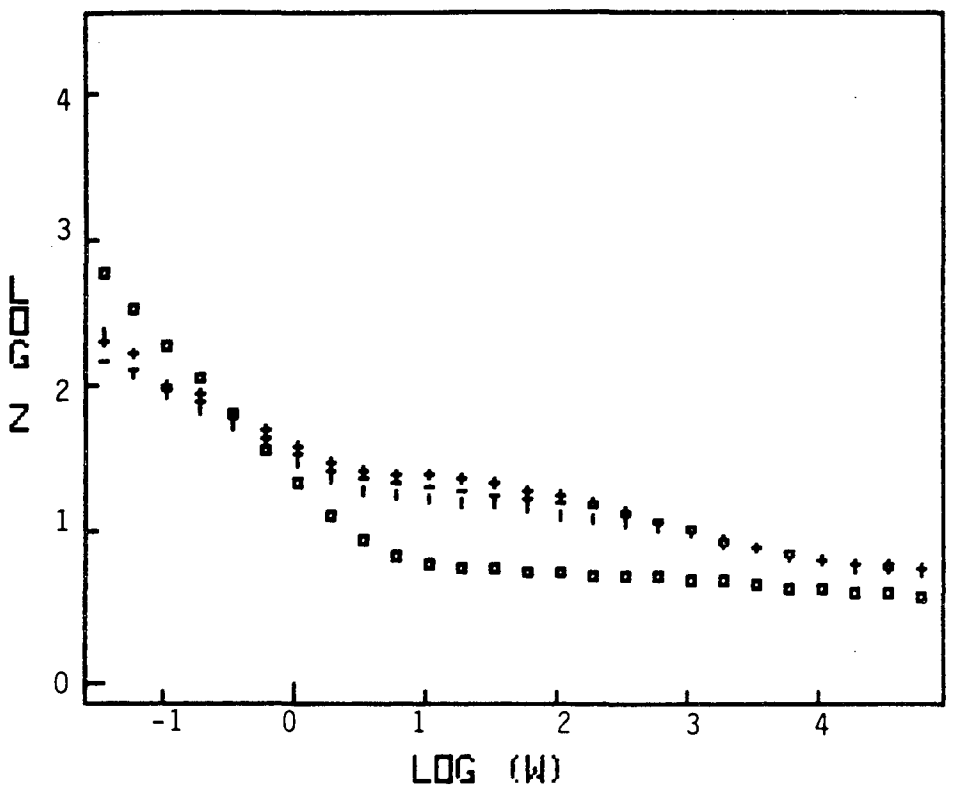

Figure 52. Bode plot of log |Z| data for a rolled and bonded electrode at 0°C and 0 V after 1 (□), 4 (1), 11 (-), and 24 (+) galvanostatic cycles. Each cycle consisted of 40 min chg to capacity and 100% DOD in 20 min.

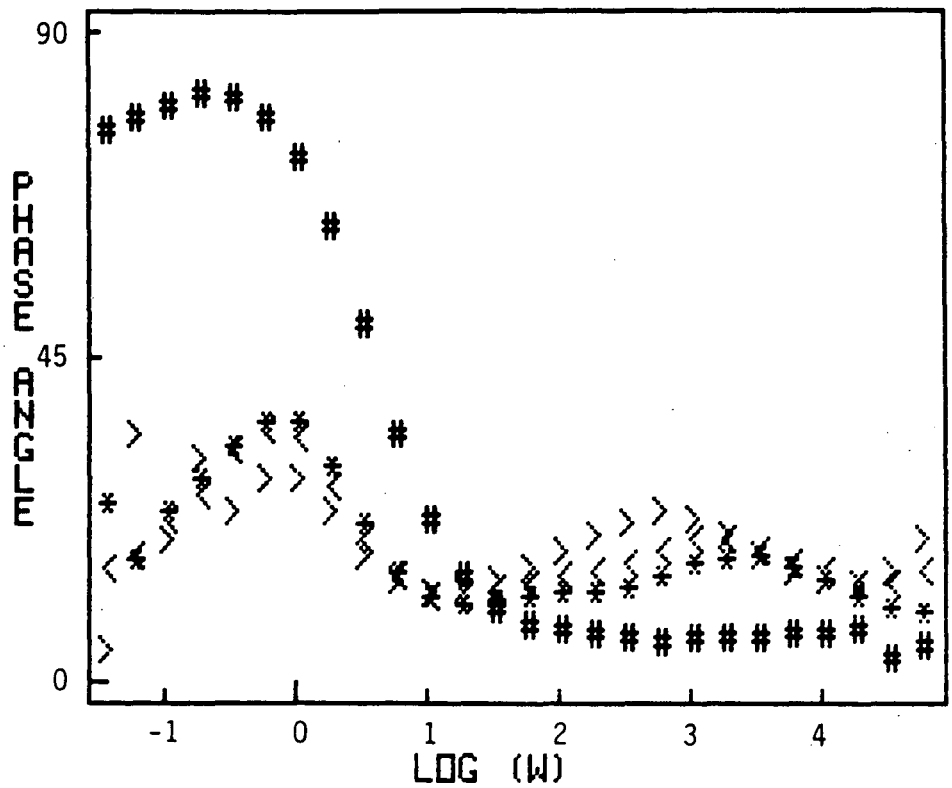

Figure 53. Bode plot of phase angle data corresponding to Figure 52 for 1 (#), 4 (*), 11 (<), and 24 (>) galvanostatic cycles.

change in the impedance spectra is observed between the first and fourth cycles. On subsequent cycles, only relatively small changes in the spectra are observed. This suggests that significant structural and/or electrochemical changes occur within the electrode during the first few cycles. The number of pores presumeably increases rapidly over this stage but remains relatively constant after the first few "conditioning" cycles. As discussed later, the TLM curve fitting shows that the number of active pores actually decreases somewhat after a large number of cycles.

3. The optimized surface coverage of pores ($1-\theta$) was found to be 0.33 which is in good agreement with the initial prediction of 0.3.

4. The optimized resistivities of the solid and solution phases were 9.3 and 4.5 Ω cm, respectively. The predicted values were 20 and 3.1, again showing reasonable agreement considering the uncertainty in estimating these values.

5. The pore wall impedance, Z, required a small change to improve the fit with experimental data. Specifically, the space charge capacitance was decreased from 42 μF to about 7 μF. The latter number was obtained by the curve fitting procedure described in Section IV for the impedance data of planar electrodes at 0 V and 23°C. Smaller space charge capacitances around 29 μF were obtained in a similar manner for the planar electrode at lower potentials such as -0.15 V.

With the above changes, the theoretical spectrum more closely fits the experimental data, as shown in Figures 54 and 55.

It is interesting that the backing plate impedance, Z', had little effect on the shape of the theoretical impedance spectra. This result supports previous findings involving a large pore length, and a large number of pores. Both of these paramenters are proportional to the solution resistance per pore and when large cause a redirection of current to the solid phase away from the solution/backing plate interface.

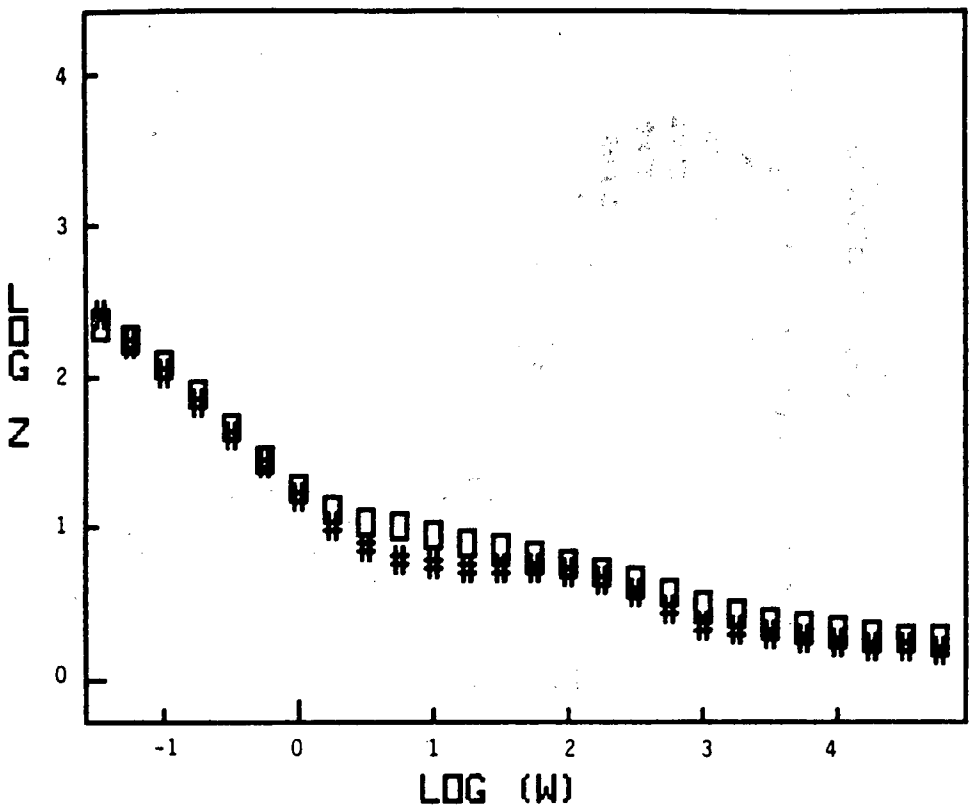

Figure 54. Bode plot of experimental (#) and calculated (□) log |Z| data at 0 V and 23°C for a rolled and bonded electrod cycled twice (40 min chg to capacity and 20 min for 100% DOD). Calculated data obtained from optimized TLM parameters described in text.

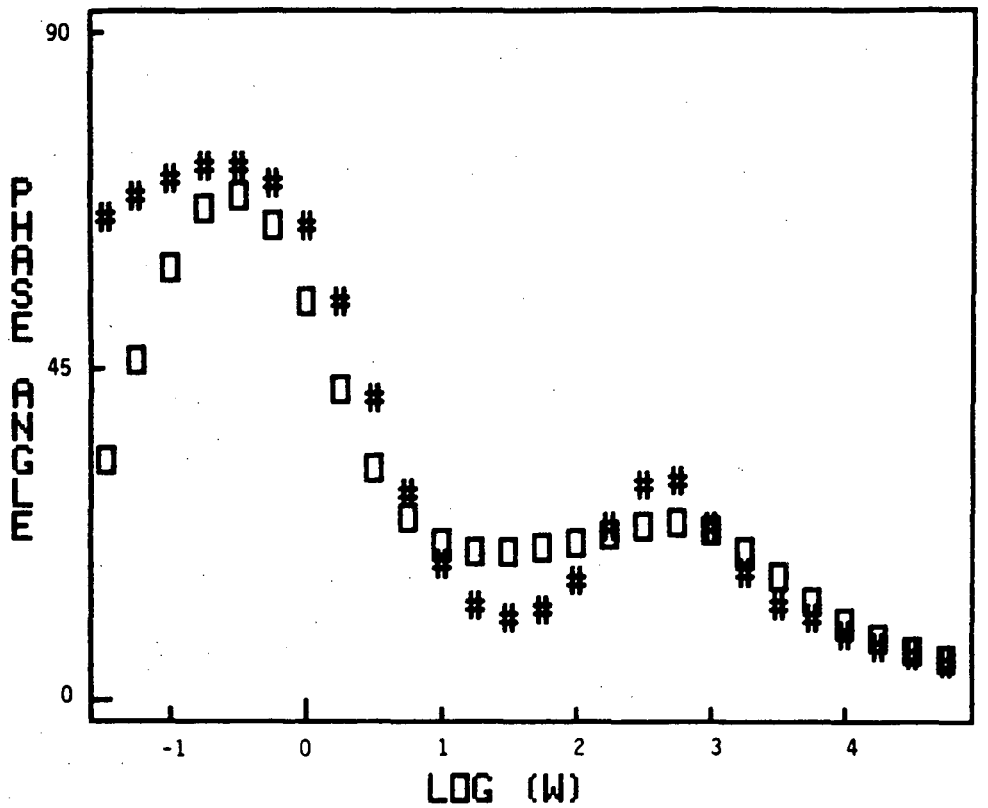

Figure 55. Bode plot of phase angle data corresponding to Figure 54.

The remaining variables in the pore wall interfacial impedance, specifically the resistance R, capacitance C_1, and Warburg coefficient σ, in Figure 28 were not optimized. Attempts to optimize these variables always resulted in a smaller sum of squares error, but with a simultaneous distortion of the theoretical spectrum. The optimization solfware clearly found pathways to reduce the sum of squares error by skewing the features of the theoretical spectrum. This may indicate that the best fit curves shown in Figures 54 and 55 represent only localized sum of squares minima and that a better fit might be found. More likely, it shows only that the optimization software in some cases can reduce the sum of squares error on curves with complex shapes by an unrealistic manipulation of a large number of variables. In this study, the reproduction of the essential features of the experimental impedance spectrum is considered to be more important than a smaller sum of squares error.

5.2.1 Cycle Dependence

Impedance spectra of rolled and bonded electrodes at ambient temperature are shown in Figures 56 and 57 after 2, 12, and 27 galvanostatic cycles. The magnitude of the impedance increases with cycle number at intermediate frequencies, while the phase angle maxima decrease at low frequencies and increase at high frequencies. This behavior can be modelled by optimizing the TLM parameters to minimize the sum of squares error betwen the experimental and theoretical impedance data. The parameters were adjusted as follows:

1. The optimized active pore length decreased from 0.35 to 0.28, and then to 0.20 after 2, 12, and 27 cycles, respectively. A considerable amount of the active material had spalled from the electrode by the end of 27 cycles, and was found scattered throughout the test cell. This could account for the decreased pore length. However, the electrode also became swollen during the test, and after 27 cycles, the net thickness at the center of the electrode was actually larger than the original thickness. The observation of spalling suggests that the solid phase particles still bound to the electrode but farthest from the backing plate were not active. The solid phase resistivity between these outer particles may have been so large that they did not participate in the electrochemical processes, and the pore length effectively decreased. On the other hand, the decrease in pore length accompanied by swelling is consistent with a

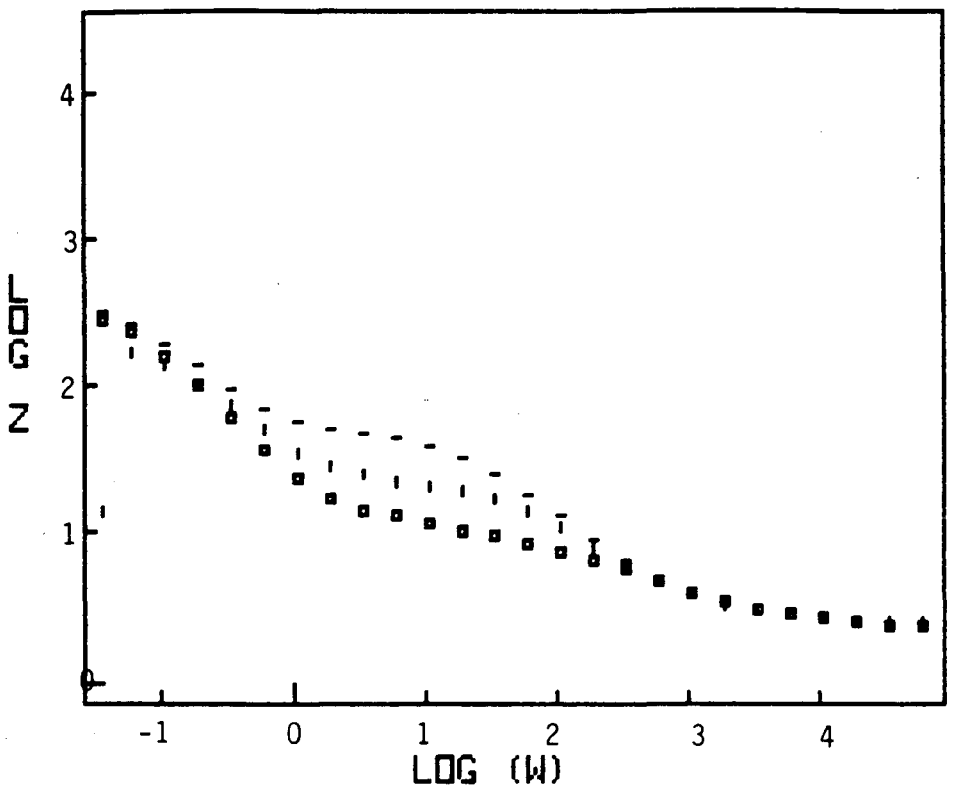

Figure 56. Bode plot of experimental log |Z| data for rolled and bonded electrode at 0 V and 23°C after 2 (□), 12 (1), and 27 (-) cycles (40 min chg to capacity and 20 min for 100% DOD).

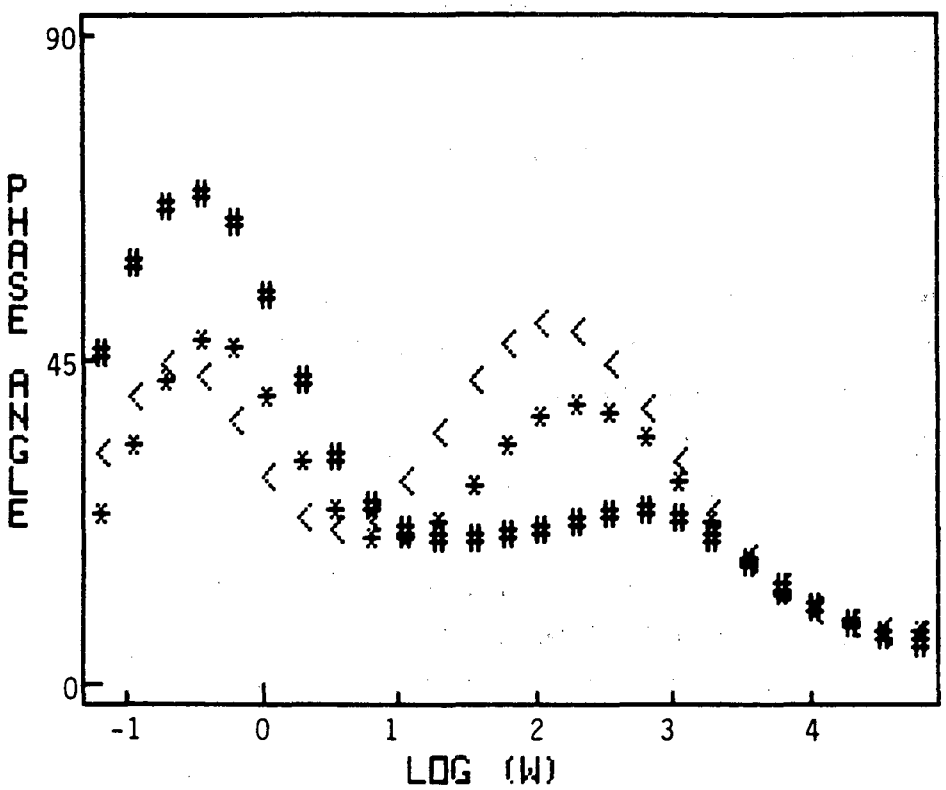

Figure 57. Bode plot of phase angle data corresponding to Figure 56 for 2 (#), 12 (*), and 27 (<) cycles.

restructuring of material within the active solid phase, possibly as a result of dissolution/precipitation processes.

2. Cycle dependent adjustments to the solid phase resistivity, ρ_m, supports the above assertion that the outer particles were not active. The average solid phase resistivity changed from 8.9 to 13.2 and then to 12.4 Ω cm after 2, 12, and 27 cycles, respectively. This cycle-dependent increase is readily explained by particle-particle bond damage or rupture during the swelling process. This rupture may result from stresses caused by volume changes associated with the interconversion of $Ni(OH)_2$ and NiOOH. Sloughing of the outer particles suggests that a resistivity gradient developed across the electrode, with the highest resistivity across the outer region.

3. Optimized values of the solution resistivity remained virtually constant throughout the cycling process. The resistivities after 2, 12, and 27 cycles were 4.5, 4.9, and 4.0 Ω cm, respectively. The lack of dependence on cycle number had been expected (Section 5.1) since the use of a high KOH concentration made electrolyte depletion within the pores unlikely.

4. The optimized pore covered fraction $(1-\Theta)$ increased slightly from 0.67 to 0.73, and then to 0.75 after 2, 12, and 27 cycles, respectively. This also is consistent with the observed swelling of the electrode after cycling.

5. As mentioned previously, the number of pores increased dramatically from approximately zero to about 23000 after just two cycles. With continued cycling, the TLM shows that it decreases from 23000 to 8500 and then to 3300 after 2, 12, and 27 cycles, respectively. These changes can be explained by the observed swelling and sloughing during cycling.

6. The optimized space charge capacitance in the pore wall interfacial impedance increases from 7 μF after cycle 2, to 34 μF after cycle 27. This latter value is approximately the same as that determined for planar electrodes at 0 V.

7. An adjustment to the Warburg coefficient in the pore wall interfacial impedance was also found to assist in the optimization procedure. The Warburg coefficient for the planar electrode at ambient temperature and 0 V was found to be about 9300 $\Omega\ s^{-1/2}$. This value was adequate for porous electrodes with two galvanostatic cycles, but for heavily cycled porous electrodes, a Warburg coefficient of about 1000 $\Omega\ s^{-1/2}$ was found to improve the low frequency fit.

The sum of squares error between experimental impedance spectra and optimized theoretical spectra for the TLM is greatest at low frequencies. Curve fitting of planar electrode impedance data to an equivalent circuit also shows discrepancies at low frequencies. Since the equivalent circuit for the planar electrode is used to represent the pore wall and backing plate interfacial impedances in the TLM, at least a part of the sum of squares error in the case of the porous electrode at low frequencies will be transferred from the corresponding error for the planar electrode. The sum of squares error for porous electrodes is less at high frequencies, largely because the impedance data for the planar electrode could be modelled satisfactorily.

5.2.2 Temperature Dependence

Impedance data for rolled and bonded electrodes for various cycle numbers and temperatures of 0° and 40°C are shown in Figures 52, 53, 58 and 59.

Again, the magnitude of the impedance increases with cycling, and the phase angle maxima decrease at low frequencies and increase at high frequencies. Except for the phase angle for cycle 31 and 40°C, no significant difference between the behavior for ambient and non-ambient temperatures is evident. It seems reasonable therefore to propose that the electrode degradation processes are similar over the temperature range from 0 to 40°C.

In the case of the exception to the impedance spectra mentioned above, the high galvanostatic currents used during cycling caused severe degradation reflected by gross spalling of the active material. It was not possible to obtain impedance data for rolled and bonded electrodes at either 60° or 100°C. Electrodes failed in less than one or two cycles, and each test was terminated before impedance data were measured. This failure was associated with severe spalling of the active material.

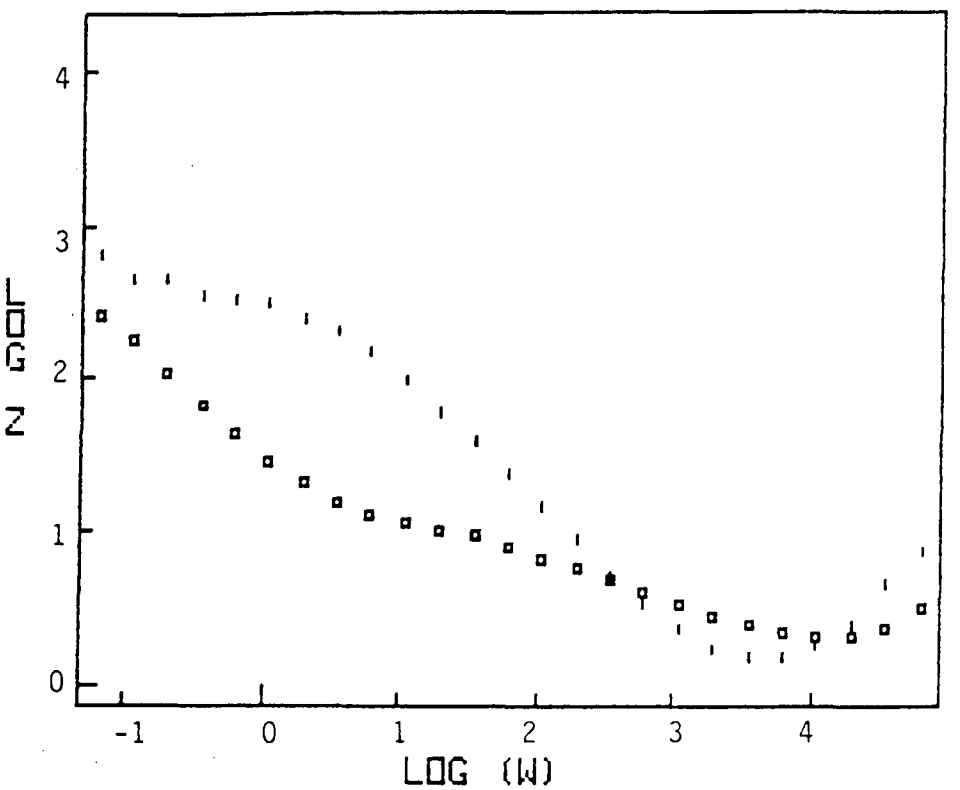

Figure 58. Bode plot of experimental log |Z| data for a rolled and bonded electrode at 0 V and 40°C after 2 (□) and 31 (1) cycles (40 min chg to capacity and 20 min for 100% DOD).

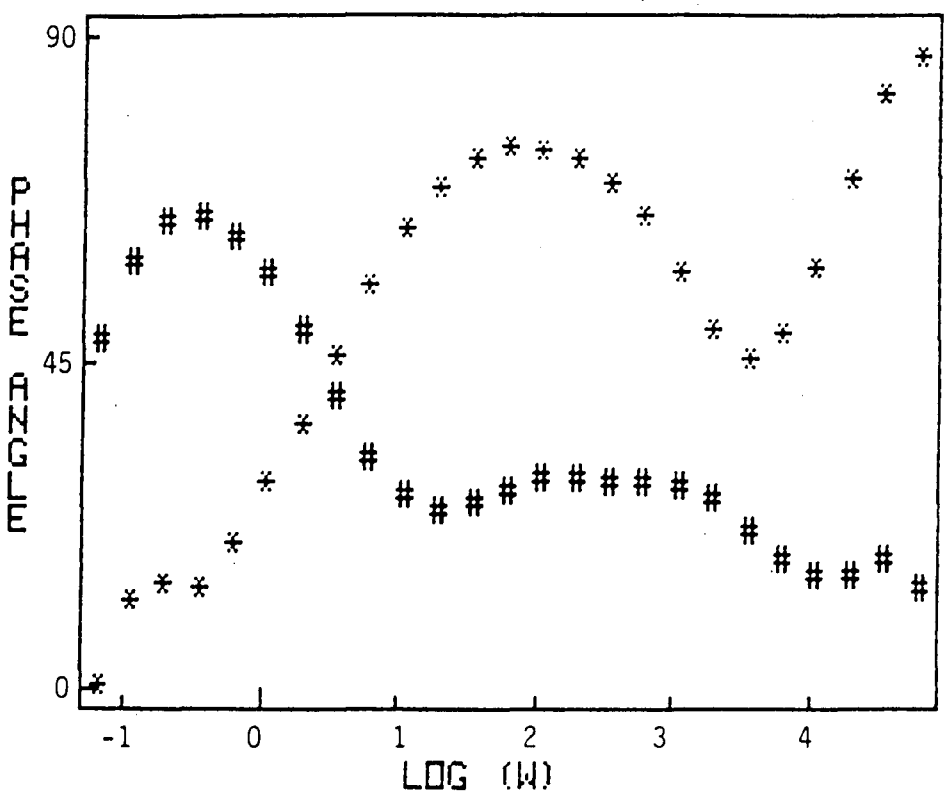

Figure 59. Bode plot of phase angle data corresponding to Figure 58 for 2 (#) and 31 (*) cycles.

The cyclic voltammetry results presented in Section III show that oxygen evolution occurs rapidly during the oxidation of nickel hydroxide at 60°C and higher temperatures. The stresses associated with the evolution of oxygen within the pores are presumeably the major cause of the rapid electrode degradation at high temperatures. The slow swelling and sloughing at lower temperatures may be related to the relatively slow rate of oxygen evolution.

5.3 Porous Sintered Electrode Impedance Data

Sintered electrodes behaved quite differently from rolled and bonded electrodes. At temperatures from 0 to 60°C, the impedance spectra were independent of cycle number (Figure 60 to 62), and were also shown to be independent of galvanostatic cycling current.

Sintered electrode failures occurred abruptly. The only indication of an impending failure was a slight wavering of the electrode potential versus time curve recorded during the galvanostatic cycles just preceding failure. Even after failure, no sloughing or swelling was ever observed. Generally, the performance of the sintered electrodes rated in terms of cycle life were far superior to rolled and bonded electrodes.

The impedance data for sintered electrodes were temperature dependent as shown in Figures 60 to 62. At 100°C, failures occurred in the first few cycles under the charge/discharge conditions used (80 minutes charging to rated capacity, and 40 minutes to 100% DOD). Impedance spectra were noisy at 100°C and second harmonic impedance spectra indicated that the electrode response to a 10 mV rms ac perturbation was not linear. The ac signal was reduced to 3 mV using a voltage divider, but the second harmonic was still large.

The impedance data for sintered electrodes were not fitted to the transmission line model because the lack of dependence of the impedance spectra on cycle number precluded any findings on degradation mechanisms. Also, examination of new and cycled sintered electrodes with the scanning electron microscope revealed that the sintered electrodes did not contain pores. Instead, the surface contained grooves (Figure 63), which are not readily represented by the TLM.

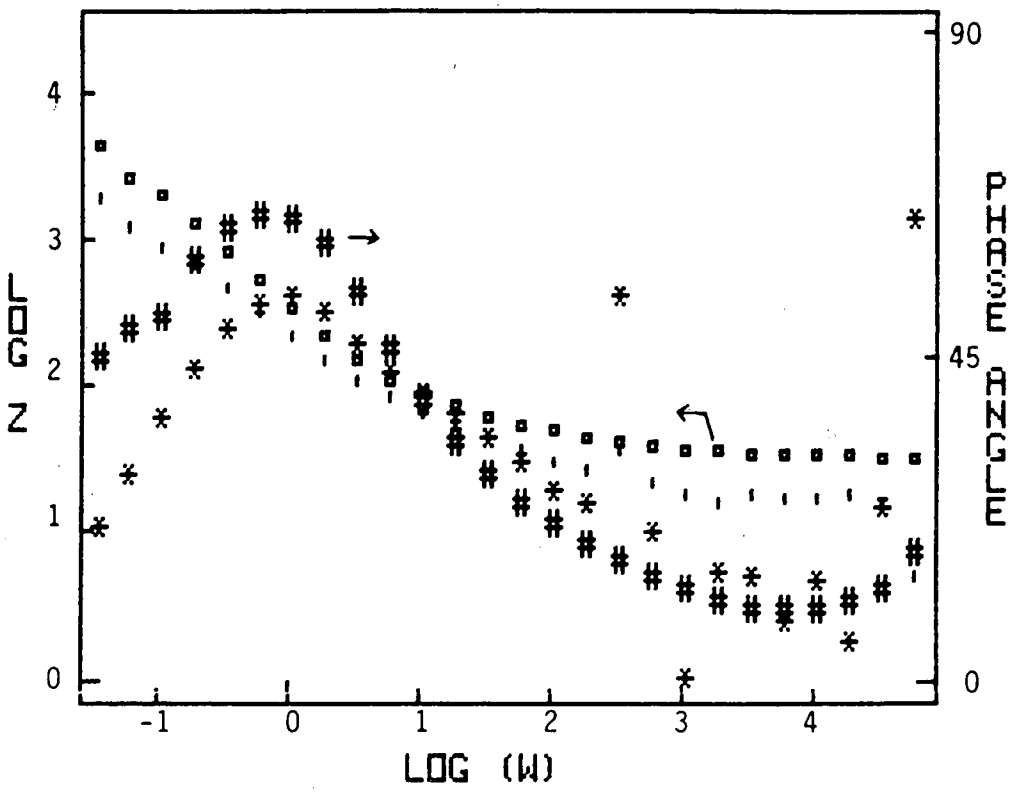

Figure 60. Bode plot of impedance data for a sintered electrode at 0°C and 0 V after 5 (□, #) and 186 (1, *) galvanostatic cycles (26 min chg to capacity with 14 min for 100% DOD). Impedance magnitude shift is most likely caused by loss of argon purge and oxygen contamination late in electrode cycle life.

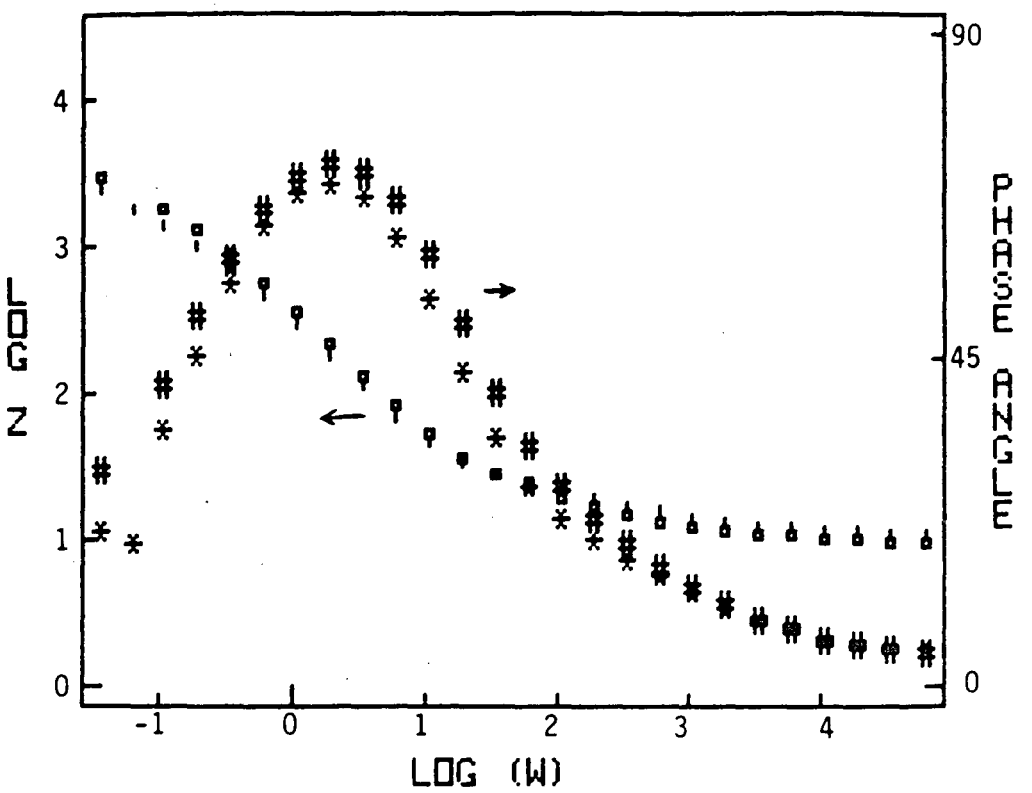

Figure 61. Bode plot of impedance data for a sintered electrode at 23°C and 0 V after 5 (□, #) and 275 (1, *) cycles (26 min chg to capacity with 14 min for 100% DOD).

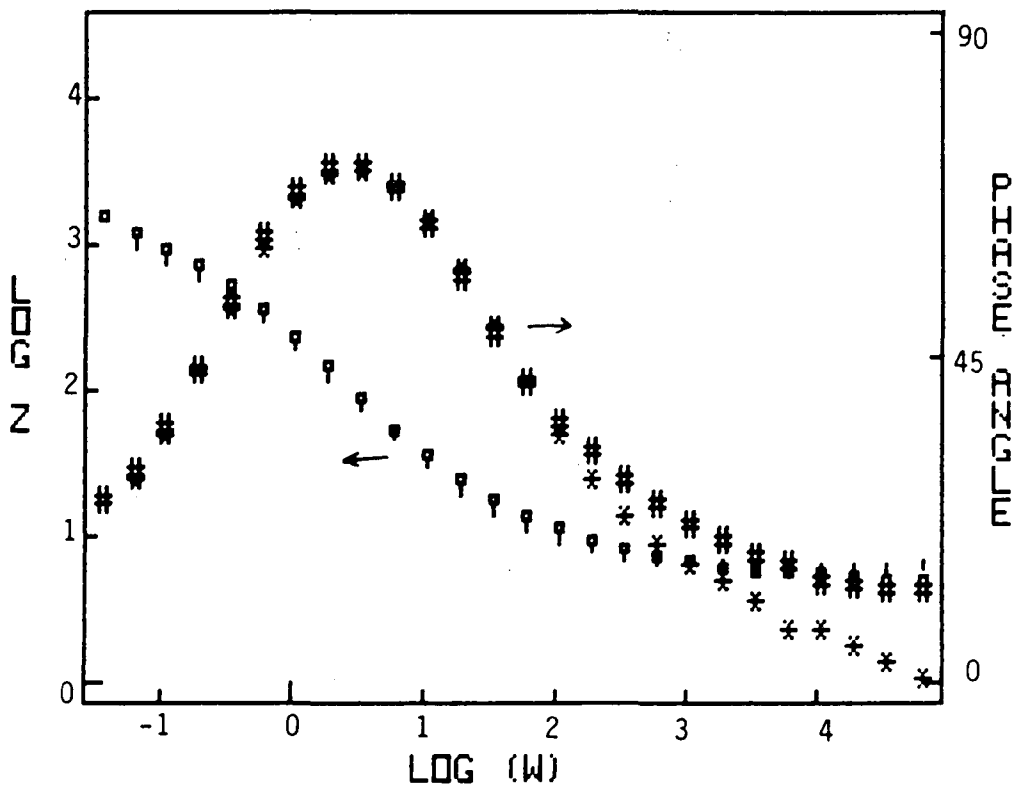

Figure 62. Bode plot of impedance data for a sintered electrode at 60°C and 0 V after 6 (□, #) and 172 (1, *) cycles (26 min chg to capacity with 14 min for 100% DOD).

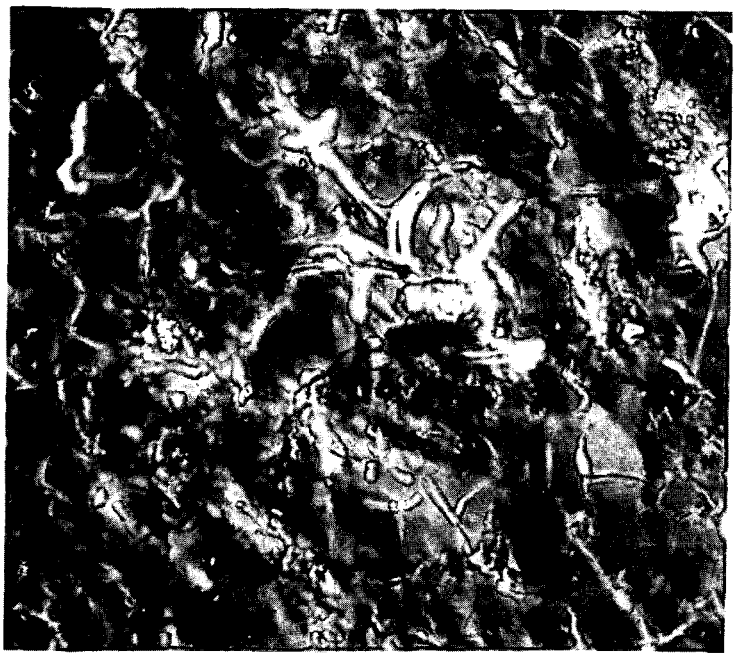

Plate 1. Uncycled

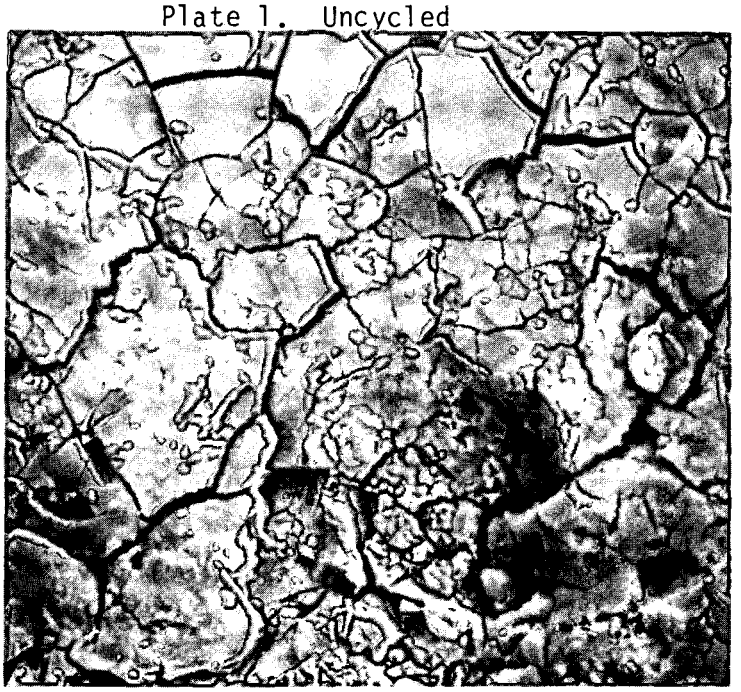

Plate 2. Cycled 5 times with 20 minutes charging time to rated capacity and 10 minutes discharging time to 100% DOD).

Figure 63. Scanning electron micrographs (240X) of a sintered electrode.

6.0 SUMMARY

The representation of ac impedance data in terms of a transmission line model provides a set of realistic parameters that in general change with cycle number in a manner consistent with experimental observation. Initial values either estimated or measured for individual parameters compare favorably with those eventually determined by curve fitting to the impedance data for rolled and bonded electrodes at 0 V and 23°C. Rolled and bonded electrode impedance data measured at 0° and 40°C behave similarly to ambient temperature data and the changes in the parameters with cycle number also appear to be similar.

The specific changes with cycle number at 23°C are as follows:

1. The average pore length decreases with cycle number, but always remains larger than the thickness of the electrode.

2. The average resistivity of the solid phase increases with cycle number.

3. The solution resistivity within the pores remains virtually unchanged during the cycle life of the electrodes.

4. The number of active pores decreases after the first few cycles.

5. The average resistance per pore of both the solution and solid phases decreases during cycling.

6. The total impedance of a porous electrode is relatively insensitive to the solution/backing plate interfacial impedance. This indicates that little current flows along the entire pore length of the solution.

These changes are generally consistent with a degradation mechanism which involves the simultaneous restructuring of the active material and rupture of particle-particle ohmic contacts. The first phenomenon accounts for the decreases in average pore length, in the number of active pores, and in the average solution resistance per pore on cycling, whereas the rupture of particle-particle contacts explains the concomitant increase in the resistance

of the active material. The restructuring process probably results from dissolution/precipitation processes which occur within the pores on cyclic charging and discharging since it presumeably requires the spatial redistribution of material within the active solid phase. On the other hand, rupture of particle-particle contacts may result from the stresses generated due to volume changes upon the cyclic interconversion of $Ni(OH)_2$ and NiOOH.

Rolled and bonded electrodes break down rapidly when cycled at 60°C and 100°C. The results from cyclic voltammetry at elevated temperatures show that, after the first few potential sweep cycles, the oxygen evolution reaction proceeds at a significant rate in the potential region for the electrode charging reaction. The rapid breakdown of porous electrodes during galvanostatic cycling at elevated temperatures can be associated with the parasitic oxygen evolution process.

The sum of squares error between experimental impedance spectra and optimized theoretical spectra from the TLM is greatest at low frequencies. Curve fitting of planar electrode impedance data to an equivalent circuit also shows discrepancies at low frequencies. Since the equivalent circuit for the planar electrode is used to represent the pore wall and backing plate interfacial impedances in the TLM, at least a part of the sum of squares error in the case of porous electrodes at low frequencies will be transferred from the corresponding error for the planar electrode. The sum of squares error for porous electrodes is less at high frequencies largely because the planar electrode impedance data could be modelled satisfactorily.

The impedance data for sintered electrodes do not change during galvanostatic cycling, and failures occur abruptly after a relatively large number of cycles. Consequently, the TLM provides little insight into degradation phenomena on sintered electrodes. However, sintered electrodes, like rolled and bonded electrodes, break down rapidly at 100°C, indicating that the oxygen evolution process may likewise affect the cycle life of sintered electrodes.

The electrochemical charge/discharge reactions on thin film nickel electrodes in 8 molal KOH appear to involve primarily the β-$Ni(OH)_2$/β-NiOOH couple. The shift of the anodic peak to higher potentials during potential

sweep cycling can be accounted for by a change in predominance from the α/γ couple to the $\beta(II)/\beta(III)$ couple after the first few cycles. However, film thickening also occurs during cycling, and the observed shift may result from this effect alone. Since thick film electrodes generally appear to behave differently from thin film electrodes, the predominance of the $\beta(II)/\beta(III)$ couple may not apply to porous battery electrodes.

REFERENCES

1. M. Pourbaix, Atlas of Electrochemical Equilibria in Aqueous Solutions, 2nd Ed., Pergamon Press, London (1974).

2. D.C. Silverman, Corrosion, 37, 546 (1981).

3. M.C.H. McKubre and D.D. Macdonald, J. Energy, 5, 368 (1981).

4. Handbook of Chemistry and Physics, p. F159, Ed. R.C. Weast, CRC Press, (1974).

5. P.C. Milner and U.B. Thomas, in Advances in Electrochemistry and Electrochemical Engineering, 5, 25, Ed. C.W. Tobias, Interscience Publishers, New York (1967).

6. H. Bode, K. Dehmelt and J. Witte, Electrochim. Acta, 11, 1079 (1966).

7. R.S. McEwen, J. Phys. Chem., 75, 1782 (1971).

8. P.C. Milner and U.B. Thomas, in Advances in Electrochemistry and Electrochemical Engineering, 5, 17, Ed. C.W. Tobias, Interscience Publishers, New York (1967).

9. C.Y. Chao, unpublished data, The Ohio State University (1980).

10. Z. Takehara, M. Kato and S. Yoshizawa, Electrochim. Acta, 16, 833 (1971).

11. E.J. Casey, A.R. Dubois, P.E. Lake and W.J. Moroz, J. Electrochem. Soc., 112, 371 (1965).

12. D. Tuomi, J. Electrochem. Soc., 112, 1 (1965).

13. R. Barnard, C.F. Randell and F.L. Tye, in Proceedings of the Symposium on the Nickel Electrode, Electrochem. Soc., 82-4 (1982).

14. G.W.D. Briggs and W.F.K. Wynne-Jones, Electrochim. Acta, 7, 241 (1962).

15. J.L. Weininger, in Proceedings of the Symposium on the Nickel Electrode, Electrochem. Soc., 82-4 (1982).

16. J.F. Jackovitz, in Proceedings of the Symposium on the Nickel Electrode, Electrochem. Soc., 82-4 (1982).

17. D.M. MacArthur, J. Electroem. Soc., 117, 422 (1970).

18. L.D. Burke and T.A.M. Twomey, in Proceedings of the Symposium on the Nickel Electrode, Electrochem. Soc., 82-4 (1982).

19. J.R. Vilche and A.J. Arvia, in Proceedings of the Symposium on the Nickel Electrode, Electrochem. Soc., 82-4 (1982).

20. A.J. Arvia and D. Posdas, Encyclopedia of Electrochemistry of the Elements, Vol.III Ed. A.J. Bard, Marcel Dekker, New York (1973).

21. S.H. Glarum and J.H. Marshall, J. Electrochem. Soc., 129, 535 (1982).

22. V.A. Macagno, J.R. Vilche and A.J. Arvia, J. Electrochem. Soc., 129, 301 (1982).

23. M.A. Hopper and J.L. Ord, J. Electrochem. Soc., 120, 183 (1973).

24. G.W.O. Briggs and M. Fleischmann, Trans. Faraday Soc., 67, 2397 (1971).

25. G. Fueillade and R. Jacoud, Electrochim. Acta, 14, 1297 (1969).

26. J.G. Wolf, L.S.R. Yeh and A. Damjanovic, Electrochim. Acta, 26, 409 (1981).

27. J.F. Wolf, L.S.R. Yeh and A. Damjanovic, Electrochim. Acta, 26, 811 (1981).

28. A. Damjanovic, L.S.R. Yeh and J.F. Wolf, Electrochim. Acta, 26, 825 (1981).

29. K.N. Goswami and R.W. Staehle, Electrochim. Acta, 16, 1895(1971).

30. F.P. Fehlner and N.F. Mott, Oxidation of Metals, 2, 59 (1970).

31. C.Y. Chao, L.F. Lin and D.D. Macdonald, J. Electrochem. Soc., 128, 1187 (1981).

32. W. Visscher and E. Barendrecht, Electrochim. Acta, 25, 651 (1980).

33. G.W.D. Briggs, G.W. Stott and W.F.K. Wynne-Jones, Electrochim. Acta, 7, 249 (1962).

34. G.W.D. Briggs and W.F.K. Wynne-Jones, Trans. Faraday Soc., 52, 1272 (1956).

35. G.W.D. Briggs, E. Jones and W.F.K. Wynne-Jones, Trans. Faraday Soc., 51, 1433 (1955).

36. M.J. Madou and M.C.H. McKubre, J. Electrochem. Soc., 130, 1056 (1983).

37. G.W.D. Briggs and P.R. Snodin, Electrochim. Acta, 27, 565 (1982).

38. O.R. Rademacher and K.W.Z. Wiesener, Z. Phys. Chem., 258, 967 (1977).

39. H.G. Meier, J.R. Vilche and A.J. Arvia, J. Appl. Electrochem., 10, 611 (1980).

40. R. Barnard, C.F. Randell and F.L. Tye, J. Appl. Electrochem., 10, 127 (1980).

41. R. Barnard, C.F. Randell and F.L. Tye, J. Appl. Electrochem., 10, 109 (1980).

42. R.S.S. Guzman, J.R. Vilche and A.J. Arvia, J. Electrochem. Soc., 125, 1578 (1978).

43. T.O. Rouse and J.L. Weininger, J. Electrochem. Soc., 113, 184 (1966).

44. W. Van Gool, Principles of Defect Chemistry of Crystalline Solids, p. 15, Academic Press, New York (1966).

45. D.M. Tench and E. Yeager, J. Electrochem. Soc., 120, 164 (1973).

46. D. Alder, Solid State Phys., 21, 1 (1968).

47. S.M. Wilhelm and N. Hackerman, J. Electrochem. Soc., 128, 1668 (1981).

48. S.R. Morrison, Electrochemistry at Semiconductor and Oxidized Metal Electrodes, Plenum Press, New York (1980).

49. A.T. Frombold, J. Electrochem. Soc., 124, 538 (1977).

50. A.T. Frombold, in Oxides and Oxide Films, 3, Eds. J.W. Diggle and A.K. Vijh, Marcel Dekker, New York.

51. M.S. Whittingham, Electrochim. Acta, 20, 575 (1975).

52. R. Barnard and C.F. Randell, J. Appl. Electrochem., 13, 27 (1983).

53. R. Barnard and C.F. Randell, J. Power Sources, 9, 185 (1983).

54. D.D. Macdonald, Transient techniques in Electrochemistry, p. 185, Plenum Press, New York and London (1977).

55. A.J. Bard and L.R. Faulkner, Electrochemical Methods, p. 213, John Wiley and Sons, (1980).

56. L.N. Sagoyan, Y.M. Gulamov, P.Z. Barsukov and V.E. Dmitrenko, 28th ISE Meeting, Ext. Abstract No. 82, Bulgaria (1977).

57. A.A. Yakovleva and Y. N. Chernykh, Electrokhim., 6, 167 (1970).

58. P.D. Lukovstev, Soviet Electrochem., 3, 156 (1961).

59. W. Wisscher and E. Barendrecht, J. Appl. Electrochem., 10, 269 (1980).

60. J.L. Weininger and M.W. Breiter, J. Electrochem. Soc., 111, 707 (1964).

61. S. Sathyanarayana, S. Venugopalan and M.L. Gopikanth, J. Appl. Electrochem., 9, 125 (1979).

62. A.H. Zimmerman and M.G. Janecki, in Proceedings of the Symposium on the Nickel Electrode, Electrochem. Soc., 82-4 (1982).

63. A.H. Zimmerman, M.R. Martinelli, M.C. Janecki and C.C. Badcock, J. Electrochem. Soc., 129, 289 (1982).

64. D.S. Humphereys, in The Analysis, Design, and Synthesis of Electrical Filters, p. 207, Prentice-Hall, (1970).

65. R.D. Armstrong and K. Edmonson, Electrochim. Acta, 18, 937 (1973).

66. J.L. Dawson and D.G. John, J. Electroanal. Chem., 110, 37 (1980).

67. M. Sluyters-Rehback and J.H. Sluyters, Electroanalytical Chemistry, 4, 1, Ed. A.J. Bard, Marcel Dekker, New York (1970).

68. J. O'M. Bockris and A.K.N. Ready, Modern Electrochemistry 1, 155, Plenum Press, New York (1970).

69. B.D. Cahan, C.T. Chen, D. Radman, D.A. Scherson, unpublished data, Case Western Reserve University, Cleveland.

70. I. Epelboin, C. Gabrielli, M. Keddam and H. Takenouti, in Comprehensive Treatise of Electrochemistry, p. 151, Ed. J. O'M. Bockris, Plenum Press (1981).

71. J.F. McCann and S.P.S. Badwal, J. Electrochem. Soc., 129, 551 (1982).

72. R. DeGryse, W.D. Goves, F. Cardon and J. Vennik, J. Electrochem. Soc., 122, 711, (1975).

73. B.D. Cahan and C.T. Chen, J. Electrochem. Soc., 129, 474 (1982).

74. E. Gileadi, Interfacial Electrochemistry.

75. M.A. Sattar and B.E. Conway, Electrochim. Acta, 14, 695 (1969).

76. Z. Takehara, J. Kato and S. Yoshizawa, Electrochim. Acta, 16, 833 (1971).

77. M.H. Katz, F.R. McLarnon and E.J. Cairns, in Battery Division Ext. Abstracts of Fall Meeting, The Electrochem. Soc., p. 24, (1982).

78. R. De Levie, Electrochim. Acta, 8, 751 (1963).

79. R. De Levie, in Advances in Electrochemistry and Electrochemical Engineering, 6, 329, Ed. P. Delahay, Interscience, New York (1969).

80. S.J. Lenhart, C.Y. Chao and D.D. Macdonald, in Proc. 16th Intersoc. Energy Conversion Eng. Conf. 11P-663, ASME, New York (1981).

81. J.R. Park and D.D. Macdonald, Corrosion Sci., 23, 295 (1983).

82. G. Nagasubramanian, B.L. Wheeler and A.J. Bard, J. Electrochem. Soc., 130, 1680 (1983).

83. C.T. Morse, in Frequency Response Analysis Techniques For Materials Testing, p.13.1, Solartron Electronic Group, Farnborough, England (1975).

84. B.D. Cahan and C.T. Chen, J. Electrochem. Soc., 129, 700 (1982).

85. L. Meites and T. Meites, J. Appl. Chem., 20, 948 (1948).

86. O.A. Lown and H.R. Thirsk, Trans. Faraday Soc., 67, 132 (1971).

87. N.J. Maskalick and E.S. Buzzelli, in Battery Division Ext. Abstracts of Fall Meeting, The Electrochem. Soc., p.24, (1982).

88. B.G. Pound, B. Sundararaj, R.P. Singh and D.D. Macdonald, "Thermodynamic Framework for Estimating the Efficiencies of Alkaline Batteries", Final Report to Lawrence Berkeley Laboratory, University of California (1983).

89. D.F. Pickett, U.S. Air Force Technical Report AFAPL-TR-75-34, Part I, (1975).

90. C.J. Wen, C. Ho, B.A. Boukame, I.D. Raistrick, W. Weppner and R.A. Huggins, International Reviews, No. 5, 253 (1981).

TECHNICAL INFORMATION DEPARTMENT
LAWRENCE BERKELEY LABORATORY
UNIVERSITY OF CALIFORNIA
BERKELEY, CALIFORNIA 94720